Phase Behaviour of Proteins and Colloid-Polymer Mixtures

Inaugural-Dissertation
zur
Erlangung des Doktorgrades der
Mathematisch-Naturwissenschaftlichen Fakultät
der Heinrich-Heine-Universität Düsseldorf

vorgelegt von

Christoph Gögelein

aus Mainz

September 2008

Gedruckt mit der Genehmigung der
Mathematisch-Naturwissenschaftlichen Fakultät der
Heinrich-Heine-Universität Düsseldorf

Referent: Prof. Dr. G. Nägele

Koreferent: Prof. Dr. S. U. Egelhaaf

Tag der mündlichen Prüfung: 24. November 2008

This thesis is partially based on the following original publications:

Chapter 2:

C. Gögelein, G. Nägele, R. Tuinier, T. Gibaud, A. Stradner, and P. Schurtenberger,
A simple patchy colloidal model for the phase behaviour of lysozyme dispersions,
Journal of Chemical Physics **129**, 085102 (2008).

Chapter 3:

C. Gögelein and R. Tuinier,
Phase behaviour of a dispersion of charge-stabilised colloidal spheres with added non-adsorbing interacting polymer chains,
European Physical Journal E **27**, 171 (2008).

Chapter 4:

C. Gögelein, G. Nägele, J. Buitenhuis, R. Tuinier and J. K. G. Dhont,
Polymer depletion-driven cluster aggregation and demixing in charge-stabilised colloidal dispersions,
(in preparation).

Other publications by the author of this thesis:

T. Blochowicz, C. Gögelein, T. Spehr, M. Müller, and B. Stühn,
Polymer-induced transient networks in water-in-oil microemulsions studied by small-angle x-ray and dynamic light scattering,
Physical Review E **76**, 041505 (2007).

Summary

In this thesis, we present a theoretical and experimental study of the equilibrium phase behaviour of colloidal dispersions and protein solutions. The thesis consists of two theoretical parts on the phase diagram of lysozyme solutions, and mixtures of charge-stabilised colloids and neutral polymers, respectively, and an experimental part on the stability of mixtures of charged colloids and non-adsorbing polymers, including a theoretical model of the aggregation kinetics.

In the first part, the phase behaviour of lysozyme solutions is calculated using thermodynamic perturbation theory applied to a patchy colloidal model with an anisotropic interaction part that incorporates screened Coulomb repulsions. The interaction parameters in this model are obtained from experimental data sets. The experimental phases are consistently described by our model of protein interactions, and nearly quantitative agreement is found for the metastable gas-liquid and the fluid-solid coexistence lines. We show that the phase behaviour of lysozyme strongly depends on the anisotropic hydrophobic interactions. The range of attraction obtained with our model is in excellent agreement with previous surface force measurements. In addition, a consistent description is obtained for the structure factor at small wave numbers.

The second part addresses the depletion interaction and the phase behaviour of mixtures of charged spherical colloids and neutral polymer chains under good and θ-solvent conditions. To predict the phase behaviour, we have derived a generalised free-volume theory, which is in good agreement with computer simulation data of the binodal for polymer-to-colloid size ratios $q \leq 1$. For $q > 1$, our theory captures the qualitative trends. We study the effect of weak electrostatic repulsions and the influence of the solvent quality, and show that the colloid charge stabilises the homogeneous phase against demixing. The phase stability is enhanced with increasing q and solvent quality. Our theory predicts that the solvent quality strongly affects the location of the gas-liquid coexistence curve in case of weakly charged colloids. For a θ-solvent and $q > 1$, the gas-liquid coexistence curve is almost unaffected by electrostatic repulsions.

In the third part, the stability and phase behaviour of an aqueous mixture of charged, nanosized spheres and polysaccharide chains of roughly equal sizes is investigated by visual inspection and photon correlation spectroscopy. We explore the interplay between charge-induced repulsion and polymer-induced colloid attraction. We find that even weak electrostatic screening, or small amounts of polymers enhance colloid aggregation. Good agreement is observed between the experimental cluster growth rates and the predictions of doublet formation theory with hydrodynamic interactions, where the polymer-induced attractions are well described by the Asakura-Oosawa-Vrij potential. We compare the non-equilibrium phases caused by macroscopic phase separation, with predictions from a generalised free-volume theory on equilibrium phases, and observe similar trends regarding the salt influence.

Zusammenfassung

In dieser Arbeit werden Gleichgewichtsphasenübergänge in kolloidalen Dispersionen und Proteinlösungen theoretisch und experimentell untersucht. Die Dissertation setzt sich zusammen aus zwei theoretischen Teilen über das Phasenverhalten von Lysozymlösungen und Mischungen von ladungsstabilisierten Kolloiden und neutralen Polymeren. In einem vorwiegend experimentellen Teil untersuchen wir das Nichtgleichgewichts-Phasenverhalten und die Aggregationskinetik von wässrigen Mischungen geladener Kolloidkügelchen, einschließlich eines theoretischen Modells zur Beschreibung der initialen Aggregationskinetik.

Im ersten Teil wird das Phasenverhalten von Lysozym im Rahmen eines kolloidalen Modells mit anisotrop anziehenden sowie abgeschirmten Coulomb-Wechselwirkungen unter Verwendung einer thermodynamischen Störungstheorie berechnet. Die in diesem Modell auftretenden Wechselwirkungsparameter werden anhand von experimentellen Daten bestimmt. Die experimentell auftretenden Phasen werden konsistent in unserem Modell beschrieben. Die berechneten gas-flüssig und flüssig-fest Koexistenzkurven stimmen nahezu quantitativ mit den experimentellen Daten überein. Dies zeigt, dass das Phasenverhalten von Lysozym wesentlich durch die anisotropen Wechselwirkungen beeinflußt wird. Die aus unseren Rechnungen gefundene Reichweite der anziehenden Wechselwirkung stimmt sehr gut mit zuvorigen Messungen überein. Weiterhin liefert unser Modell eine konsistente Beschreibung des Kolloidstrukturfaktors bei kleinen Wellenzahlen.

Der zweite Teil befaßt sich mit Depletionswechselwirkungen und dem Gleichgewichts-Phasenverhalten von Mischungen aus geladenen Kolloiden und Polymeren in guten und θ-Lösungsmitteln. Das Phasenverhalten wird bestimmt mittels einer generalisierten freien Volumentheorie, die für kleine Polymer-Kolloid Größenverhältnisse $q < 1$ Ergebnisse liefert in guter Übereinstimmung mit früheren Computersimulationen. Für $q > 1$ beschreibt die Theorie das Phasenverhalten nur qualitativ richtig. Wir untersuchen insbesondere den Einfluß schwacher elektrostatischer Abstoßungen und den Einfluß der Lösungsmittelqualität und zeigen, daß die Kolloidladungen die homogene Phase gegen Entmischung stabiliseren. Die Phasenstabilität nimmt mit anwachsendem q und anwachsender Lösungsmittelqualität zu. Die Lösungsmittelqualität beeinflußt auch stark die Lage der gas-flüssig Koexistenzkurve für schwach geladene Kolloide. Für ein θ-Lösungsmittel und für $q > 1$ bleibt die Binodale nahezu unbeeinflußt von der Coulombabstoßung.

Im dritten Teil wird die Stabilität und das Phasenverhalten einer Mischung von geladenen, nanometrischen Kolloiden und Polymeren von etwa gleicher Größe mittels Photonenkorrelationsspektroskopie untersucht, um das Wechselspiel zwischen ladungsinduzierter Abstoßung und polymerinduzierter Anziehung der Kolloide zu studieren. Wir finden, daß bereits eine geringe elektrostatische Abschirmung bzw. eine geringe Polymerkonzentration die Aggregation der Kolloide beschleunigt. Die experimentellen Aggregationszeiten stimmen gut mit der Ag-

gregationstheorie von kolloidalen Dimeren überein, wobei darin hydrodynamische Wechselwirkungen berücksichtigt sind und die polymerinduzierte Anziehung mit dem Asakura-Oosawa-Vrij Potential beschrieben wird. Wir vergleichen die experimentellen Nichtgleichgewichts-Phasen mit den Vorhersagen der generalisierten freien Volumentheorie für die Spinodale und Binodale, und finden analoge Trends für den Einfluß der Salzkonzentration.

Contents

1 Introduction

We come across phase transitions in everyday life whenever we boil or freeze water, while we are ice-skating or, for another example, when we dissolve table salt. Common to all these phenomena is that we recognise an abrupt change in the materials constitution, which enables us to distinguish unequivocally the states of matter, i.e., the thermodynamic phases. For atomistic systems, it is usually not possible to tune the location of a coexistence curves in a first-order phase transition by changing the interaction strength on atomistic or molecular length scales, since these are ruled by quantum mechanics. Each molecular system exhibits a specific phase behaviour and no systematic, gradual variations of the molecular interactions can be made to study the accompanied changes of the phase diagram [1]. This is quite different in colloidal systems. Colloidal dispersions consist of particles of nanometre-to-micrometre-size, dispersed in a low-molecular weight solvent [2]. The particles can be solid, e.g., made of glass or plastic, or soft objects like vesicles or liquid droplets stabilised by surfactants (micelles). Such systems of colloidal particles of varying length scales are prime examples of soft matter. For example, paints, ink, glue, milk, or in a wider sense blood and the cytoplasm within cells belong to this class of condensed matter. As these examples illustrate, colloids are part of our everyday experience. They are thus of industrial, medical and biological interest.

The large separation of time and length scales between the large colloidal particles and the smaller solvent molecules allows in many cases to disregard the molecular nature of the solvent [3]. Therefor, colloidal suspensions are commonly described as systems that interact via an effective potential, which accounts in a coarse-grained way for the effect of the embedding solvent and additional constituents (such as, e.g., ions and polymers) on the colloid interactions. This simplifying description is formally obtained by integrating out the degrees of freedom of the surrounding small solvent molecules and additives. Usually, there is a price to pay for this coarse-graining in that the effective interactions include many-body contributions [4]. The colloid-colloid interactions, and thereby the phase behaviour, can be tuned by variation of the salt concentration in case of charged colloids, by adding polymers, mixing solvents, and so forth.

Due to the many possibilities of modifying the solvent and colloid properties, the interactions between mesoscopic particles can be tuned in many different ways giving rise to an unprecedented richness in the phase behaviour [5]. Repulsive particle interactions are, for example, caused by surface charges, whereas attractive interactions can be imposed by adding non-adsorbing polymer chains [6]. In

addition, globular particles with hard-sphere-like interactions can be produced by covering the colloid surface with short polymer brushes [7], and by dispersing the particles in a non-polar solvent with similar dielectric properties to avoid significant dispersion attractions. It is even possible to reverse the effective interactions from purely repulsive to attractive by modifying the solvent properties. Due to their large size and their slow dynamics, one can relatively easily observe, as compared to atomic fluids, the structure and dynamics of colloidal suspensions with scattering methods (light, x-ray, neutrons) and, for larger particles, with optical imaging techniques such as light microscopy and confocal microscopy. Since, by definition, colloidal particles exhibit thermal motion, colloidal dispersions can be quantitatively described using classical statistical mechanics [8, 9]. This link has led to a mutual inspiration between theory and experiments in the past. To this day, colloid science is a very active field of research. In particular, the study of colloid model systems has led to an increased knowledge on the influence of the strength and range of interactions on the stability of equilibrium phases. If the range of the attractive interaction part is sufficiently short, the gas-liquid coexistence region becomes metastable with respect to a fluid-crystal phase separation. Such a situation is often observed in protein solutions, which can be considered as a colloidal dispersion. In fact, concepts developed in colloid physics have been successfully applied more recently to biological systems.

In chapter 2, we propose and analyse a simple model to describe the phase behaviour of lysozyme protein solutions. We devise a patchy colloidal model with anisotropic attractive interactions. The phase behaviour of lysozyme solutions is calculated using second-order thermodynamic perturbation theory. As our calculations demonstrate, the gas-liquid coexistence curve of lysozyme can only be consistently described by incorporating a long-ranged patchy attractive and a charge-induced repulsive pair interaction. In particular, we use previously obtained experimental data on the phase behaviour at the critical point to quantify the range and strength of the unknown attractions. Using these critical parameters, we can predict the crystallisation curve. The overall good agreement between the experimental data and our predictions for the phase coexistence curves, and the excellent compliance of the estimated attraction range with former surface force measurements on hydrophobic plates found in the literature, allow us to conclude that the anisotropic attractive interactions are due to the hydrophobic patches on the protein surfaces.

In Chapter 3, we investigate the combined influence of polymer-depletion-induced colloid attractions and charge-induced repulsions on the phase behaviour of colloid-polymer mixtures. For this purpose, we apply the so-called free-volume approximation to study the topology of the phase diagram. That is, we explore the influence of the polymer-to-colloid size ratio, which defines the range of colloid attraction, as well as the salt concentration, which determines the electrostatic range of repulsion of two colloidal particles due to the screening of the colloid charges. By interpolating between the limit of dilute polymer concen-

trations, where the polymer solution can be described by an ideal gas law, and approximate scaling relations known for semi-dilute polymer concentrations, our calculations capture qualitatively the phase behaviour of colloid-polymer mixtures under good- and θ-solvent conditions. Interestingly, for polymer-to-colloid size ratios larger than one, our calculations predict a strong effect of the solvent quality on the phase behaviour of mixtures of polymer chains and weakly charged colloids.

Chapter 4 contains an experimental study on the properties of such a mixture of charged colloids with non-adsorbing added polymers. We explore an aqueous suspension of charge-stabilised and nanometre-sized silica spheres, and a water-soluble and non-adsorbing polysaccharide (dextran) used as depletion agent. A feature that was not considered in the thermodynamics treatment of the previous chapter is colloid aggregation. As we will discuss in Chapter 4, for unstable colloid-polymer mixtures demixing and aggregation can occur simultaneously. In regions of the phase space where no aggregation occurs, or where aggregation is slow as compared to phase separation, a comparison of the experimental phase diagram with the free-volume theory of Chapter 3 is made. The existence of non-equilibrium clusters is an example of a state which is usually not found in molecular systems, giving rise to specific and new phenomena in colloidal suspensions. If the colloidal particles have steep and short-ranged attractive interactions at near-contact inter-particle distances, they can stick together after a collision and form open-structured clusters which grow in time. In the first part of this chapter, we investigate the influence of the salt concentration on the cluster-aggregation process in dispersions of silica spheres in water without added polymers. To gain quantitative insight, the cluster growth rate is monitored using photon correlation spectroscopy. In a next step, polymers of varying molecular weight and concentration are added to the dispersion. Due to the polymer-induced, long-ranged attractive depletion forces, cluster aggregation is accelerated with increasing polymer concentration. Furthermore, we find from our experiments that the cluster growth rate decreases with increasing polymer-to-colloid size ratio. Following previous work on cluster-aggregation processes, the experimental observations are explained by the doublet formation theory [6] with an account of hydrodynamic interactions. In addition to the electrostatic repulsion and the short-range van der Waals attraction, we account for the effect of the polymer chains, which cause an additional attraction due to the depletion mechanism, described by the Asakura-Oosawa-Vrij depletion potential. The interplay between non-equilibrium cluster-aggregation and a faster progressing demixing process, are discussed on the basis of a series of experimentally observed non-equilibrium state points determined for varying colloidal volume fractions and polymer concentrations, and for different salt concentrations.

In the final chapter 5, a summary is given of all three topics included in the thesis, and an outlook of possible future research is presented.

2 A simple patchy colloid model for the phase behaviour of lysozyme dispersions

In this chapter, we propose a minimal model for spherical proteins with aeolotopic pair interactions to describe the equilibrium phase behaviour of lysozyme. Within our model, the repulsive screened Coulomb interactions between the particles are taken into account on assuming that the net charges are smeared out homogeneously over the spherical protein surfaces. We incorporate attractive surface patches, with the interactions between patches on different spheres modelled by an attractive Yukawa potential. The parameters entering the attractive Yukawa potential part are determined using information on the experimentally accessed gas-liquid-like critical point. The Helmholtz free-energy of the fluid and solid phases are calculated using second-order thermodynamic perturbation theory. Our predictions for the solubility curve are in overall good agreement with the experimental data. By means of a set of experimental data for the gas-liquid coexistence curves measured at various salt concentrations, we demonstrate that our model is able to describe theoretically the influence of added salt on the phase behaviour of lysozyme solutions. In agreement with earlier findings, we observe that the strength and the range of the attractive potential part only weakly depends on the salt content. Our approach thus gives a consistent description of the experimental findings on the phase behaviour of lysozyme solutions.

2.1 Introduction

The exploration of crystallisation processes of proteins is a the subject of very active research, since obtaining regular crystals is indispensable for the structural analysis using, e.g., X-ray scattering tools [10]. In practice, crystallographers need to screen many batches by varying the solution properties until the proper conditions are found where regular crystals are formed [11]. Obviously, this approach is time-consuming and tedious, and one would like to have a rule of thumb to know in advance for what conditions a successful crystallisation route may be

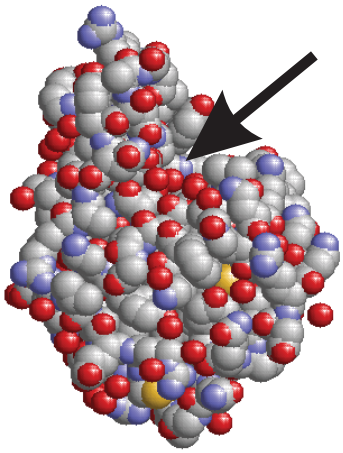

Figure 2.1: The crystal structure of lysozyme (ID 133l) taken from the Protein Data Bank [20,21]. The arrow marks the active centre where the hydrolysis of specific kinds of polysaccharides comprising the cell walls of bacteria is catalysed.

achieved. Several ways to accelerate structural analysis have been discussed, e.g., transferring the proteins to solvent conditions far away from their native environment by increasing the salt concentration (salting-out effect), adding di- and multivalent ions (Hofmeister series), and varying the *p*H-value, the temperature, or adding depletion agents [10].

The application of concepts from colloidal science to proteins has led to progress in understanding their interactions and phase behaviour. By applying the Derjaguin-Landau-Verwey-Overbeek (DLVO) theory of colloidal stability [12] to proteins, and by adjusting the van der Waals interaction to match the experimental data, it had been concluded that proteins interact essentially by long-ranged screened electrostatic repulsion due to their effective surface charges, and by short-ranged attractive forces responsible for a metastable gas-liquid coexistence curve [13–15]. In addition, the adhesive hard-sphere model, as exemplified by the sticky-sphere model, has been applied to protein solutions [16–18]. However, in the presence of such extremely deep ($\sim 8k_{\mathrm{B}}T$) and short-range attractions ($\sim 10\%$ of the protein diameter) obtained from models with isotropic interactions using the DLVO-theory, one might expect that the proteins coagulate, whereas non-coagulated stable phases are observed [19]. Experiments on the phase behaviour have been focused so far mainly on solutions of lysozyme proteins. Lysozyme is an enzyme which damages bacterias by hydrolysing cell-wall-attached polysaccharides. In Fig. 2.1, the crystal structure of lysozyme is shown, indicating also the active centre where the hydrolysis takes place. Due to its antibacterial effect, lysozyme is abundant in several of secretions, such as saliva, mucus and

tears. Large concentrations of lysozyme are found in the white component of hen-eggs. Therefore, lysozyme proteins used in experiments to investigate the phase behaviour have often been extracted from hen-eggs. For these systems, a large amount of data and insight has been accumulated during the past: Taratuta *et al.* [22] have discovered the existence of a gas-liquid coexistence curve, which was subsequently shown to be metastable with respect to the fluid-crystal phase separation by Broide *et al.* [19]. George and Wilson [23] have found that there is a narrow band of negative values for the second virial coefficient for which crystallisation occurs. Thereafter, ten Wolde and Frenkel [24] demonstrated that the nucleation barrier is lowered in the region close to the critical point. As a consequence, the understanding and prediction of the fluid phase behaviour has turned out to be a prerequisite to describe nucleation kinetics. For a more detailed general discussion of protein crystallisation, we refer to the two reviews by Piazza in [17] and [25].

Further progress in explaining the experimental gas-liquid phase separation was made by considering anisotropic protein interactions. To investigate the influence of attractive patches on the protein surfaces, Benedek and co-workers [26, 27] have used an orientation-dependent square-well potential, which allows for a remarkably good description of the gas-liquid phase coexistence as well as for the solubility curve. Moreover, they demonstrated that whether one is allowed to orientationally average the angular-dependent pair potential depends strongly on the number of nearest neighbours, and on the number and size of patches. Thus, taking into account the anisotropic interactions is crucial in describing crystallisation in lysozyme solutions.

Kern and Frenkel [28] have discussed the phase behaviour by accounting for the relative orientation of two interacting molecules. Different from them, Lomakin *et al.* [26,27] disregarded in their computer simulation study the anisotropy of all surrounding particles in the total interaction pair potential. From their computer simulations, Kern and Frenkel conclude that the critical temperature decreases as the surface area of the attractive patches decreases. Moreover it follows from their simulations that the critical volume fraction depends only weakly on the patch area, and that for constant surface coverage, the critical temperature decreases with decreasing number of patches. According to Kern and Frenkel, the critical point is no longer characterised by a unique value of the second virial coefficient, but rather depends on the number and area of patches.

Recently, Liu *et al.* [29] have extended Kern and Frenkel's approach on using a sum of a patchy and an isotropic square-well attractive pair potential. They find good agreement between the experimental gas-liquid coexistence curve and their theoretical binodal. In their model calculations a heuristic set of interaction parameters determining the range and strength of the isotropic and anisotropic interaction potential part is selected by scaling the temperature and the particle density with the experimental values at the critical point. Additionally, they observe that the location of the critical point is only slightly affected by the

surface distribution of patches.

In an alternative approach Sear [30] has addressed the problem of protein crystallisation by applying Wertheim's perturbation theory [31,32] for self-associating fluids. He obtains a qualitative description of the phase behaviour. In Wertheim's theory, the interactions are assumed as point-like, so only site-site bounds can be formed. Clusters and percolated gels are described here by assuming non-vanishing probabilities for the formation of monomers, dimers, and so on, leading to a statistical description of the associating fluid. This approach has afterwards been used by Warren [33] to explore the influence of added salt on the phase behaviour of lysozyme. In addition, Sear's model has been used by Zukoski and co-workers, to address the problem of the nucleation kinetics in protein solutions (see [34] and references therein). They have also compared their results to the experimental data on crystal nucleation kinetics [34, 35].

Despite this success and the valuable insight gained by using Wertheim's perturbation theory, the Sear model lacks the incorporation of patches. Fantoni *et al.* [36] pointed to this shortcoming, and developed an analytical description for patchy hard spheres using Baxter's adhesive sphere model. They compared the results of their analytical description for the structure in the anisotropic liquid and the equilibrium phase behaviour with their computer simulations.

An anisotropic interaction-site lattice model was proposed by Talanquer [37]. In this work, the occurrence of non-spherical critical nuclei is predicted whose specific geometry depends on the strength of the anisotropic interactions.

The influence of the number of patches on the crystal lattice structure has been investigated by Chang *et al.* [38] using computer simulation methods. Interestingly, in case of a model with six patches, they observed a phase transition from a simple cubic (sc) to an orientationally disordered face-centred cubic lattice (fcc) above room temperature. In addition they observed a metastable transition between the orientationally disordered and ordered face-centred cubic lattice at lower temperature. This study demonstrates that anisotropic interactions can lead to manifold crystal structures that depend crucially on the geometry and strength of the patchy interactions.

Quite recently, theoretical work on dispersions of patchy colloid particles has caused much attraction due to the progress made by Bianchi *et al.* [39]. On varying the patchiness, they demonstrated that patchy colloids can offer the possibility to generate a beforehand inaccessible liquid state, with a possible percolation threshold at temperatures below the critical point without a preceding gas-liquid phase separation.

Common to all previous studies incorporating anisotropic interactions is that they use a square-well potential to describe the attractive interaction part between the proteins. A square-well form, however, is only realistic in case of a very short-ranged attraction and negligible non-excluded volume repulsions such as in high-salt systems. On decreasing the salinity, the range of the screened electrostatic repulsion increases. Hence, the fluid phase becomes stabilised against

gas-liquid phase separation on lowering the salt content, and one can expect that the critical point is shifted to lower temperatures. For zero added salt, one expects in lieu of a gas-liquid coexistence a microphase separation to take place [40–42], which actually has been seen experimentally [43]. Such equilibrium clusters form if, first, the range of repulsion is large enough to stabilise the conglomerates against further growth, and second, if the attractive forces are sufficiently short-ranged to hinder particles from escaping the cluster.

To investigate the influence of discrete charge patterns on the protein surfaces regarding many-body interactions, Allahyarov *et al.* [44] have performed Molecular Dynamic simulations where, in addition, the finite size of the microions has been accounted for. In lysozyme solutions they observe deviations in the angular-averaged pair potential from the monotonic decaying behaviour predicted by DLVO theory only for large ionic strengths.

The thermodynamic properties of lysozyme crystals have been investigated in detail by Chang *et al.* [45]. These authors have combined atomistic Monte Carlo simulation to account for the anisotropic shape and van der Waals attractions with a boundary element method as a solver of the Poisson-Boltzmann equation to account for the discrete charge distribution close to the lysozyme surface, and the effect of salt-induced screening. Whereas the predicted van der Waals energy and the electrostatic energy are in good agreement with experimental data for a tetragonal lattice structure, the agreement is less good found for an orthorhombic lattice structure. This discrepancy can be attributed to both a change in the solvation structure, which has been observed experimentally, and to the general difficulties in describing van der Waals interactions quantitatively.

In the present work, we include the screened electrostatic repulsion explicitly in the pair potential to separate the influence of the screened Coulomb repulsions from the attractive forces in lysozyme solutions, which are presumably induced by hydrophobic interactions and dispersion forces [46,47]. In Fig. 2.2(a) we have coloured the hydrophobic segments by red and all non-hydrophobic polypeptide segments by blue. As can be seen in this colour map, the surface of lysozyme is covered by several hydrophobic regions (or patches). In our model calculations, the patchy attractive forces are assumed to be of a Yukawa-like form. This enables us to characterise and quantify the strength and range of the radial attractive pair potential part from data on the experimental critical point and the measured binodals, as well as to investigate the competing effects of repulsive and attractive pair forces on the phase behaviour as a function of salinity.

The chapter is organised as follows: in section 2.2 we explain in detail the model describing the attractive patchy and repulsive screened electrostatic pair interactions. The Helmholtz free energy of the fluid and solid phases is calculated using second-order perturbation theory, as described in section 2.3. In section 2.4, we explain how we determine the range and strength of the attractive potential part, as well as the patchiness of the proteins, by using information on the experimentally observed critical point. For this purpose, we take advan-

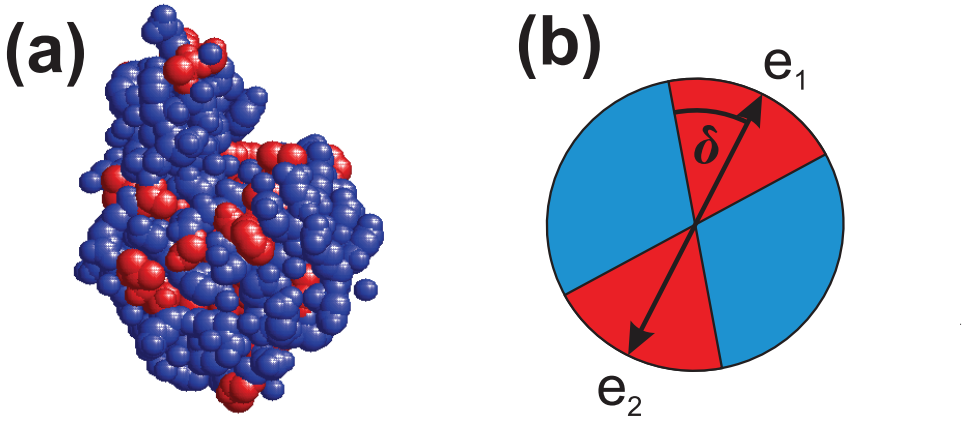

Figure 2.2: Left hand side (char (a)): Tertiary crystal structure of lysozyme. The hydrophobic segments have been coloured red and all remaining non hydrophobic segments blue. Right-hand side (char (b)): Two-dimensional sketch of the spherical patchy model of lysozyme. The hard-sphere colloidal particle carries two attractive patches (red areas) characterised by an opening angle δ and normal direction $\mathbf{e}_\alpha$ ($\alpha = 1, 2$).

tage of an earlier finding of Warren [33] on the second osmotic virial coefficient of lysozyme solutions, and an extended corresponding state argument of Noro and Frenkel [48]. This simplifying strategy enables us to quantify the range and strength of attraction, and the surface area fraction covered by attractive patches. In section 2.5 we present the calculated phase diagrams. To compare the theoretical coexistence curves with the experimental data, we include the temperature dependence of the attractions. In section 2.7 we discuss the so-obtained physical parameters in comparison to previous findings. The capability of our model to describe the influence of added salt on the gas-liquid coexistence curve is demonstrated through a comparison with existing [49] and new experimental data on lysozyme solutions at various salinities. We also predict the fluid-solid coexistence curve for the experimentally given salt concentrations. Finally, in section 2.8, we present our conclusions.

2.2 The model

We assume that the total pair potential, $u(r, \Omega_1, \Omega_2)$, between two spherical proteins at a centre-to-centre distance r, can be described by a known repulsive isotropic interaction potential part, $u_{\text{rep}}(r)$, due to the effective charges on the protein surfaces and an attractive, patchy interaction part, $u_{attr}(r, \Omega_1, \Omega_2)$, with yet unspecified interaction parameters. The finite size of the spherical protein is

accounted for using a hard-sphere potential, $u_0(r)$, by mapping the ellipsoidal-like shape [50] of a lysozyme protein onto an effective sphere as explained at the end of this section. In total,

$$u(r, \Omega_1, \Omega_2) = u_0(r) + u_{\rm rep}(r) + u_{\rm attr}(r, \Omega_1, \Omega_2)\,. \tag{2.1}$$

Here, $\Omega_{\rm i}$ is the solid angle of a sphere i, and the hard-sphere potential part is

$$u_0(r) = \begin{cases} \infty\,, & r \le \sigma \\ 0\,, & r > \sigma\,, \end{cases} \tag{2.2}$$

where σ denotes the protein diameter.

The repulsive pair interaction part is described by the electrostatic part of the one-component macroion-fluid potential [51],

$$\beta u_{\rm rep}(r) = \begin{cases} Z^2\, l_{\rm B}\, Y^2 \frac{\exp\left[-z_{\rm rep}(r/\sigma - 1)\right]}{r}\,, & r > \sigma \\ 0\,, & r \le \sigma\,, \end{cases} \tag{2.3}$$

Here, Z is the protein charge number, and $l_{\rm B} = e^2/\left(4\pi\varepsilon_0\varepsilon k_{\rm B}T\right)$ is the Bjerrum length with the dielectric constant in vacuo, ε_0, the dielectric solvent constant, ε, the elementary charge e and the temperature T.

The effects of the finite size and concentration of the colloidal macroions on the interaction strength is incorporated by the factor $Y = X\exp(-\kappa\sigma/2)$, where

$$\kappa^2 = 4\pi l_{\rm B} N_{\rm A}\left(|Z|\frac{\rho_0}{M}\eta + 2c_{\rm s} + 2c_{\rm b}\right) \tag{2.4}$$

is the square of the Debye screening parameter κ, $N_{\rm A}$ is Avogadro's constant, $\eta = \pi\rho\sigma^3/6$ is the protein volume fraction, ρ is the number density of proteins of molar mass M, and ρ_0 is the protein mass density. The molar buffer and monovalent molar salt concentrations are denoted by $c_{\rm b}$ and $c_{\rm s}$, respectively. For the systems studied in this work, κ is determined essentially by the added salt concentration. The explicit form of the geometric factor, $X(\eta, \kappa\sigma)$, as obtained in the mean-spherical approximation (MSA) for point-like microions is quoted in the appendix. The factor X accounts, within the linear MSA, for the reduced screening ability of the microions at non-zero concentration of proteins (macroions). It decreases with decreasing protein concentration and approaches the standard DLVO prefactor $X_0 = 1/(1 + \kappa\sigma/2)$ for $\rho \to 0$. Since Z is quite small, we have disregarded here the charge renormalisation effect caused by quasi-condensed counterions (see, e.g., [52]). The reduced screening parameter $z_{\rm rep} = \kappa\sigma$ quantifies the electrostatic screening length in units of σ. For later discussion, we abbreviate the non-dimensionalised contact value of $u_{\rm rep}(r)$ as $\beta\epsilon_{\rm rep} = Z^2 l_{\rm B} Y^2/\sigma$.

In using this effective electrostatic interaction part, we neglect the discrete surface charge pattern of lysozyme. Such effects have been investigated by Allahyarov *et al.* in Refs. [44, 53]. We will refer to their results in our discussion in section 2.7.

Commonly, the *p*H-value and the excess amount of salt are carefully adjusted in a protein solution under experimental conditions. Then the salt concentration c_s, the co- and counterion concentrations, and the protein net charge number Z are precisely known. Therefore, the repulsive electrostatic interaction part is completely determined by the system temperature and the protein volume fraction η.

To describe the attractive interactions between adjacent patches on two protein surfaces, we employ the patchy model description of Kern and Frenkel [28], on assuming that the radial and angular degrees of freedom can be factorised. The attractive interaction potential part, $\tilde{u}_\mathrm{attr}(r)$, hereby is angularly modulated by an angular distribution function, $d(\Omega_1, \Omega_2)$, that depends on the solid angles Ω_1 and Ω_2 of two particles 1 and 2, respectively, according to

$$u_\mathrm{attr}(r, \Omega_1, \Omega_2) = \tilde{u}_\mathrm{attr}(r) \times d(\Omega_1, \Omega_2)\,. \tag{2.5}$$

The particles are assumed to have $\alpha = 1 \ldots n$ attractive spherical caps on each surface, with an opening angle δ around the normal direction, $\mathbf{e}_\alpha$, of each cap (see Fig. 2.2(b)). According to Fig. 2.3, two particles, 1 and 2, attract each other only if the centre-to-centre vector, $\mathbf{r}$, intersects simultaneously the patchy cones of particle 1 and 2. This is equivalent to demanding that for attraction the angle $\theta_{12,\alpha}$ between the normal vector $\mathbf{e}_\alpha$ of patch α on particle 1, and the angle $\theta_{21,\beta}$ between the normal vector $\mathbf{e}_\beta$ of patch β on particle 2 are simultaneously smaller than δ. The angular distribution function, $d(\Omega_1, \Omega_2)$, is thus given by

$$d(\Omega_1, \Omega_2) = \begin{cases} 1\,, & if \begin{cases} \theta_{12,\alpha} \le \delta \text{ for a patch } \alpha \text{ on } 1 \\ \text{and} \quad \theta_{21,\beta} \le \delta \text{ for a patch } \beta \text{ on } 2 \end{cases} \\ 0\,, & \text{otherwise}\,. \end{cases} \tag{2.6}$$

Different from the work of Kern and Frenkel, where an attractive square-well potential has been used for $\tilde{u}_\mathrm{attr}(r)$, we use here an attractive Yukawa-type potential of the form

$$\tilde{u}_\mathrm{attr}(r) = \begin{cases} -\,\tilde{\epsilon}_\mathrm{attr}(T)\,\sigma\,\frac{\exp\left[-z_\mathrm{attr}(r/\sigma - 1)\right]}{r}\,, & r > \sigma \\ 0\,, & r \le \sigma\,, \end{cases} \tag{2.7}$$

where the temperature-dependent potential depth, $\tilde{\epsilon}_\mathrm{attr}(T)$, is described as [27]

$$\tilde{\epsilon}_\mathrm{attr}(T) = \epsilon_\mathrm{attr}\left(1 + \psi\,\frac{[T_\mathrm{c} - T]}{T_\mathrm{c}}\right)\,. \tag{2.8}$$

Here, T_c is the critical temperature at the liquid-gas coexistence, and ϵ_attr and ψ are two physical parameters, which will be determined from the experimental data at the critical point (see later). Since the strength of the attractive potential part increases with decreasing T, the signs of ψ and ϵ_attr have to be positive. For $\psi = 0$, the attractive potential part would be temperature-independent. The

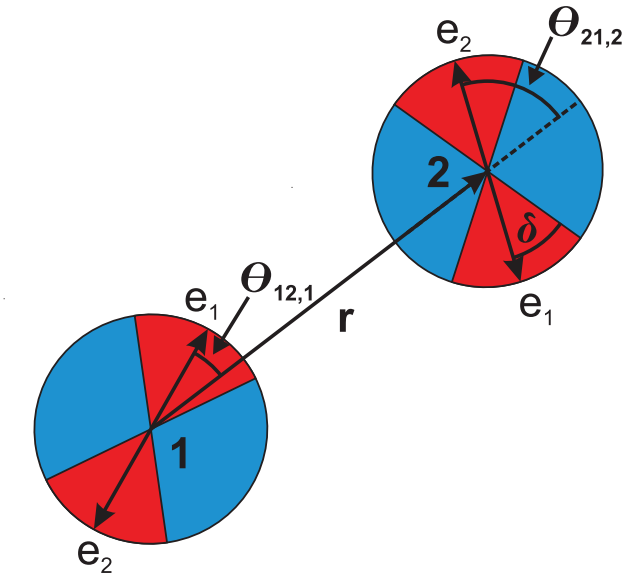

Figure 2.3: Schematic drawing of a configuration of two model proteins, each carrying two attractive patches (red cones). For the given configuration, the two particles repel each other as described by the screened electrostatic potential in Eq. (2.3), with the surface charge assumed to be smeared out homogeneously over the sphere surface as indicated by the blue colour. There is no attractive interaction part, since the centre-to-centre vector, **r**, does not intersect simultaneously the shaded attractive patches on particles 1 and 2. See the main text for the definitions of the remaining symbols.

temperature dependence in Eq. (2.8) constitutes a first-order Taylor-expansion around T_c. It can be considered as a simple approximation to the so far not well understood temperature dependence of the attractive hydrophobic interactions. The expansion around $T = T_c$ has been selected since the critical temperature is an experimentally well-assessed quantity.

The fraction, χ, of the sphere surface covered by the n attractive patches is given by the surface coverage factor [28],

$$\chi = n \sin^2\left(\frac{\delta}{2}\right) . \tag{2.9}$$

Within the present patchy model, only the square of χ appears in the average of u_{attr} over the angular degrees of freedom. The surface coverage factor χ is thus an additional, independent parameter in our anisotropic patchy model, and our calculations do *not* depend on the actual local distribution of patches and their individual sizes. All details of the discrete character of the pair interactions are convoluted in the surface coverage factor χ due to this angular-averaging. However, in place of χ one can use the opening angle δ as the adjustable parameter for n fixed, or, likewise, n is taken as adjustable and δ is fixed. Our calculations

have been performed such that δ is the independent parameter for n fixed to 2, as sketched in Fig. 1 of this thesis. With this form, an isotropic attractive potential is recovered in the limit $\delta \to \pi$.

The second osmotic virial coefficient, B_2, has the following form for an angular-dependent pair potential,

$$B_2(T) = -\frac{1}{2}\int d\mathbf{r}\,\langle \exp\left[-\beta u(r,\Omega_1,\Omega_2)\right]-1\rangle_{\Omega_1,\Omega_2}\,, \tag{2.10}$$

where

$$\langle \ldots \rangle_{\Omega_1,\Omega_2} = \frac{1}{(4\pi)^2}\int\int \ldots\, d\Omega_1 d\Omega_2 \tag{2.11}$$

denotes an unbiased angular average. The reduced second virial coefficient, B_2^*, is defined as the ratio of B_2 and the virial coefficient, $B_2^0 = 2\pi\sigma^3/3$, of hard spheres of diameter σ, i.e., $B_2^* = B_2/B_2^0$.

Lysozyme is approximately an ellipsoidal polypeptide with volume $v_0 = (\pi/6)\times 4.5\times 3.0\times 3.0\,\mathrm{nm}^3$ [19]. In the present work, we treat the ellipsoidal-like polypeptide as a spherical particle of equal volume v_0, and effective diameter $\sigma = 3.4\,\mathrm{nm}$ [15, 54, 55]. The molar mass of lysozyme is $14,400\,\mathrm{g/mol}$, and its mass density is $\rho_0 = 1.351\,\mathrm{g/cm}^3$. In the experiments, the proteins have been dissolved with a $c_\mathrm{b} = 0.02\,\mathrm{mol/l}$ (2-hydroxyethyl)piperazine-N'-(2-ethanesulfonic acid) (HEPES) buffer solution without added salt. The pH has been adjusted to 7.8 ± 0.1 using a sodium hydroxyl solution [56, 57]. At this pH-value it is known from titration experiments that the protein carries $Z = 8$ net positive elementary charges [58].

2.3 Helmholtz free energy and phase coexistence

In order to explore the phase diagram of lysozyme, we need to calculate the Helmholtz free energies of the fluid and solid phases. For this purpose, we employ the thermodynamic perturbation theory of Barker and Henderson [59], using hard spheres as the reference system. The Helmholtz free energy of the actual system is hereby expanded in powers of the interaction strength of the perturbational potential part, $u_\mathrm{p} = u - u_0$, with the hard-sphere reference system indicated by the subscript 0,

$$f(T,\eta) = f_0(\eta) + f_1(T,\eta) + f_2(T,\eta) + \ldots\,. \tag{2.12}$$

We have non-dimensionalised here the Helmholtz free energy, $F(N,V,T)$, of the proteins by the thermal energy $1/\beta = k_\mathrm{B}T$ and the volume per particle, $v_0 = \pi\sigma^3/6$, according to $f = \beta F v_0/V$, where N is the number of particles in the system volume V. The first-order perturbation contribution to the free energy contains only pair-wise interactions and is given by

$$f_1(T,\eta) \;=\; 12\,\eta^2 \frac{1}{\sigma^3}\int_\sigma^\infty dr\, r^2 g_0(r)\,\langle\,\beta u_{\rm p}(r,\Omega_1,\Omega_2)\,\rangle_{\Omega_1,\Omega_2}\,, \qquad (2.13)$$

where $g_0(r)$ is the radial distribution function of hard spheres of volume fraction η. In the solid phase, $g_0(r)$ is the orientationally averaged pair distribution function.

The second-order perturbation contribution, f_2, contains three- and four-body distribution functions and includes fluctuations in the particle density. Unfortunately, this contribution cannot be computed easily because of the complexity of these higher-order distribution functions. For this reason, we involve the macroscopic compressibility approximation developed by Barker and Henderson [60], which involves only the pair distribution function and the isothermal compressibility, $\chi_{\rm T}$, of the reference system according to

$$f_2(T,\eta) \;=\; -6\,\eta^2\left(\frac{\partial\eta}{\partial\Pi_0}\right)_{\rm T}\frac{1}{\sigma^3}\int_\sigma^\infty dr\, r^2\, g_0(r)\big\langle\,[\beta u_{\rm p}(r,\Omega_1,\Omega_2)]^2\,\big\rangle_{\Omega_1,\Omega_2}. \qquad (2.14)$$

Here, $\chi_{\rm T}/(\beta v_0) = 1/\eta(\partial\eta/\partial\Pi_0)_{\rm T}$, where we have non-dimensionalised the protein osmotic pressure, $\tilde{\Pi}_0$, according to $\Pi_0 \equiv \beta\tilde{\Pi}_0 v_0$.

In the fluid phase, the reduced free energy of the hard-sphere reference system, f_0, consists of the ideal gas part,

$$f_0^{\rm id}(\eta) = \eta\left[\ln(\eta\Lambda^3/v_0) - 1\right]\,, \qquad (2.15)$$

with the thermal wavelength, $\Lambda = h/\sqrt{2\pi m k_{\rm B}T}$, involving the protein mass m, Planck's constant h, and the interaction free energy part. The latter is described using the Carnahan-Starling equation of state [61],

$$f_0^{\rm CS}(\eta) = \frac{4\eta^2 - 3\eta^3}{(1-\eta)^2}\,. \qquad (2.16)$$

Solid lysozyme dispersions are known to have a tetragonal crystal structure [62]. Within our simplifying model, we have mapped the ellipsoidal-like particle shape onto a sphere, which allows us to use for simplicity the hard-sphere reference system which has a fcc solid phase. Existing schemes for g_0 in solids [63–66] have been developed and compared with Monte Carlo simulation data only for face-centred cubic (fcc) and body-centred cubic (bcc) lattices. For the excess Helmholtz free energy density of the fcc hard-sphere solid phase, we use Wood's equation of state [67], namely

$$f_0^{\rm solid}(\eta) = 2.1306\,\eta + 3\,\eta\ln\left(\frac{\eta}{1-\eta/\eta_{\rm cp}}\right) + \eta\ln\left(\frac{\Lambda^3}{v_0}\right), \qquad (2.17)$$

where $\eta_{\rm cp} = \pi\sqrt{2}/6$ is the fcc volume fraction for closed packing. The integration constant (i.e., the first term on the right-hand side of Eq. (2.17)) is obtained from

the free energy density of a hard-sphere crystal calculated from Monte Carlo simulations at $\eta = 0.576$ [68]. Note that different free energy expressions are used for the fluid and solid phases of the reference system, since there is a symmetry change in going from one phase to the other. For the radial distribution function, $g_0(r)$, in the liquid phase, we use the Verlet-Weis (VW) corrected [69, 70] Percus-Yevick (PY) solution [71, 72], and the orientation-averaged pair distribution function of Kincaid [66] for the fcc crystal phase.

The second-order perturbation scheme outlined above has been widely used for various perturbation potentials and compared with simulation data. For example, it has been used for approximating the free-energies of fluid or solid phases of particles with attractive [73] and repulsive [74] short-ranged pair potentials of Yukawa-type, and particles with polymer-induced depletion interactions [75–77]. As long as the contact value of the perturbation potential part is not much larger than $k_{\mathrm{B}}T$, so that u_{p} can be treated as a perturbation relative to the dominating hard sphere contribution, the perturbation scheme works decently well, provided u_{p} is not too long-ranged. In our calculations, the second-order free energy perturbation term is typically ten to twenty times smaller than the first-order contribution.

At fluid-solid phase coexistence, the two phases must be in thermal, mechanical, and chemical equilibrium. Since the coexisting phases are in thermal contact, the only two conditions determining the volume fractions of the coexisting fluid (f) and solid (s) phases are the equality of the osmotic pressure

$$\Pi_{\mathrm{f}}(T, \eta_{\mathrm{f}}) = \Pi_{\mathrm{s}}(T, \eta_{\mathrm{s}}) \,, \tag{2.18}$$

and chemical potentials,

$$\mu_{\mathrm{f}}(T, \eta_{\mathrm{f}}) = \mu_{\mathrm{s}}(T, \eta_{\mathrm{s}}) \,, \tag{2.19}$$

with

$$\Pi(T, \eta) = \eta^2 \left(\frac{\partial (f(T, \eta)/\eta)}{\partial \eta} \right)_{\mathrm{T}} \quad \text{and} \quad \beta\mu(T, \eta) = \left(\frac{\partial f(T, \eta)}{\partial \eta} \right)_{\mathrm{T}} . \tag{2.20}$$

At sufficiently low temperatures, a liquid (l) and a gas-like (g) phase of high and low density, η_{l} and η_{g}, respectively, coexist along the gas-liquid coexistence curve. The liquid-gas coexistence is metastable, however, with respect to a fluid-solid phase coexistence. Under gravity, the two fluid phases are separated by a meniscus, and particles and energy can pass through this interface. Equilibrium is achieved for equal osmotic pressures

$$\Pi_{\mathrm{g}}(T, \eta_{\mathrm{g}}) = \Pi_{\mathrm{l}}(T, \eta_{\mathrm{l}}) \,, \tag{2.21}$$

and chemical potentials,

$$\mu_{\mathrm{g}}(T,\eta_{\mathrm{g}}) = \mu_{\mathrm{l}}(T,\eta_{\mathrm{l}})\,, \tag{2.22}$$

of the coexisting phases.

The spinodal instability curve of diverging isothermal compressibility is determined by

$$\frac{\partial^2 f(T,\eta)}{\partial \eta^2} = 0\,. \tag{2.23}$$

The binodal and spinodal merge at the critical point (see later).

We have evaluated the improper integrals in the perturbation scheme using Chebyshev quadrature for the zonal part of $g_0(r)$ and Romberg quadratures for the remainder, where the perturbation pair potential has almost decayed to zero and the angular-averaged pair distribution is nearly constant. Higher-order derivatives of the free-energy have been computed to machine precision accuracy using Ridder's implementation of Neville's algorithm. The phase coexistence curves have been determined using a Newton-Raphson method with line search (see [78] for the invoked algorithms).

2.4 Determination of the attractive interaction parameters

We proceed by first characterising the yet unknown interaction parameters z_{attr} in Eq. (2.7) and ϵ_{attr} in Eq. (2.8), and compute subsequently the equilibrium phase diagram of lysozyme for the experimentally scanned part of the T - η plane. Aside from these two interaction parameters, there are two additional unknown parameters in our patchy sphere model, namely the parameter ψ in Eq. (2.8), which characterises the temperature-dependence of the depth of the attractive potential part, and δ, the opening angle of the patches (see Eq. (2.9)), which determines the surface coverage factor χ for the given number $n = 2$ of patches.

In a first attempt to determine these parameters, one could try to fit the binodal, obtainable in principal from our model, to the experimental one. However, the complexity of the involved thermodynamic expressions renders this direct approach very tedious. For simplicity, we choose a simpler strategy and focus on a characteristic point in the phase diagram, namely the critical point of the metastable gas-liquid protein phase coexistence. Right at the critical point, $u_{\mathrm{attr}}(r)$ is determined by z_{attr}, ϵ_{attr} and δ alone, since its depth becomes temperature-independent (see Eq. (2.8)). At the critical point, the second and third density derivatives of the Helmholtz free energy vanish, i.e.

$$\frac{\partial^2 f(T_{\mathrm{c}},\eta_{\mathrm{c}})}{\partial^2 \eta} = 0 \quad \text{and} \quad \frac{\partial^3 f(T_{\mathrm{c}},\eta_{\mathrm{c}})}{\partial^3 \eta} = 0\,. \tag{2.24}$$

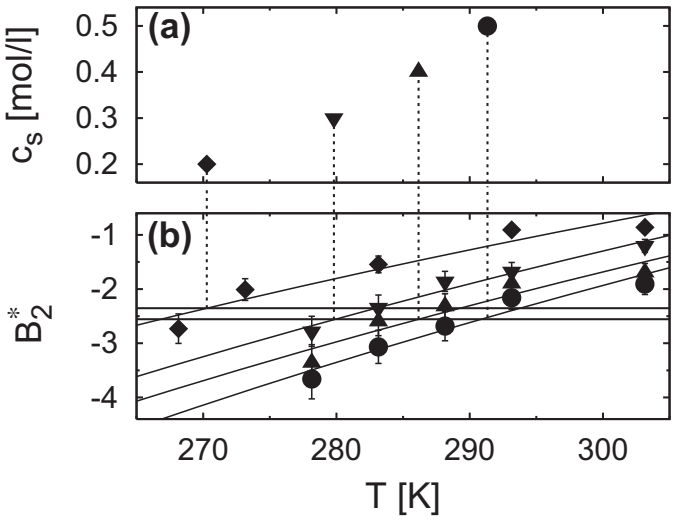

Figure 2.4: (a) Sodium chloride concentrations, c_s, at fixed buffer concentration, $c_b = 0.02\,\mathrm{mol/l}$ of HEPES buffer, corresponding to $p\mathrm{H} = 7.8$, for which the $B_2^*(T)$ values of lysozyme have been obtained from static light scattering experiments by Gibaud [79]. The vertical dashed lines mark the salt-concentration dependent critical temperature. (b) Experimentally obtained $B_2^*(T)$ versus T. The solid curves are best fits to the parametrisation $B_2^*(T, c_s) = 1 + A/T - B/T^2$, with the two parameters A and B determined for $c_s = 0.5\,\mathrm{mol/l}$ (●) as: $A = 3921\,\mathrm{K}$, $B = 1.4 \times 10^6\,\mathrm{K}^2$; $c_s = 0.4\,\mathrm{mol/l}$ (▲): $A = 3566\,\mathrm{K}$, $B = 1.3 \times 10^6\,\mathrm{K}^2$; $c_s = 0.3\,\mathrm{mol/l}$ (▼): $A = 3620\,\mathrm{K}$, $B = 1.3 \times 10^6\,\mathrm{K}^2$; $c_s = 0.2\,\mathrm{mol/l}$ (♦): $A = 2869\,\mathrm{K}$, $B = 1.0 \times 10^6\,\mathrm{K}^2$). See the text for additional explanation.

Here we use values for the critical temperature, T_c, and the volume fraction at the critical point, η_c, as determined experimentally by Gibaud [79] and Cardinaux *et al.* [49]. To obtain a third condition for the three unknown parameters, we exploit an empirical observation made by Warren, Egelhaaf and Poon [33, 55]. These authors find that the $B_2^*(T)$ of lysozyme is practically independent of the salt concentration for values larger than $c_s = 0.25\,\mathrm{mol/l}$, with a plateau value of $B_2^* = (-2.7 \pm 0.2)$. Hence, as an additional constraint, we demand that $B_2^*(T_c)$ is equal to

$$B_2^*(T_c) = -2.7\,. \tag{2.25}$$

This requirement is reasonable, since B_2^* is the second term in the density expansion of the Helmholtz free energy density, $f(T, \eta) = f_0^{\mathrm{id}}(\eta) + 4B_2^*(T)\eta^2 + \mathcal{O}(\eta^3)$, so that any viable model should at least reproduce this value correctly.

Gibaud [79] has experimentally determined the reduced second virial coefficient of hen egg lysozyme as a function of T (see Fig. 2.4(b)). These data for $B_2^*(T)$ are fitted (see the caption of Fig. 2.4 for details) to the form $B_2^*(T) = 1 + A/T - B/T^2$, and the so-determined second-order polynomial forms for $B_2^*(T)$ are used to rescale the experimental phase diagram In the upper chart of Fig. 2.4(a), the

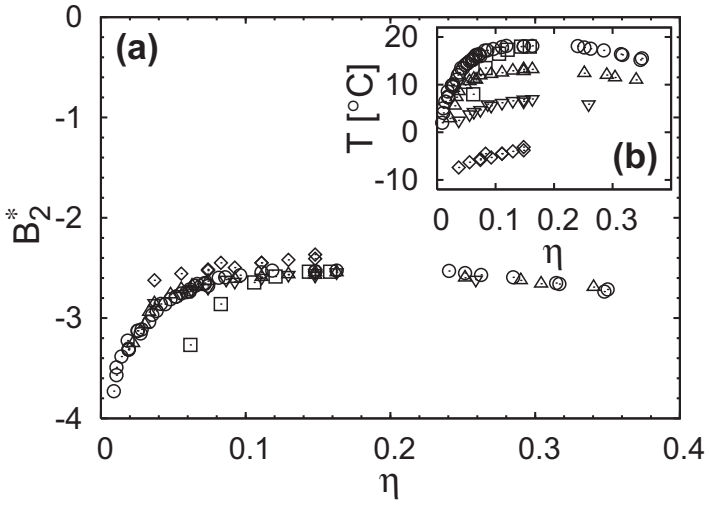

Figure 2.5: Reduced experimental phase diagram of aqueous lysozyme solutions at $c_\mathrm{b} = 0.02\,\mathrm{mol/l}$ HEPES buffer with $p\mathrm{H} = 7.8$ by Gibaud [79]. The data are consistent with earlier measurements summarised by Warren [33], where a value of $B_2^*(T_\mathrm{c}, \eta_\mathrm{c}) = (-2.7 \pm 0.2)$ is observed practically independent of c_s. The circles ($\circ$) describe the experimental gas-liquid coexistence curve for various salt content: $c_\mathrm{s} = 0.5\,\mathrm{mol/l}$ ($\circ$) [49], $c_\mathrm{s} = 0.4\,\mathrm{mol/l}$ ($\triangle$), $c_\mathrm{s} = 0.3\,\mathrm{mol/l}$ ($\triangledown$), and $c_\mathrm{s} = 0.2\,\mathrm{mol/l}$ ($\diamond$). The squares ($\square$) indicate the experimental spinodal [49]. In (a), the temperature has been replaced by the corresponding reduced second virial coefficient, $B_2^*(T, \eta, c_\mathrm{s})$, obtained from the parametrisation explained in Fig. 2.4. The inset (b) displays the binodal and spinodal for various c_s values in the T - η plane.

experimentally observed critical temperatures are indicated as vertical lines for various salt concentrations. The intercepts of these lines with the curves for $B_2^*(T)$ in Fig. 2.4 give the reduced second virial coefficient $B_2^*(T_\mathrm{c})$ at the salt-concentration dependent critical point. As can be seen, there is a narrow band of $B_2^*(T_\mathrm{c})$ values for which the fluid phase becomes unstable and separates into a gas and a liquid-like phase, supporting Eq. (2.25), and in accordance with the extended principle of corresponding states discussed by Noro and Frenkel [48]. Foffi and Sciortino [80] have recently shown, using computer simulations, that the principle of corresponding states holds also for non-spherical symmetrical pair interaction potentials. Rosenbaum and Zukoski [18] have demonstrated that the solubility curves collapse onto a single master curve when plotted in the B_2^* - η plane, or, likewise, in the τ-η plane, where τ is the stickiness parameter in the adhesive hard-sphere model considered by them. Fig. 2.5 shows additionally, on the basis of the data set by Gibaud [79], that the experimentally determined gas-liquid coexistence curves of lysozyme suspensions for various salt concentrations collapse onto a single curve when plotted in the B_2^* - η plane. Such a scaling behaviour of the gas-liquid coexistence curves is expected for systems interacting with short-ranged attractions, because the term containing B_2^* describes the

c_s [mol/l]	T_c [K]	z_{rep}	$\epsilon_{rep}/(k_B T_c)$	z_{attr}	$\epsilon_{attr}/(k_B T_c)$	δ [°]	χ
0.5	291.3	8.43	0.51	3.02	3.06	73.0	0.707
0.4	286.2	7.63	0.60	3.08	3.15	73.5	0.716
0.3	279.8	6.76	0.73	3.15	3.27	74.0	0.725
0.2	270.3	5.76	0.94	3.18	3.50	74.3	0.729

Table 2.1: System and pair potential parameters used in the thermodynamic perturbation calculation of the metastable gas-liquid binodal/spinodal, and the stable fluid-solid coexistence curve (for salt concentrations c_s as indicated). The attractive potential part parameters z_{attr} and $\beta\epsilon_{attr}$ are determined by Eqs. (2.24) and (2.25), respectively, using $Z = 8$ independent of η and c_s. For given c_s, the parameters z_{attr}, $\beta\epsilon_{attr}$ and δ (with a fixed value $n = 2$) are determined from the experimental values for $\eta_c(c_s)$, $T_c(c_s)$ and $B_2^* = -2.7$, with ψ fixed to 5.

mayor non-hard-sphere-like contribution to the Helmholtz free energy as we have noticed before. Therefore, B_2^* can be only a crude measure of the actual form of the pair interaction potential, and, as a consequence, is quite insensitive to small changes in the interaction parameters. A case in point will be the gas-liquid coexistence curves discussed in the following (see, especially, Fig. 2.7).

The so far unknown parameters, z_{attr}, ϵ_{attr}, and δ, characterising the attractive pair interaction part can now be obtained numerically from solving the set of nonlinear algebraic Eqs. (2.24) and (2.25). The additional free parameter ψ in Eq. (2.8) mainly determines the width of the coexistence curve. Its value will be adjusted when we compare the calculated and experimental binodals and spinodals (see below).

At this point we emphasise, that the second-order perturbation term in Eq. (2.14) is a necessary contribution which allows to fix χ independently of ϵ_{attr}. Carrying out the angular average results in a factor of χ^2. When the first-order perturbation term is considered alone, χ^2 and ϵ_{attr} appear only as a product. Thus, one can not choose χ (or, respectively, δ at fixed n) and ϵ_{attr} independently when the first-order perturbation contribution to the free energy of the reference hard-sphere system in Eq. (2.12) is considered only.

In the present second-order perturbation theory, density fluctuation effects are ignored, which in general lower the critical temperature. However, the fluctuations become less important with increasing range of the pair interactions [81], since the number of particles contributing to the force experienced by a central one increases with increasing range of attraction, so that the mean-field picture becomes more accurate (see, e.g., Fig. 1 in [82]). Thus, we can expect that the fluctuation-induced shift of the critical point is rather small in lysozyme solutions, as argued also earlier by Sear and Gelbart [42].

The parameters determined by the evaluation strategy described above are

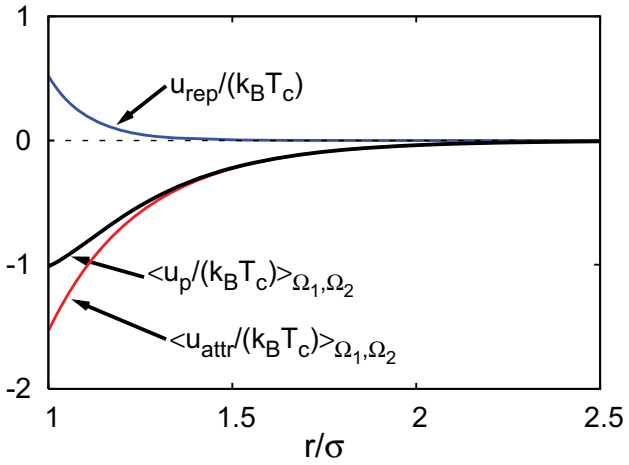

Figure 2.6: Repulsive electrostatic pair potential part, $u_{\rm rep}/(k_{\rm B}T_{\rm c})$ (blue curve), angular-averaged attractive interaction part, $\langle u_{\rm attr}/(k_{\rm B}T_{\rm c})\rangle_{\Omega_1,\Omega_2}$ (red curve), and total perturbational pair potential, $\langle u_{\rm p}/(k_{\rm B}T_{\rm c})\rangle_{\Omega_1,\Omega_2}$ (black curve), for parameters at the critical point where $c_{\rm s} = 0.5\,$mol/l, using $\eta_{\rm c} = 0.17$, $T_{\rm c} = 291.3\,$K. The parameters used in the perturbational interactions for the attractive and repulsive Yukawa-type potential parts are listed in Table 2.1. At larger r, $\langle u_{\rm p}/(k_{\rm B}T_{\rm c})\rangle_{\Omega_1,\Omega_2}$ is dominated by the attractive interaction part.

summarised in Table 2.1. Note that the range of the screened Coulomb repulsion, $1/z_{\rm rep}$, and its strength, $\beta\epsilon_{\rm rep}$, show the expected increase with decreasing salt concentration. The temperature dependency of the Bjerrum length, through $\varepsilon(T)$, has been accounted for. However, in the considered temperature range, $l_{\rm B}$ is only mildly dependent on T.

Due to the stronger electrostatic repulsion between the proteins on lowering the salt concentration, $T_{\rm c}$ decreases with decreasing salt concentration. Fig. 2.6 shows the repulsive potential part, $u_{\rm rep}(r)$, the angular-averaged attractive potential part, $\langle u_{\rm attr}(r)\rangle_{\Omega_1,\Omega_2}$, and the angular-averaged total perturbation potential, $\langle u_{\rm p}(r,\Omega_1,\Omega_2)\rangle_{\Omega_1,\Omega_2}$, obtained at the critical concentration for $c_{\rm s} = 0.5\,$mol/l. Note that the contact value, $\epsilon_{\rm attr}/(k_{\rm B}T_{\rm c})$, of the *non-angular*-averaged attractive pair potential at $T_{\rm c}$ given in Table I, is well above $3\,k_{\rm B}T_{\rm c}$. In contrast, Figs. 2.6 and 2.7 show the *angular*-averaged attractive interaction part, with contact value $\langle u_{\rm attr}(\sigma)/(k_{\rm B}T_{\rm c})\rangle_{\Omega_1,\Omega_2} = \chi^2\epsilon_{\rm attr}/(k_{\rm B}T_{\rm c})$. Thus, the angular-averaged contact value of the attractive part is smaller than $3\,k_{\rm B}T_{\rm c}$ (see Figs. 2.6 and 2.7).

The range, $1/z_{\rm attr}$, and depth, $\beta\epsilon_{\rm attr}$, of the attractive Yukawa potential exceed the range, $1/z_{\rm rep}$, and strength, $\beta\epsilon_{\rm rep}$, respectively, of the repulsive part, so that the averaged perturbation pair potential is purely attractive. Actually, this finding holds true for all salt concentrations considered, as can be noticed from Fig. 2.7. Due to the weaker screening of the protein surface charge at lower salt content, c_s, the attraction range of the total potential decreases with decreasing

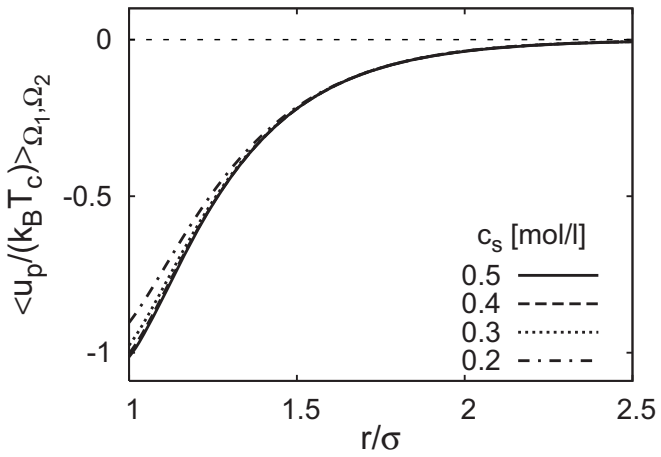

Figure 2.7: Angular-averaged total perturbation potential, $u_\mathrm{p} = u - u_0$, (see Eq. (2.1)) for various salt concentrations as indicated. With decreasing c_s, the contact value of $\langle u_\mathrm{p}/(k_\mathrm{B}T_\mathrm{c})\rangle_{\Omega_1,\Omega_2}$ decreases due to the enlarged range of the electrostatic repulsion part.

amount of salt. However, in contrast to the drastic change of the repulsive interaction part with c_s, the parameters of the attractive potential part vary only slightly with the salinity. The range of attraction, $1/z_\mathrm{attr}$, shrinks by 6% only when c_s is reduced from 0.5 to 0.2 mol/l, whereas the attraction strength, $\beta\epsilon_\mathrm{attr}$, increases by 14%. According to our calculations, the opening angle δ, and thus the surface coverage χ, increase only slightly with decreasing salinity. These changes in χ and δ are negligible as compared to the strong influence of the salinity on the electrostatic screening length. Therefore, we can conclude that in our model the range and strength of the radially averaged attractive potential part is approximately constant within the salt range considered.

We have carefully checked the sensitivity of the calculations to small changes in the employed parameters. Changing B_2^* from -2.7 to -2.5 or, likewise, to -2.9, and keeping all other parameters unchanged, leads to changes in z_attr and $\beta\epsilon_\mathrm{attr}$ by less than 5%, whereas the surface coverage factor is affected by 2% only. Varying the bare protein charge number $Z = 8$ by ± 2, keeping again all other parameters fixed, changes both z_attr and $\beta\epsilon_\mathrm{attr}$ by less than 6%, and χ by less than 3%. As expected, our calculations are more sensitive to variations in the critical volume fraction: Assuming an uncertainty of 10% in the experimental η_c, say $\eta_\mathrm{c} = (0.17 \pm 0.02)$, z_attr changes by up to 29%, whereas $\beta\epsilon_\mathrm{attr}$ is changed by 6%, and χ by 3%. An uncertainty in the protein diameter of ± 0.2 nm [16] causes deviations in z_attr and $\beta\epsilon_\mathrm{attr}$ by less than 4 %, and in χ by less than 2 %.

We note that an alternative strategy to extract the interaction parameters from the experimentally observed phase diagrams is described in appendix B. In this alternative strategy we fix the distance between the solubility curve and

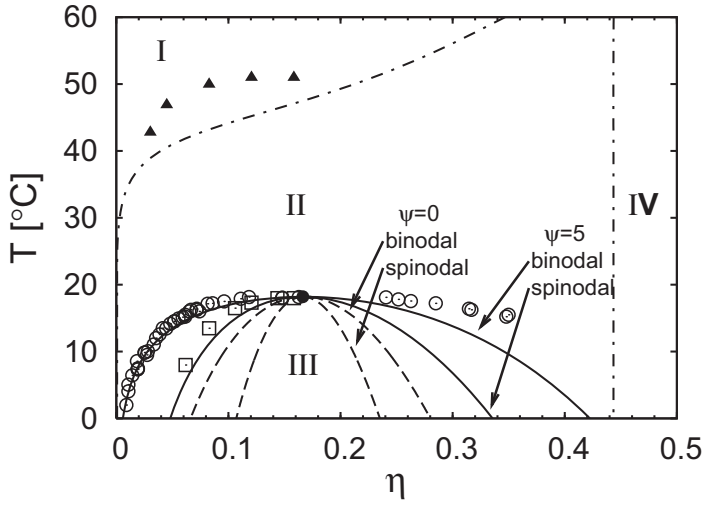

Figure 2.8: The phase diagram of aqueous lysozyme solutions for $c_\mathrm{b} = 0.02\,\mathrm{mol/l}$ HEPES buffer, and $p\mathrm{H} = 7.8$, $c_\mathrm{s} = 0.5\,\mathrm{mol/l}$ NaCl. The circles (○) describe the experimentally found metastable gas-liquid coexistence curve [49], the squares (□) indicate the spinodal [49], and the black triangles (▲) depict the experimental fluid-crystal coexistence curve [79]. The two dashed curves show the calculated binodal and spinodal, respectively, for $\psi = 0$. The two solid curves describe the calculated binodal and spinodal, respectively, where the two curves account for an additional temperature dependence of the attractive potential depth with $\psi = 5$ (see Eq. (2.8)). The dashed-dotted curves are the calculated fluid-crystal coexistence curves for $\psi = 5$, with the interaction parameters determined from the experimental data at the critical point as explained in the text. In region I, a stable fluid phase is observed, whereas one finds a fluid-crystal coexistence in region II, a metastable gas-liquid coexistence in region III, and a pure crystalline phase in region IV.

the binodal at T_c. Through this we can directly obtain ψ without adjusting this parameter by hand as described above. However, the so-obtained interaction parameters, in particular ψ, differ only slightly from the former and result in a similarly good agreement with the experimentally observed phase diagram.

2.5 Calculated phase diagrams

In Fig. 2.8, the phase diagram is shown for the largest salt concentration considered of $c_\mathrm{s} = 0.5\,\mathrm{mol/l}$. As can be seen from this figure, the predicted gas-liquid coexistence curves are too narrow when $\psi = 0$ is used (dashed curves). To correct for this, we have introduced the temperature-dependent coupling parameter, $\tilde{\epsilon}_\mathrm{attr}$, in Eq. (2.8), which includes the parameter ψ. Positive values of ψ widen the unstable region in the calculated phase diagram, because of the increase in the strength of attraction. From calculating the binodals (solid curves) for a variety of ψ values, and comparing them with the experimental data points at

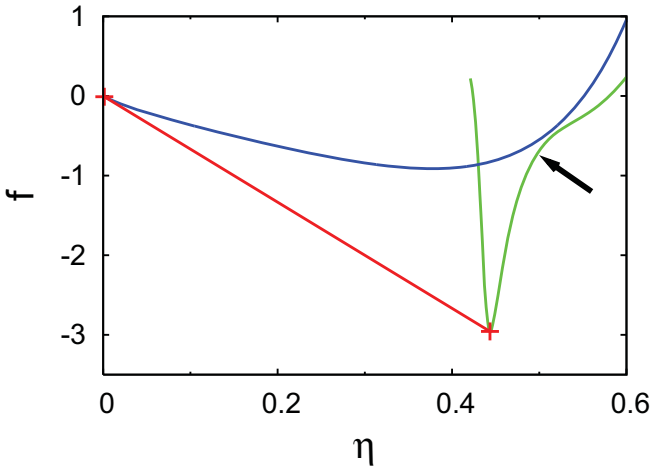

Figure 2.9: Reduced free energy of the fluid and solid phase as a function of the volume fraction in a lysozyme dispersion with $c_s = 0.5\,\mathrm{mol/l}$ for $T = 300\,\mathrm{K}$. The fluid branch is indicated by a blue and the solid branch by a green curve. The fluid-crystal coexistence points are marked by crossed and are connected by a red solid line according to the common tangent construction. The arrow emphasis the van der Waals loop of the reduced free energy in the solid branch. This indicates the existence of an isostructural solid-solid phase coexistence predicted in our model (see text for further remarks).

$c_s = 0.5\,\mathrm{mol/l}$, we find good agreement, using a value $\psi = 5$, for all volume fractions smaller than twenty percent. At larger volume fractions, the calculated binodals deviate somewhat from the experimental ones. We note, however, that changing ψ by not more than 40% does not crucially affect the overall good agreement between experimental and calculated binodals and spinodals.

The range, $1/z_{\mathrm{attr}}$, and the strength, $\beta\epsilon_{\mathrm{attr}}$, of the attractive potential part, obtained for one specific salt concentration ($c_s = 0.5\,\mathrm{mol/l}$) at the critical point, have been fixed in calculating the coexistence curves also for the other values of c_s considered. The binodal and the fluid-crystal coexistence curves have been calculated according to the double tangent construction, using Eqs. (2.18) and (2.19). The spinodal curve follows from the condition that the isothermal compressibility diverges (see Eq. (2.23)).

In Fig. 2.9, the reduced free energy is plotted for $T = 300\,\mathrm{K}$, where a symmetry-breaking fluid-solid phase transition takes place. The volume fractions of the coexisting fluid and crystal phase is found according to the common tangent construction (solid red line) which minimises the reduced free energy at constant pressure and chemical potential. Interestingly enough, the crystal branch of the free energy shows a van der Waals loop indicating a isostructural solid-solid phase transition predicted by our model (see arrow in Fig. 2.9). Because such an isostructural solid-solid phase transition has not been reported in experiments,

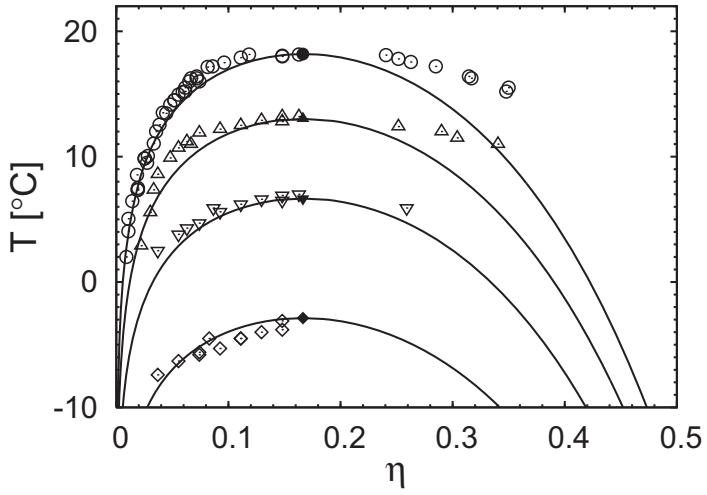

Figure 2.10: Gas-liquid coexistence curves of a lysozyme solution obtained experimentally by Cardinaux *et al.* [49] and Gibaud [79] from temperature quenches at four different salt concentrations : $c_s = 0.5\,\mathrm{mol/l}$ (○), $0.4\,\mathrm{mol/l}$ (△), $0.3\,\mathrm{mol/l}$ (▽), and $0.2\,\mathrm{mol/l}$ (◇). The filled symbols mark the critical points estimated from the experiment. The solid curves describe the coexistence curves as calculated from our model using a fixed value $\psi = 5$.

and due to the simplified description of the crystal free energy in our model, we have refrained from including this solid-solid phase coexistence curve into our discussion of the phase behaviour of lysozyme dispersions. Note however, that a similar isostructural solid-solid phase transition has been predicted in earlier simulations by Frenkel on attractive spherical colloids [83].

In Fig. 2.10, finally, the calculated gas-liquid coexistence curves are shown for four different salt concentrations in comparison with the experimental data points. We could have adjusted the parameter ψ for each c_s separately. However, we find that fixing it to $\psi = 5$ results in binodals that describe the experimental ones quite well for all salinities. For each c_s considered, the binodal curve is described reasonably well for low volume fractions, whereas, as discussed before, our model underestimates the transition temperature systematically at higher protein concentrations. This might be due to a salt partitioning over the two phases which is not accounted for in our model calculations [16, 33].

2.6 Isothermal compressibility

The isothermal compressibility, $\chi_T/\chi_T^{id} = S(q \to 0)$, $1/\chi_T^{id} = k_B T\eta/v_0$, has been extracted from scattering experiments at various lysozyme volume fractions for $T = 20^o\mathrm{C}$ and $T = 30^o\mathrm{C}$, respectively (see Fig. 6.3(a) in [79]). These systems

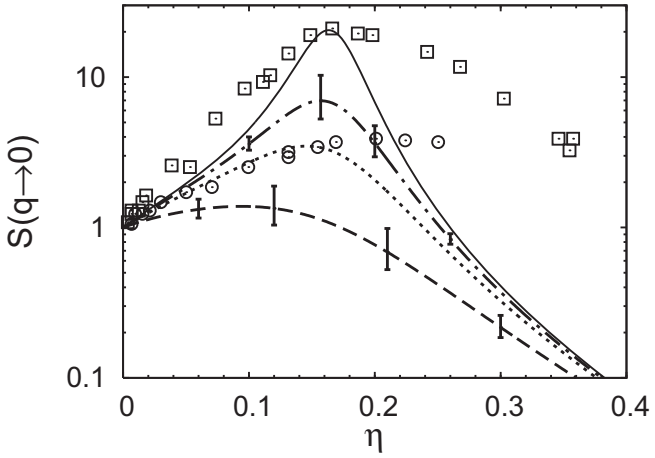

Figure 2.11: Isothermal osmotic compressibility, $\chi_{\mathrm{T}}/\chi_{\mathrm{T}}^{\mathrm{id}} = S(q \to 0)$, calculated using the second-order perturbation free energy density in the fluid phase for $c_{\mathrm{s}} = 0.5\,\mathrm{mol/l}$, $c_{\mathrm{b}} = 0.02\,\mathrm{mol/l}$, and $p\mathrm{H} = 7.8$. The dash-dotted curve is obtained for $T = 20^o\mathrm{C}$ and $\psi = 5$, and the dashed curve for $T = 30^o\mathrm{C}$ and $\psi = 5$. The error bars correspond to an uncertainty in ψ of $\Delta\psi = \pm 2$. The solid curve, corresponding to $T = 20^o\mathrm{C}$, and the dotted curve, corresponding to $T = 30^o\mathrm{C}$, are obtained using $\psi = 1$. The squares ($\square$) mark the experimental data at $T = 20^o\mathrm{C}$ and the circles ($\circ$) indicate the experimental data at $T = 20^o\mathrm{C}$ [79] (see the text for additional discussion).

are all located within the fluid-solid coexistence region above the critical point. The measurements have been made before the phase separation has been established, so that in fact they characterise *non-equilibrium* states. It is interesting to compare the scattering data with the equilibrium isothermal compressibility as estimated from our perturbative free energy calculations using the fluid branch of the Helmholtz free energy density. In equilibrium, and for a *homogeneous* one-phase system, the isothermal osmotic compressibility is related to the second-order density derivative of the free energy density according to

$$\frac{\chi_{\mathrm{T}}}{\chi_{\mathrm{T}}^{\mathrm{id}}} = \frac{1}{\eta}\left(\frac{\partial^2 f(T,\eta)}{\partial \eta^2}\right)^{-1} = S(q \to 0). \tag{2.26}$$

Fig. 2.11 shows the isothermal compressibility obtained from our patchy model calculations. Therein, we also display the error bars in $S(q \to 0)$ resulting from an uncertainty of ± 2 in the factor ψ, as discussed earlier in section 2.5. As can been seen, the calculated values for $\chi_{\mathrm{T}}/\chi_{\mathrm{T}}^{\mathrm{id}}$ underestimate the experimental $S(q \to 0)$. However, as discussed before, the width of the binodal and the distance between the fluid-solid coexistence curve and the binodal at T_{c} depend sensitively on the parameter ψ quantifying the T-dependence of the contact value of $\tilde{u}_{\mathrm{attr}}(r)$. Thus, if we determine ψ to match the experimental data for $S(q \to 0)$, then the best agreement is found for $\psi = 1$ for both temperatures considered. Albeit there is no quantitative agreement with the neutron scattering data for $\psi = 5$, the non-

monotonic density dependence of $S(0)$, and the location of the maximum, are well reproduced. Recall here again that the measurements of $S(0)$ have been made at state points where the solution is in the process to undergo a fluid-solid phase separation. Hence, one should be cautious when comparing these experimental data for a non-equilibrium situation with our perturbation results expression for the homogeneous fluid branch of the free energy.

2.7 Discussion

The virtue of our patchy model potential as compared to using a square-well potential alone [26,27,29], is that we account explicitly for the screened electrostatic repulsion. Through this model extension, we can distinguish the influence of the excess salt concentration from the attractive potential part that to date is not well-understood in its details. For the attractive part, in turn, we have adopted a simplifying patchy model that is of Yukawa-type in its radial factor. We have determined the interaction parameters characterising u_{attr} from the experimental data for the values of T_{c}, η_{c}, and $B_2^*(T_{\mathrm{c}})$ of lysozyme at the critical point. Using these experimental data at the critical point, we find an attractive range of $0.33\,\sigma$ at $c_{\mathrm{s}} = 0.5\,\mathrm{mol/l}$, and $0.31\,\sigma$ at $c_{\mathrm{s}} = 0.2\,\mathrm{mol/l}$. These ranges of attraction are consistent with corresponding findings by several authors as summarised by Lomakin *et al.* (see their Fig. 5 in [27]). In fact, such an intermediately extended range of attraction is very remarkable, since for a *purely* isotropic attractive pair potential of Yukawa-type one would expect a stable gas-liquid coexistence region for attractive range exceeding $0.17\,\sigma$ (or, correspondingly, for $z_{\mathrm{attr}} < 6$) [73, 84]. In the present case of an attractive and repulsive pair interaction potential of Yukawa-type, the fluid phase is stabilised against gas-liquid phase separation by the charge-induced electrostatic repulsion, which shifts the gas-liquid critical point below the solubility curve, and thus, give rise to a metastable binodal. We note that the range of attraction of $(1.0 \pm 0.1)\,\mathrm{nm}$ ($\sim 0.3\,\sigma$), experimentally found by Israelachvili and Pashley [85] from measuring the force between two hydrophobic plates, is in excellent accord with our findings.

In a number of previous studies, the isotropic and rather short-range DLVO pair potential has been used to fit the experimental scattering data on lysozyme [13,15,54]. To make contact with this earlier work, consider now a purely isotropic pair interaction by setting $\chi = 1$ in our model. In the isotropic case, we obtain $1/_{z_{\mathrm{attr}}} = 0.36$, using the same method to determine the attractive part as in the non-isotropic case. This attraction range, in fact, is nearly identical to the one observed for the anisotropic case, since the critical volume fraction depends only weakly on the patchiness [28]. On the other hand, the potential depth for $\chi = 1$ is given by $\beta\epsilon_{\mathrm{attr}} = 1.39$, corresponding to $B_2^*(T_{\mathrm{c}}) = -1.26$. This value for $B_2^*(T_{\mathrm{c}})$ obtained from assuming isotropic attractions, disagrees strongly with the experimentally observed value $B_2^*(T_{\mathrm{c}}) = -2.7$. In contrast, our patchy model

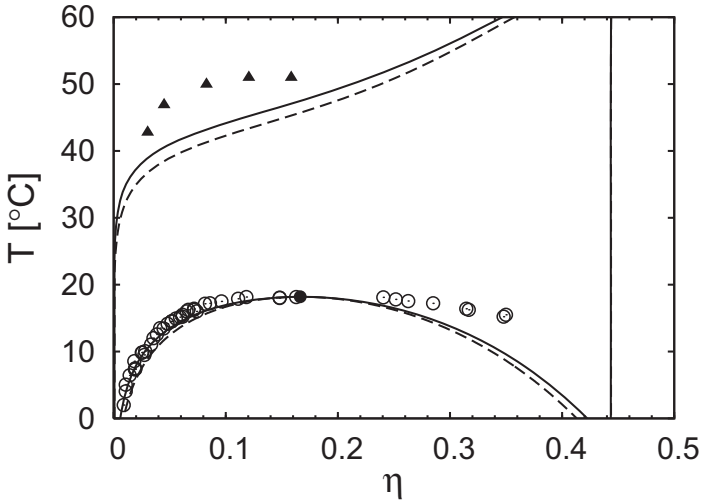

Figure 2.12: Phase diagram of lysozyme for $c_s = 0.5\,\mathrm{mol/l}$ NaCl, $c_b = 0.02\,\mathrm{mol/l}$ HEPES buffer, and pH = 7.8. The symbols indicate the experimental data points identical to the ones in Fig. 2.8 [49, 79]. The solid curves describe the equilibrium phase diagram obtained from the anisotropic model. For comparison, the dashed lines describe the gas-liquid and fluid-solid coexistence curves as obtained from a purely isotropic pair potential. In both cases, ψ is set equal to 5.

for $\chi < 1$ is capable to describe the experimental data, and it accounts for the influence of added salt.

In Fig. 2.12, we compare the gas-liquid and fluid-solid coexistence curves, for an isotropic interaction potential where $\chi = 1$, with the results from our anisotropic model from Fig. 2.8. As can be seen, the fluid-solid coexistence curve is shifted only slightly to lower temperatures when an isotropic pair interaction potential is assumed. Hence, isotropic attractive pair interactions for the protein solution result in a solubility curve located further below the experimental data, for interaction parameters determined again at the experimental critical point. Even in the isotropic case, the gas-liquid coexistence curve remains metastable relative to the fluid-solid coexistence curve, which might be due to the effect of the competing repulsive and attractive interactions. Such a weak influence of the patchiness on the location of the coexistence curves is expected in our model calculations since only the orientationally-averaged pair potential enters into the free energy expression. In fact, the angular-averaged contact value $\langle \beta\epsilon_{\mathrm{attr}} \rangle_{\Omega_1,\Omega_2} = \chi^2 \beta\epsilon_{attr} = 1.53$ (see Table 2.1), obtained using an anisotropic pair interaction potential, differs only mildly from the contact value, $\beta\epsilon_{\mathrm{attr}} = 1.39$, for the isotropic pair potential. However, the fact that the calculated B_2^* for an isotropic interaction potential disagrees by a factor of two with the experimentally observed virial coefficient, and the observation that the fluid-solid curve is located further below the experimental data than the one for anisotropic interactions implies that the experimental

data can be consistently described only for an anisotropic pair interaction. Furthermore, our phase boundary calculations for isotropic versus anisotropic interactions highlights why in earlier calculations on the phase behaviour of lysozyme, based on assuming a short-ranged isotropic pair potential, qualitative agreement with the experimental data has been achieved. In fact, aside from the totally wrong prediction for $B_2^*(T_c)$, an isotropic attractive pair potential can result in a reasonably good qualitative agreement with the experimental phase coexistence curves.

Carpineti *et al.* [46] discuss the need to account for hydrophobic patches in order to explain the temperature dependence of the solubility curve. Our model calculations conform to their findings, since the experimental data are recovered with the correct B_2^* only for $\chi \neq 1$. Curtis *et al.* [47] have argued that 51 % of the lysozyme surface area is hydrophobic, a value not too different from the surface coverage factor found in our work (we obtained $\chi = 71 - 73\,\%$). This discrepancy between the experimentally estimated χ-value and the one observed from our model might be explained by microion correlation effect which have not been accounted for within the one-component macroion fluid model used in our calculations. As shown by Allahyrov *et al.* [44], correlation effects between the microionic co- and counterions due to their finite sizes reduce the strength of the repulsive macroion-macroion pair interactions potential significantly already at salt concentrations above $c_s = 0.1\,\mathrm{mol/l}$. This is due to the fact that the size of the microions in aqueous solution ($\sim 0.2\,\mathrm{nm}$) is not small compared to the macroion size ($\sim 3.6\,\mathrm{nm}$). Thus, we presumably overestimate somewhat the strength of the screened electrostatic repulsions by neglecting such correlation effects, and, as a consequence, we overestimate the strength of attraction, i.e. χ, within our simple model. Curtis *et al.* [47] conclude further from their experimental data that the non-polar (hydrophobic) area on the protein surface shrinks by the addition of sodium chloride (see Table 2.1), in agreement with our findings. Our phenomenological description of the hydrophobic interactions between adjoined patches using a Yukawa-like attractive interaction potential part indicates that these interactions are only slightly affected by the salt concentration. All the experimental binodals for $c_s = 0.2$, 0.3, 0.4 and $0.5\,\mathrm{mol/l}$ can be well described using a fixed value of $\psi = 5$ (see Fig. 2.10). Only the prefactor, ϵ_{attr}, and χ decrease slightly with increasing c_s (see Table 2.1). Thus, the main effect of salt is to screen the lysozyme net charges.

To arrive at a deeper physical understanding of the strong temperature dependence of the attractive interaction part, as indicated in lysozyme solutions by a non-zero value of $\psi = 5 \pm 2$ (see section 2.5), is a demanding task, since little is known so far about the underlying molecular mechanism [86].

Some progress on the microscopic understanding of the attractive interactions has been made only very recently by Horinek *et al.* [87]. Their main observation is that the force between two hydrophobic objects is caused by two contributions of comparable strength; namely van der Waals attractions and water-

structure effects. Because the van der Waals attractions are to a first approximation temperature-independent, on neglecting the trivial temperature dependence due to the Boltzmann weight of the Hamiltonian, we attribute the strong temperature dependence in lysozyme solutions, indicated by a non-zero value of $\psi = 5 \pm 2$, mainly to the change in the water structure close to the hydrophobic surface [88]. Lomakin and co-workers [27], who used an aeolotopic model to describe the phase behaviour of γ-crystallin protein solutions, have arrived earlier at a similar conclusion by pointing to the strong temperature dependence of the attractive interactions (see p. 1655 in Ref. 27). Furthermore, they found a comparable value of $\psi = 3$ for γ-crystallin protein dispersions. These authors propose alternatively that the extended width of the gas-liquid coexistence might also be due to the discrete and anisotropic character of the hydrophobic interactions. Using computer simulations, Kern and Frenkel [28] showed that the gas-liquid coexistence curves can broaden significantly for sufficiently short-ranged attractive pair potentials and low surface coverage. Within our simple model we cannot distinguish whether the broadening of the gas-liquid coexistence curve is due to a strong temperature dependence or to the patchiness.

Understanding protein crystallisation is a complex issue. The dashed-dotted fluid-crystal coexistence curve in Fig. 2.6 deviates to some extent from the experimental data at higher volume fractions. However, aside from this, the calculated phase diagram agrees qualitatively with the experimental one regarding the metastability of the gas-liquid coexistence curve, and the extent of the gap between the critical point and the fluid-solid coexistence curve. In addition, our model predicts correctly a crystalline phase at remarkably low volume fraction as often observed in protein solutions [89]. In recent work [26, 90, 91], it has been demonstrated that the specific geometry, i.e., the number of patches, their size and their distribution across the surface, significantly affects the ability to form crystals, the nucleation kinetics and the crystalline order. In particular, crystallisation is expected to be hindered whenever the preferred local order in the liquid state is incompatible to the crystalline space symmetry. One speaks then of a "frustrated" liquid state [91]. In this case, the pair potential is no longer angularly averageable to describe the solid state [26]. Furthermore, McManus *et al.* [92] have shown for human γD-crystallin proteins, that angular-averaging is a feasible simplification to describe the fluid phase in its dependence on the number of spots on the protein surface, whereas the discrete patchiness influences crucially the solubility curve. One can speculate that this applies also to lysozyme dispersions.

2.8 Conclusions

Using thermodynamic perturbation theory, we have studied the phase behaviour of lysozyme dispersions on the basis of a pair potential consisting of a repulsive DLVO-type screened Coulomb part plus a patchy attractive part.

The strength and the range of the attractive radial potential factor of Yukawa-type, and the surface coverage of patches, have been determined using the experimentally known values for the concentration, temperature and reduced second virial coefficient of lysozyme at the metastable gas-liquid critical point. With the so-determined patchy pair potential, we have calculated the metastable gas-liquid coexistence and the spinodal curves of lysozyme solutions, and the fluid-solid coexistence curve, using the compressibility approximation of second-order thermodynamic perturbation theory. The shape of the computed phase diagram conforms overall quite well with the experimental data, in particular regarding the salt dependence of the coexistence curve, and the width of the gap in between the binodal and the fluid-solid coexistence curves. The percentage of surface coverage of patches ($\sim 70\%$) obtained in our model, and the interaction range of about 30% of the diameter, and the temperature-dependence of the attractive interaction part, as well as the salt-dependence of the interaction strength, are consistent with previous findings. This consistency is encouraging and supports the applicability of our simple model to describe lysozyme solutions. To obtain the solubility curve more accurately, however, might require to account for the patch geometry explicitly, without invoking an orientational pre-averaging.

A One-component macroion-fluid potential

Belloni [51] provides an analytic expression for the effective pair potential in Eq. (2.3), using the mean-spherical approximation (MSA) for the direct correlation functions and on assuming point-like microions. Within this level of approximation, the DLVO potential part is corrected by a factor X depending on the reduced inverse screening length $\kappa\sigma/2$ and the macroion volume fraction η, according to

$$X = \cosh(\kappa\sigma/2) + U\left[\kappa\sigma/2\cosh(\kappa\sigma/2) - \sinh(\kappa\sigma/2)\right], \tag{A.1}$$

where

$$U = \frac{z}{(\kappa\sigma/2)^3} - \frac{\gamma}{\kappa\sigma/2}, \tag{A.2}$$

and

$$\gamma = \frac{\Gamma\sigma/2 + z}{1 + \Gamma\sigma/2 + z}, \tag{A.3}$$

with $z = 3\eta/(1-\eta)$. The positive valued MSA screening parameter, Γ, is uniquely obtained from solving the following quartic relation:

$$\Gamma^2 = \kappa^2 + \frac{q_0^2}{(1+\Gamma\sigma/2+z)^2}\,, \tag{A.4}$$

where $q_0 = \sqrt{4\pi l_{\mathrm{B}}\rho}\,Z$. In the infinite dilute limit, $\rho \to 0$, Γ reduces to the inverse Debye screening length κ. For an extension of Belloni's expression to differently sized and charged colloidal spheres, see [93].

Because of the presence of the surrounding macroions in a concentrated colloidal dispersion, the screening ability of the microions is reduced. Therefore, the electrostatic repulsion between two macroions increases as compared to the DLVO limit and, thus, $X > X_0$. Due to the fact that non-zero colloid concentrations lead within the MSA only to a correction of the DLVO potential prefactor, X_0, one can define an effective number of charges, Z_{eff}, according to $Z_{\mathrm{eff}}/Z = X/X_0$ [51]. As shown in Fig. A1(c), Z_{eff}/Z increases rapidly with increasing η and decreasing salt concentration. According to Fig. A1 (a) and (b), the contact value of the macroion-macroion radial distribution, $g_{00}(\sigma^+)$, and the macroion-microion radial distribution function, $g_{0\mathrm{i}}(\sigma^+)$, as a function of η for $c_{\mathrm{s}} = 0.2\,\mathrm{mol/l}$, $0.3\,\mathrm{mol/l}$, $0.4\,\mathrm{mol/l}$ and $0.5\,\mathrm{mol/l}$. The contact value of the radial distribution functions increases with increasing volume fraction, and decreases with decreasing salt concentration. As can be seen, the contact values are non-negative for all η-values considered indicating the applicability of the linear MSA schema. We note that non-linear screening effects are not included in the linear MSA treatment. Non-linear screening caused by the quasi-condensation of counterions close to the surface of strongly charged colloids and biomolecules give rise to an effective charge that is, in general, smaller than the bare one (see, e.g., [69]).

B Phase diagram using the distance between the fluid-solid coexistence curve and binodal as an input

Instead of adjusting the parameter ψ to match the calculated binodal to the experimental one, we can determine ψ alternatively by matching, at temperature T_{c}, the vertical distance between the experimental and theoretical fluid-solid and gas-liquid coexistence curves. This alternative procedure proceeds as follows: there are in total five unknown parameters in our model, namely, the range of attraction, z_{attr}, the contact value, ϵ_{attr}, the parameter ψ describing the strength of the temperature dependence at contact, the opening angle δ of a patch, and the volume fraction, η_{s}, of the crystalline phase. In contrast to the first method used earlier, where ψ has been adjusted once z_{attr}, ϵ_{attr} and δ have been determined at the critical point, all five parameters are adjusted now simultaneously using the

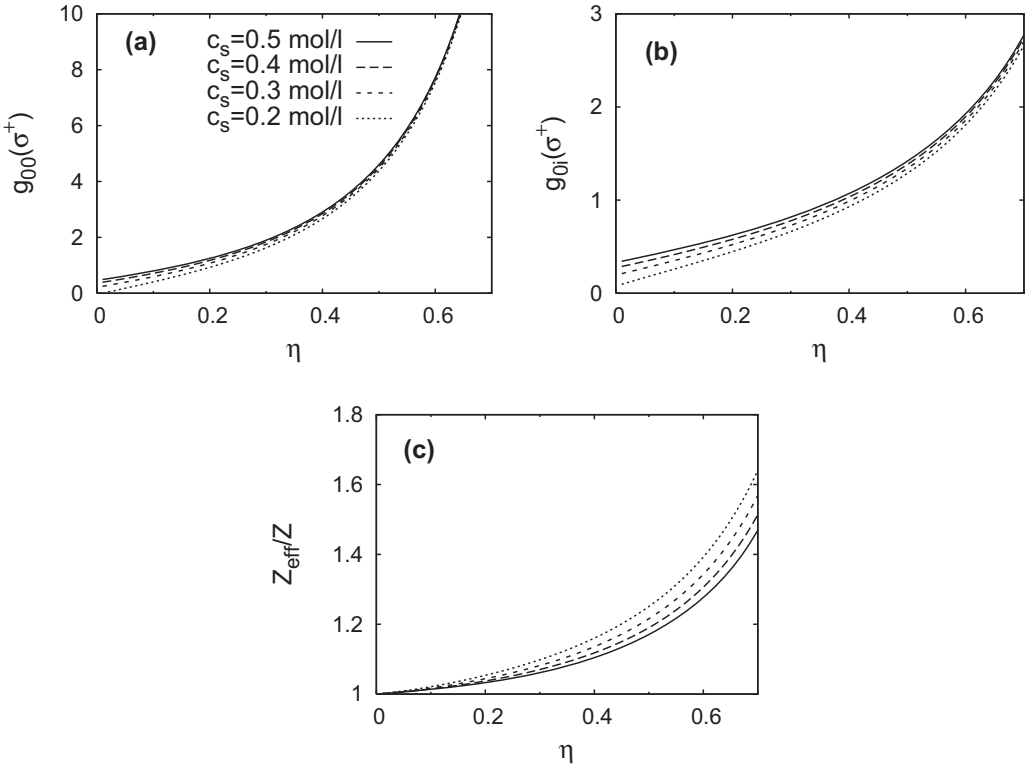

Figure A1: Macroion-macroion radial distribution function contact values, $g_{00}(\sigma^+)$ (chart (a)), and macro-ion-microion contact values, $g_{0\mathrm{i}}(\sigma^+)$ (chart (b)), as a function of the volume fraction, η, as predicted by the linear MSA closure scheme. In chart (c), the ratio between the effective macroion charge number,Z_{eff}, and the number of bare charges, Z, is plotted in dependence of η.

values at the experimental critical point (T_{c},η_{c}), and by selecting two state points from the experimental fluid-solid coexistence region for a fixed temperature. The critical point is known from the experiments, and we use it as one constraint to partially adjust the five unknown interaction parameters in our patchy model. To obtain additional constraints, we focus now on the fluid-solid coexistence curve and select a temperature, T_{fs}, where the fluid of volume fraction η_f is coexisting with a crystalline phase of volume fraction η_s. The fluid branch of the fluid-solid coexistence curve is known experimentally, so that T_{fs} and η_{f} are given. The volume fraction, η_{s}, of the coexisting solid is used as a free parameter, so that no experimental data on the solid branch are invoked. Like in the first method used to determine the interaction parameters, the additional constraint $B_2^*(T_{\mathrm{c}}) = -2.7$ is employed.

In total, this gives a complete set of conditions determining the five unknowns. The fluid-solid phase coexistence implies the constraint of equal pressures and chemical potentials, i.e.,

$$\mu(T_{\rm fs},\eta_f;z_{\rm attr},\epsilon_{\rm attr},\delta,\psi) = \mu(T_{\rm fs},\eta_{\rm s};z_{\rm attr},\epsilon_{\rm attr},\delta,\psi)\,, \tag{B.5}$$

$$\Pi(T_{\rm fs},\eta_{\rm f};z_{\rm attr},\epsilon_{\rm attr},\delta,\psi) = \Pi(T_{\rm fs},\eta_{\rm s};z_{\rm attr},\epsilon_{\rm attr},\delta,\psi)\,, \tag{B.6}$$

and the critical point is characterised by the two additional constraints, namely

$$\frac{\partial^2 f(T_{\rm c},\eta_{\rm c};z_{\rm attr},\epsilon_{\rm attr},\delta,\psi)}{\partial^2\eta} = 0\,, \tag{B.7}$$

and

$$\frac{\partial^3 f(T_{\rm c},\eta_{\rm c};z_{\rm attr},\epsilon_{\rm attr},\delta,\psi)}{\partial^3\eta} = 0\,. \tag{B.8}$$

Taken together with the condition

$$B_2^*(T_{\rm c};\eta_c,z_{\rm attr},\epsilon_{\rm attr},\delta,\psi) = -2.7\,, \tag{B.9}$$

these are five equations for five unknowns. The numerical solution for these equations is

$$\eta_{\rm s} = 0.44\,,\quad z_{\rm attr} = 3.02\,,\quad \epsilon_{\rm attr} = 3.06\,k_{\rm B}T_{\rm c}\,, \tag{B.10}$$
$$\delta = 73.0\,,\quad \chi = 0.707\,,\quad \text{and}\quad \psi = 4.36,$$

for the selected state point ($T_{\rm fs} = 324.1\,{\rm K}, \eta_{\rm f} = 0.16$) on the fluid branch of the fluid-solid coexistence curve. As seen, the parameters $z_{\rm attr}$, $\epsilon_{\rm attr}$, δ, and χ are practically unchanged compared to the previous findings, but ψ is changed slightly from 5 to 4.36. In Fig. B2, the resulting phase diagram (dashed curves) obtained by the present second procedure is compared with the result from the first one used in section 2.4 (solid curves), which was obtained from fixing the calculated binodal to the critical point values of the fluid branch only.

In comparison to the experimental binodal, the calculated gas-liquid coexistence curve obtained for $\psi = 4.36$ is slightly more narrow. Furthermore, the calculated solubility curve is still too steep relative to the experimental data. However, the overall agreement between the calculated solubility curve and the experimental data improves significantly by fixing the distance between the solubility curve and the binodal. Yet, fixing the distance between the two coexistence curves is conceptually less satisfying since it requires information both about the location of the experimental binodal and the solubility curve. The discussion given above suggests that our model is especially accurate for the fluid phase, where the protein molecules re-orient themselves so that an orientational average over the anisotropic shape and the anisotropic pair interactions is more justified. Thus, predicting the solubility curve using experimental information on the fluid phase only is certainly more adequate. Recall again that the crystalline

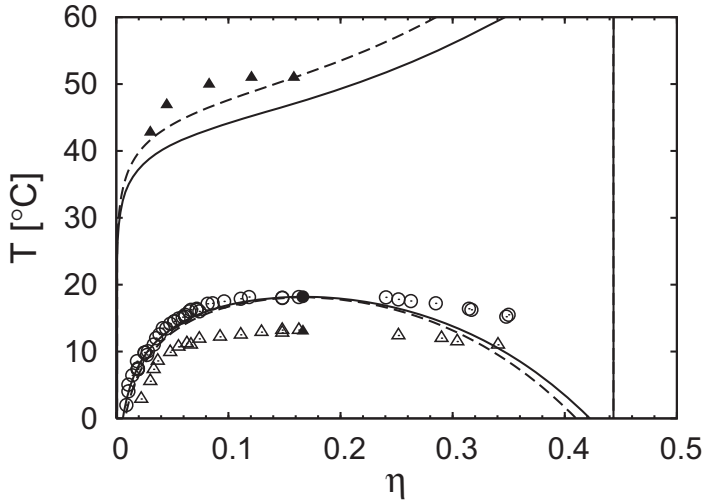

Figure B2: Comparison between theoretically calculated phase diagrams, with $c_s = 0.5\,\mathrm{mol/l}$, and the experimental data by Gibaud [79] and Cardinaux *et al.* [49]. The symbols indicating the experimental data points are identical to those in Figs. 2.8 and 2.10. The experimental data points marked by an triangle (△) describe the binodal for $c_s = 0.4\,\mathrm{mol/l}$. The solid lines are the theoretical gas-liquid and fluid-solid coexistence curves shown already in Fig. 2.8, and obtained using the experimental data for the critical point only. The dashed coexistence curves have been obtained, in contrast, from matching the experimental gap between between an experimental point on the solubility curve and the critical point (see the text for further details).

phase is described in our perturbative approach by a fcc crystal structure even though experiments have shown that lysozyme crystallises depending on the temperature into an tetragonal or orthorhombic lattice structure [94, 95]. Therefore, determining the attractive interaction parameters from the binodal critical point alone avoids to refer additionally to this crude crystal description.

3 Phase behaviour of a dispersion of charge-stabilised colloidal spheres with added non-adsorbing interacting polymer chains

We present a theory for the phase behaviour of mixtures of charge-stabilised colloidal spheres plus interacting polymer chains in good and θ-solvents. The phase diagram is calculated using the free-volume theory. We use simple but accurate combination rules for the depletion thickness around a colloidal particle and for the osmotic pressure up to the semi-dilute concentration regime. In this way, we obtain expressions for the free energy for mixtures of charged colloidal particles and non-adsorbing interacting polymers. From these expression we calculate the phase behaviour, and discuss its topology in dependence on the competition between the charge-induced repulsion and the polymer-induced attraction. The homogeneous mixture of colloids and polymers becomes more stabilised against demixing when he electrostatic repulsion is increased. This charge-induced stabilisation is strongest for small polymer-to-colloid size ratios, and it is more pronounced for charged colloids mixed with polymers in a good solvent than for polymers in a θ-solvent. For the weakly charged regime, we find that the phase diagram becomes salt concentration-independent in the protein regime for charged colloids plus polymers in a θ-solvent. The liquid window, i.e., the concentration ranges where a colloidal liquid exists, is narrowed down upon increasing the charge-induced repulsion. In addition this effect is more pronounced when charged colloids are mixed with polymer chains in a good solvent. In summary, we demonstrate that the solvent quality significantly influences the phase behaviour of mixtures of charged colloids plus non-adsorbing polymers when the range of the screened electrostatic repulsion becomes of the order of the range of the depletion-induced attraction.

3.1 Introduction

Adding non-adsorbing polymers to a dispersion of colloidal particles induces attractive forces between them [6, 96, 97]. These attractive interactions are due to the loss of conformational entropy if a polymer approaches a particle surface, leading to a polymer depleted zone around the particle. Overlapping of two depletion zones induces an inhomogeneous pressure distribution caused by the dissolved polymers around the two neighbouring particles, and, thus, leads to an attractive force between them. This depletion interaction has first been described by Asakura and Oosawa [98, 99] (AO), and was later rediscovered by Vrij [100]. In Vrij's model for mixtures of polymers and colloids, the polymers are freely inter-penetrable (mimicking ideal chains), while there is a hard-sphere repulsion between the colloids and the polymers. This situation corresponds to hard spheres dispersed in a dilute polymer solution.

First success in describing the experimentally observed phase behaviour of colloid-polymer mixtures semi-quantitatively has been made by Gast *et al.* [77] using thermodynamic perturbation theory (TPT). Gas-liquid and fluid-solid phase transitions have been predicted by TPT in accordance with experimental results. Gast *et al.* [77] also showed analytically that the assumption of a pair-wise additive interaction potential in TPT is exact for polymer-to-colloid size ratios $q = R_g/a \leq 2/\sqrt{3} - 1 \approx 0.155$ in case of freely inter-penetrable polymer 'spheres' of radius R_g and the hard-spheres of radius a. For $q > 0.1547$, multiple overlap of depletion zones can occur and many-body interactions have to be taken into account. De Hek and Vrij [101] performed experiments on model hard-sphere-like systems with added non-adsorbing polymer chains using silica particles and polystyrene in cyclohexane. They observed separation into two coexisting fluid phases. The coexistence between a stable fluid and solid was observed for instance by Vincent *et al.* [102, 103].

The partitioning of the polymers over the coexisting colloid-poor and colloid-rich phases has first been described by the free-volume theory (FVT) by Lekkerkerker *et al.* [104]. Here, the main step was to approximate the free-volume accessible to the freely-overlapping polymer coils by using scaled-particle theory (SPT) [105, 106]. Meijer and Frenkel [107] used a lattice model for the mixture of hard spheres and polymers and Monte Carlo (MC) simulation techniques to investigate the accuracy of SPT and TPT. These theories use the AO model, where the deformability of the polymer coil is not taken into account. The simulation data show that polymer-induced many-body interactions have to be taken into account for $q > 0.2$. The theory of Lekkerkerker *et al.* [104] performs overall very well but leads to deviations around the gas-liquid critical point when compared with computer simulation results [108]. Dijkstra *et al.* [76, 109–112] verified and extended the statistical-mechanical derivation of the thermodynamic properties of colloid-polymer mixtures by Meijer and Frenkel [107]. They observed good agreement for equal sizes of the polymers and colloids in comparing their computer

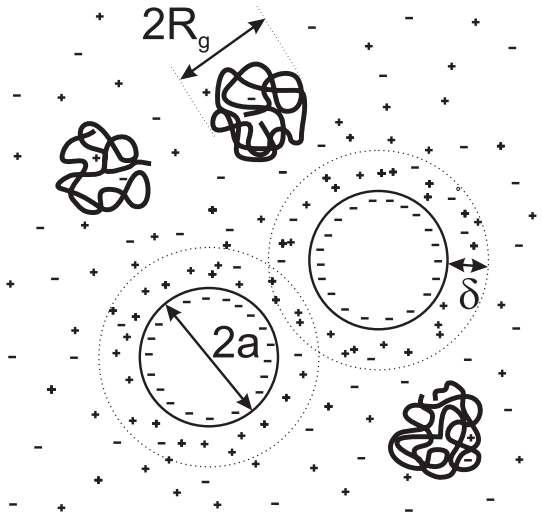

Figure 3.1: Schematic drawing of two negatively charged colloidal particles with diameter $2a$ in a solution with neutral polymers with a radius of gyration R_g. The depletion zone with thickness δ is indicated by the dotted circles around the colloidal particles. The micro-ions are depicted by little plus (+) and minus (−) signs. These micro-ions build up the electrostatic double layer around the charged colloidal particles. Because of the negatively charged macro-ions (colloids), the concentration of counter-ions (+) increases whereas the number of co-ions (−) decreases upon approaching the colloidal surface.

simulation data using the effective one-component AO model with FVT [112]. Moncho-Jorá *et al.* [113] investigated the AO model for $q \gg 1$ (protein limit), where many-body interactions become important. Good agreement was found between the binodals predicted by FVT and the computer simulation data.

Fuchs, Schweizer, and co-workers [114–118] used an off-lattice Polymer Reference Interaction Site Model (PRISM) integral equation method with a modified Percus-Yevick closure to derive analytical expressions for the spinodal boundaries of mixtures of ideal coils and hard spheres. Because calculating the binodal coexistence curves is numerically extremely demanding within PRISM, Zukoski and co-workers [119–121] have restricted themselves to compare theoretically predicted spinodal decomposition curves with binodals in mixtures of effectively hard-sphere-like silica particles and polystyrene polymer chains under θ- (decalin) and good (toluene) solvent conditions. Good agreement has been found which encourages further investigations using this approach. Compared to the free-volume approach yielding macroscopic thermodynamic quantities, the liquid-state theory derived by Fuchs and Schweizer gives quantitative predictions for the microscopic structure of colloid-polymer mixtures which can be verified by appropriate scattering studies. It will be interesting, for instance, to investigate Fuchs and Schweizer's predictions on long-ranged polymer mediated attractive

forces [118], which might be related to recent observations of critical phenomena in colloid-polymer mixtures [122, 123].

The fundamental interest on the influence of the attractive polymer-induced depletion forces on colloidal dispersions, focused especially on studying the global phase behaviour in dependence on the range of attraction through the polymer-to-colloid size ratio. Besides that there is also a need to include properties of non-ideal polymer solutions plus non-hard-sphere colloids to describe industrial colloid-polymer dispersions. Concerning the colloids, a practical situation is to account for electrostatic charges on the colloidal particles that are screened by surface-released counterions. Apart from applications like paints or processed food [124, 125], one encounters such systems for example in biology, and, especially, in the cell, where $20 - 30\%$ of the volume is occupied by soluble proteins and other biomacromolecules [126]. Here, one expects that depletion interactions play a major role in the self-organisation of biomacromolecules, e.g., the self-assembling of DNA [127] or the bundling of f-actin fibres [128]. The aim is therefore to find reasonably simple but accurate expressions to calculate the phase behaviour of charged spheres in a crowded (semi-dilute) (bio-)macromolecular (polymer) environment. An additional need to describe such mixtures of charged colloids and interacting polymers results from crystallography to determine the atomic structure of proteins. Here, polymers are often added to protein solutions at high salt concentration to accelerate crystallisation or to obtain regular crystals [10]. Not many attempts have been made to describe such systems.

Another approach to include the influence of non-ideal polymers has been made by approximating polymers as soft colloids [129–131], and quantitative agreement with computer simulation data on the phase behaviour of colloids and self-avoiding polymers has been found [132] on the level of the depletion interaction between two hard walls. A disadvantage of this approach is that it relies on Monte Carlo simulations as an input to adjust polymer-polymer and colloid-polymer interactions.

Schmidt and Fuchs [133] derived a penetrable Asakura-Ooasawa model (PAO) using density functional theory. The model allows colloids to penetrate the polymer spheres by introducing a repulsive step-function colloid-polymer pair potential. The strength of the colloid-polymer repulsions is adjusted using known expressions from renormalisation group-theory for the insertion energy of adding colloids into a dilute polymer solution at θ- and good solvent conditions. Essentially, the model reduces to the functional AO model with a polymer-to-colloid size ratio-dependent colloid packing fraction neglecting polymer-polymer interactions. The PAO model agrees well with results from the PRISM approach.

The influence of excluded-volume polymer chains on the phase behaviour of colloidal spheres has first been incorporated within the free-volume theory by Aarts *et al.* [134] using results from renormalisation group theory [135, 136] for the correlation length in polymer solutions.

The phase equilibrium of charged colloidal particles with polymer-induced de-

pletion interaction has been investigated by Tavares and Sandler [137] using TPT and Gibbs ensemble Monte Carlo simulations. In this work the electrostatic repulsion was modelled on a Debye-Hückel level and van der Waals interactions were included as well. They observed that the additional van der Waals attraction widens the fluid-solid coexistence curves and destabilises the dispersion against gas-liquid phase separation. On the other hand, the repulsive electrostatic forces tremendously stabilise the colloid-polymer mixture against phase separation. Thus, the fluid-solid coexistence curve shifts to higher polymer concentrations upon increasing the screened electrostatic repulsions.

Later on, Ferreira *et al.* [138] have calculated spinodal decomposition curves using liquid-state theory for charged colloids and neutral polymers inter alia. They also observed that the electrostatic repulsion between highly charges colloids [84] significantly stabilises mixtures of charged colloids and non-adsorbing polymers against gas-liquid phase separation (see Fig. 11 and the discussion on p. 9860 in [138]).

Denton and Schmidt [139] included electrostatic repulsive forces due to screened charges into the free-volume theory. In their model, the electrostatic repulsions were mapped onto effective hard-sphere interactions, and the additivity of the mixture was restored by scaling the radius of gyration of the polymer. Fortini *et al.* [140] proposed a similar way to include highly screened electrostatic Coulomb interactions to the free-volume theory by mapping the repulsive interactions onto effective hard-sphere ones. In their approach, the non-additivity of the mixture was not restored by (down-)scaling the polymer size. Instead, the free-volume fraction was reanalysed from SPT, and a semi-quantitatively accurate description was proposed, which describes their computer simulation data reasonably well. In contrast, the model by Denton and Schmidt underestimates the osmotic pressure of the polymer solution significantly. Thus, it follows that rescaling the polymers and ensuring an additive mixture is inappropriate in describing highly screened or, conversely, weakly charged colloidal dispersions containing non-adsorbing polymers.

Fleer and Tuinier [141] extended the free-volume approach for colloid-polymer mixtures up to and including the semi-dilute concentration regime for interacting polymer solutions, using scaling arguments for the depletion thickness and osmotic pressure. Their expressions for the depletion thickness and osmotic pressure were tested against experimental and computer simulation data [142]. Quite recently, Tuinier *et al.* [143] have compared this approach to experimental data on the gas-liquid phase coexistence diagram of hard-sphere-like polymethylmethacrylate colloids with added flexible polystyrene chains dispersed in cis-decalin and found excellent quantitative agreement. This improved free-volume theory has been named generalised free-volume theory (GFVT). Based on this adequate refinement, we feel encouraged to apply the GFVT to mixtures of charged colloids and interacting polymer solutions.

In this work, we present a generalised free-volume theory which predicts the

equilibrium phase behaviour of mixtures of polymers and charged colloidal spheres in either a θ- or good solvent. We calculate the fluid-solid and gas-liquid coexistence curves for various size ratios of the polymers and the colloids, and for various electrostatic screening lengths. Here, we restrict ourselves to the regime of weakly charged or, equivalently, highly screened particles with thin double layers, where the electrostatic pair interactions can be mapped accurately onto an effective hard-sphere interaction. We also discuss the influence of the solvent quality and the effect of the electrostatic repulsion, on the stability of a homogeneous fluid phase with respect to a gas-liquid phase demixing, and we further focus on the effect of salinity on the location of the critical end point.

3.2 Model of weakly charged colloidal particles and non-adsorbing polymer chains

We now proceed to explain how we map the system of charged colloids onto an effective hard-sphere system. In section 3.3, the polymers, which in addition insert depletion-induced attractive interactions to the system, are taken into account. As an application for our model calculations one might think of weakly charged globular proteins at high salt content, dispersed in a polymer solution to accelerate crystallisation. Thus, we assume that the electrostatic Coulomb interactions are highly screened, and, therefore, short-ranged. We also assume that correlation effects between the micro-ions (added salt and surface released counter-ions), which might arise due to the comparable size between the micro-ions and macro-ions (proteins), can be neglected. This assumption even may hold for high salt concentrations in case of monovalent co- and counter-ions. We describe the electrostatic repulsion by a Debye-Hückel screened Yukawa-like pair interaction potential,

$$\beta u_{\mathrm{cc}}(r) = \begin{cases} \infty\,, & r \leq 2a \\ \dfrac{Z^2\, l_{\mathrm{B}}}{(1+\kappa a)^2}\, \dfrac{\exp\left[-\kappa(r-2a)\right]}{r}\,, & r > 2a\,, \end{cases} \tag{3.1}$$

where Z is the protein charge number and $l_{\mathrm{B}} = e^2/\left(4\pi\,\varepsilon_0\,\varepsilon\,k_{\mathrm{B}}T\right)$ is the Bjerrum length with the dielectric constant in vacuo, ε_0, the dielectric solvent constant, ε, and the elementary charge e. The colloidal particle radius is denoted by a. The square of the Debye screening parameter, κ, is given as

$$\kappa^2 = 4\pi l_{\mathrm{B}} \left(|Z|\rho_{\mathrm{c}} + \sum_s \rho_{\mathrm{s}} \right)\,, \tag{3.2}$$

where ρ_{c} is the colloid number density. The first term between the brackets accounts for monovalent counter-ions released from the colloid surface, and the second for the additionally inserted monovalent micro-ions with number density

ρ_s. For later use we introduce the reduced contact value of the repulsive pair interaction potential as $\beta\epsilon = 2\,Z^2\,l_B\,a/(1+\kappa a)^2$.

As discussed previously by Fortini *et al.* [140], one can map electrostatic repulsions onto effective hard-sphere interactions provided the colloidal net charges are sufficiently screened by the co- and counter-ions, or provided that the colloidal particles are sufficiently weakly charged. The resulting effective volume fraction, η_c', is defined by

$$\eta_c' = \left(\frac{a'}{a}\right)^3 \eta_c = m\,\eta_c\,, \tag{3.3}$$

where a' is the effective colloidal radius, and $\eta_c = 4\pi a^3\rho_c/3$ denotes the colloid volume fraction. The factor m is defined as the cubed size-ratio between the effective, a', and bare colloidal particle radius, a. The effective radius, a', of a charged colloidal sphere is calculated using the expression found by Barker and Henderson [60] from leading-order TPT

$$a' = a + \frac{1}{2}\int_{2a}^{\infty} dr\,(1 - \exp[-\beta u_{cc}(r)])\,. \tag{3.4}$$

Next, after we have mapped the charge-induced colloid-colloid interactions onto effective hard-sphere-like interactions, the effect of the non-adsorbing polymer chains on the colloidal dispersion can be treated within the framework of the free-volume theory.

3.3 Generalised free-volume theory

3.3.1 Semi-grand canonical potential

To compute the equilibrium phase diagram of mixtures of charged colloids and polymers, we need expressions for the free energy of the colloidal fluid and solid phases. Due to the fact that we have already mapped the screened electrostatic Coulomb interactions onto hard-sphere ones, we can apply a simple approach that successfully describes the stability of polymer-colloid mixtures [104, 144]. Here, the colloid-polymer mixture is described in the semi-grand-canonical ensemble, where N_c colloidal particles (c) and N_p polymer chains are enclosed in the system with volume V at temperature T. The system is attached to a reservoir (r) of polymer chains (p), which is in osmotic equilibrium with the polymer solution in the system. Thus, the system is described by the (N_c, V, T, μ_p^r) ensemble, where μ_p^r is the chemical potential of the polymer chains in the reservoir. This potential μ_p^r determines the polymer number density, $\rho_r = N_p/V$, in the system. The semi-grand canonical potential is characterised through

$$\Omega(N_\mathrm{c}, V, T, \mu_\mathrm{p}^\mathrm{r}) = F(N_\mathrm{c}, V, T) - \int_{-\infty}^{\mu_\mathrm{p}^\mathrm{r}} \left\langle N_\mathrm{p}(\tilde{\mu}_\mathrm{p}^\mathrm{r}) \right\rangle \, d\tilde{\mu}_\mathrm{p}^\mathrm{r} \,. \tag{3.5}$$

The (canonical) free energy of the charged colloid dispersion in the absence of polymers is described by $F(N_\mathrm{c}, V, T)$; i.e., $\Omega(\ N_\mathrm{c},\ V,\ T,\ \mu_\mathrm{p}^\mathrm{r} \to -\infty) = F(N_\mathrm{c},\ V,\ T)$. The brackets, $\langle\cdot\rangle$, underneath the integral denote the semi-grand-canonical ensemble average, and the tilde indicates the integration variable.

We define the free-volume fraction as $\alpha(\rho_\mathrm{c},\, \mu_\mathrm{p}^\mathrm{r}) = \langle V_\mathrm{free} \rangle / V = \rho_\mathrm{p}/\rho_\mathrm{p}^\mathrm{r}$, where V_free is the free-volume in the system not occupied by the colloids and their depletion zones and $\rho_\mathrm{p}^\mathrm{r}$ is the reservoir polymer number density. Using the Gibbs-Duhem relation, $\rho_\mathrm{p}^\mathrm{r}\, d\mu_\mathrm{p}^\mathrm{r} = d\Pi_p^\mathrm{r} = (\partial \Pi_p^\mathrm{r} /\ \partial \rho_\mathrm{p}^\mathrm{r})\ \ d\rho_\mathrm{p}^\mathrm{r}$, where $\Pi_\mathrm{p}^\mathrm{r}$ is the reservoir polymer osmotic pressure, we obtain

$$\omega(\eta_\mathrm{c}, y) = f(\eta_\mathrm{c}) - \int_0^y \alpha(\eta_\mathrm{c}, \mu_\mathrm{p}^\mathrm{r}(\tilde{y})) \, \frac{\partial \hat{\Pi}_\mathrm{p}^\mathrm{r}(\eta_\mathrm{c}, \mu_\mathrm{p}^\mathrm{r}(\tilde{y}))}{\partial \tilde{y}} \, d\tilde{y} \,. \tag{3.6}$$

Here, we introduced the reduced semi-grand-canonical free energy density $\omega = \beta \Omega v_0 / V$ and the reduced canonical free energy density $f = \beta F v_0 / V$, where $1/\beta = k_\mathrm{B} T$ is the thermal energy and $v_0 = 4\pi a^3/3$ is the colloid volume. The relative reservoir polymer concentration is given by $y = \rho_\mathrm{p}^\mathrm{r} (4/3) \pi R_\mathrm{g}^3$, where R_g is the radius of gyration of a polymer coil. We also use the normalised osmotic pressure defined as $\hat{\Pi}_\mathrm{p}^\mathrm{r} = \beta \, \Pi_\mathrm{p}^\mathrm{r}(\eta_\mathrm{c}, \mu_\mathrm{p}(y))\, v_0$.

So far no approximation has been made. The contribution of the polymers to the free energy in the second term is now described by the (reservoir) polymer osmotic pressure, $\hat{\Pi}_\mathrm{p}^\mathrm{r}(\eta_\mathrm{c}, y)$, and the free-volume fraction, $\alpha(\eta_\mathrm{c}, y)$, accessible to the polymer chains.

We approximate $\alpha(\eta_\mathrm{c}, y)$ by an expression previously derived by Fortini *et al.* [140],

$$\alpha(\eta_\mathrm{c}, y) = (1 - \eta_\mathrm{c}) \exp(-b_1 \gamma - b_2 \gamma^2 - b_3 \zeta - 3 b_3 \zeta^2 - 3 b_3 \zeta^3) \,, \tag{3.7}$$

where $\gamma = \eta_\mathrm{c}/(1 - \eta_\mathrm{c})$, $\zeta = \eta_\mathrm{c}'/(1 - \eta_\mathrm{c}')$, $b_1 = 3q_\mathrm{s} + 3q_\mathrm{s}^2$, $b_2 = 9q_\mathrm{s}^2/2$, and $b_3 = q_\mathrm{s}^3$. The size ratio $q_\mathrm{s} = \delta/a$ is the ratio of the depletion thickness δ around a spherical particle over a. For uncharged colloids, or infinite screening ($m \to 1$), the free-volume factor reduces to the hard-sphere one known from SPT [105, 106]. A geometric interpretation of these factors in terms of fundamental measure theory has been given by Oversteegen and Roth [145]. The relative polymer concentration within the system, η_p, is given by $\eta_\mathrm{p} = \alpha(\eta_\mathrm{c}, y)\, y$.

We note that SPT is approximate, but surprisingly, the free-volume fraction from SPT appears to be rather accurate [112]. Brader *et al.* [146] have discussed possible ways to derive systematic expressions for the free-volume fraction by first calculating the equilibrium properties of the effective one-component system where the polymer degrees of freedom has been integrated out. This could be done either theoretically or by using using Monte Carlo computer simulations

results. The polymer concentration and, thus, the free-volume fraction $\alpha(\eta_c, y)$ could then be obtained exactly using pair and higher order distribution functions. An effective pair potential for mixtures of interacting (excluded volume) polymer chains and colloids has been derived from computer simulations by Louis *et al.* [147], which might be used in such an approach. Thus, it is possible to test the extensively used SPT against exact computer simulations. There is a need for more work in this direction to reveal how accurate SPT is for more complicated systems. The physical properties of the polymer solution will be discussed separately for ideal and interacting polymer in subsections 3.3.2, 3.3.3 and 3.3.4.

The canonical free energy of the effective hard-sphere system consists in the fluid phase of the ideal gas term,

$$m\, f^{\mathrm{id}}(\eta_c) = \eta_c' \left[\ln(\eta_c' \Lambda_c^3 / v_0) - 1\right] , \tag{3.8}$$

where $\Lambda_c = h/\sqrt{2\pi m_c k_B T}$ is the thermal wavelength, with the colloid mass m_c, Planck's constant h, and the hard-sphere interaction term, which we describe by the Carnahan-Starling equation of state [61],

$$m f^{\mathrm{CS}}(\eta_c) = \frac{4\eta_c'^2 - 3\eta_c'^3}{(1-\eta_c')^2} . \tag{3.9}$$

Here the factor m appears because we have normalised the free energy by the bare colloid volume v_0 (see above).

The solid phase is assumed to have a face-centred cubic (fcc) lattice structure. We use Wood's equation of state [67] to describe the free energy of the effective hard-sphere system [140],

$$m f^{\mathrm{Wood}}(\eta_c) = 2.1306\,\eta_c' + 3\,\eta_c' \ln\left(\frac{\eta_c'}{1-\eta_c'/\eta_c^{\mathrm{cp}}}\right) + \eta_c' \ln\left(\frac{\Lambda_c^3}{v_0}\right) . \tag{3.10}$$

where $\eta_c^{\mathrm{cp}} = \pi\sqrt{2}/6$ is the fcc volume fraction for close packing. The integration constant (inside the first term on the right-hand side) is obtained from the absolute free energy of a hard-sphere crystal calculated from Monte Carlo simulations at $\eta_c = 0.576$ [68].

When fluid and solid phase coexist, the two phases are in thermal, mechanical, and chemical equilibrium. Thus, for a given polymer reservoir concentration, y, thermodynamic equilibrium is reached when the osmotic pressures

$$\hat{\Pi}_f(\eta_{c,f}, y) = \hat{\Pi}_s(\eta_{c,s}, y) \tag{3.11}$$

and the chemical potentials,

$$\mu_f(\eta_{c,f}, y) = \mu_s(\eta_{c,s}, y) \tag{3.12}$$

of the fluid (f) and solid (s) phases are equal at the two different volume fractions, $\eta_{\mathrm{c,f}}$ and $\eta_{\mathrm{c,s}}$, respectively, where

$$\hat{\Pi}(\eta_{\mathrm{c}}, y) = \eta_{\mathrm{c}}^2 \frac{\partial(\omega(\eta_{\mathrm{c}}, y)/\eta_{\mathrm{c}})}{\partial \eta_{\mathrm{c}}} \tag{3.13}$$

and

$$\beta\mu(\eta_{\mathrm{c}}, y) = \frac{\partial \omega(\eta_{\mathrm{c}}, y)}{\partial \eta_{\mathrm{c}}} \,. \tag{3.14}$$

A gas-like phase at low colloidal density coexists with a liquid-like phase at high colloidal density for equal osmotic pressures

$$\hat{\Pi}_{\mathrm{g}}(\eta_{\mathrm{c,g}}, y) = \hat{\Pi}_{\mathrm{l}}(\eta_{\mathrm{c,l}}, y) \,, \tag{3.15}$$

and chemical potentials,

$$\mu_{\mathrm{g}}(\eta_{\mathrm{c,g}}, y) = \mu_{\mathrm{l}}(\eta_{\mathrm{c,l}}, y) \,. \tag{3.16}$$

The spinodal curve is found where the thermodynamic compressibility diverges at infinite wavelengths, i.e., where

$$\frac{\partial^2 \omega(\eta_{\mathrm{c}}, y)}{\partial \eta_{\mathrm{c}}^2} = 0 \,. \tag{3.17}$$

The binodal and spinodal terminate and merge at the critical point,

$$\frac{\partial^2 \omega(\eta_{\mathrm{c}}, y)}{\partial^2 \eta_{\mathrm{c}}} = 0 \quad \text{and} \quad \frac{\partial^3 \omega(\eta_{\mathrm{c}}, y)}{\partial^3 \eta_{\mathrm{c}}} = 0 \,. \tag{3.18}$$

The critical end point marks the lowest polymer-to-colloid size ratio where a colloidal liquid is stable, and is found where the gas-liquid critical point coexists with the solid phase [148].

3.3.2 Dilute and semi-dilute polymer solutions

So far undetermined are the osmotic pressure, $\hat{\Pi}_{\mathrm{p}}^{\mathrm{r}}$, of the polymers in Eq. (3.6), and the depletion thickness δ, which enters the free-volume fraction $\alpha(\eta_{\mathrm{c}}, y)$, Eq. (3.7), through the size ratio $q_{\mathrm{s}} = \delta/a$. For small polymer-to-colloid size ratios, when $q \lesssim 0.4$, the relevant part of the phase diagram lies below the polymer overlap concentration ($y < 1$). Then interactions between the polymers are not essential to properly describe the phase diagram and it is still sufficient to approximate the polymer-induced osmotic pressure by the ideal gas law as assumed in the seminal work by Lekkerkerker *et al.* [104]. Furthermore, the depletion thickness takes a value close to R_{g} in dilute polymer solutions. In dilute polymer solutions, the depletion thickness near a flat plate, δ_0, is given by [136, 149],

$$\delta_0 = p\, R_{\rm g} \quad \text{, with} \quad p = \begin{cases} 2/\sqrt{\pi} & \text{in a } \theta\text{-solvent, and} \\ 2x/\sqrt{\pi} & \text{in a good solvent,} \end{cases}$$

where $x = 3/4 + 3\ln(2)/8 + \pi/8 - \pi/\sqrt{48} = 0.9492$. When the polymers have a similar or larger size with respect to the colloidal particles, $q \gtrsim 1$, the polymer concentrations where phase transitions occur, are of the order of and above the polymer overlap concentration (compare, e.g. Fig. 4 b and c in [134]). Thus, for $q \gtrsim 0.4$ interactions between the polymer segments should be accounted for. In the semi-dilute concentration regime, the depletion thickness becomes the concentration-dependent correlation length $\xi \sim y^{-\tau}$, with $\tau = 1$ for θ-solvents and $\tau = 0.77$ for good solvents [150]. To incorporate the crossover from dilute to the semi-dilute polymer concentrations, Fleer *et al.* [142] have derived phenomenological expressions for the polymer concentration-dependent depletion thickness and the polymer induced osmotic pressure by interpolating between the exactly known dilute limit and scaling relations valid for semi-dilute polymer concentrations using combination rules.

For the osmotic pressure they found [142]

$$\hat{\Pi}^{\rm r}_{\rm p}(q,y) = q^{-3}\left(y + A\, y^{3\tau}\right) . \tag{3.19}$$

The de Gennes scaling exponent τ and the parameter A depend on the solvent quality and will be specified in subsections C and D. In the dilute limit, $y \ll 1$, Eq. (3.19) reduces to the osmotic pressure of an ideal polymer solution, $\hat{\Pi}^{\rm r}_{\rm p} = q^{-3}y$, and in the semi-dilute regime it recovers the scaling relation $\hat{\Pi}^{\rm r}_{\rm p} \sim \xi^{-3} \sim q^{-3}y^{3\tau}$ [150].

The depletion thickness for dilute and semi-dilute polymer solutions next to a flat plate, $\delta_{\rm p}$, was obtained previously [141, 142, 151] as,

$$\delta_{\rm p}/\delta_0 = \left(1 + By^{2\tau}\right)^{-1/2} , \tag{3.20}$$

where B is a parameter which again depends on the solvent quality. In the dilute limit ($y \to 0$), $\delta_{\rm p}$ reduces to δ_0, and in the semi-dilute limit it recovers the scaling relation $\delta_{\rm p} \sim y^{-\gamma}$ [150].

We also have to account for curvature effects to find an accurate description for the depletion thickness, δ, around the spherical colloidal particles. For ideal polymer chains, Louis *et al.* [152] and Aarts *et al.* [134] derived the relation between δ as a function of the depletion thickness at a flat plate in *dilute* polymer solutions, δ_0, using the density profile around a sphere [135, 153],

$$q_{\rm s}^{\rm (mf)}(q_0) = \left(1 + 3\, q_0 + \frac{3\pi}{4}\, q_0^2\right)^{1/3} - 1 , \tag{3.21}$$

where $q_0 = \delta_0/a$ and $q_{\rm s} = \delta/a$. This result is valid for dilute polymers in

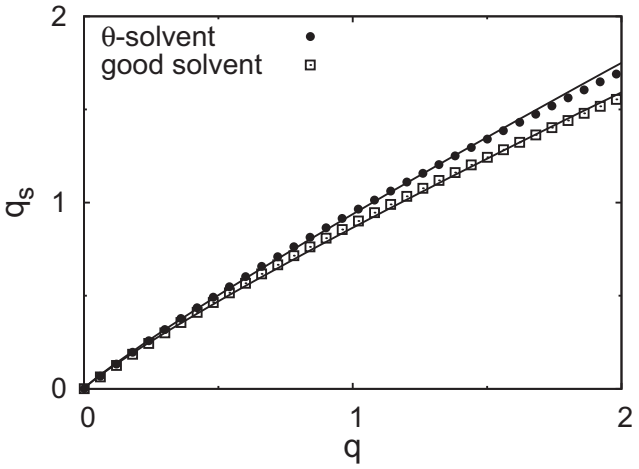

Figure 3.2: Normalised depletion thickness around a sphere, $q_s = \delta/a$, as a function of the reduced radius of gyration, $q = R_g/a$. The dots correspond to polymer chains in a θ-solvent (Eq. (3.21)) and the squares describe interacting polymer chains in good solvent (Eq. (3.22)). The solid curves indicate the power-law fits (Eq. (3.23) and (3.24), respectively) to the analytical expressions for polymer chains in a θ-solvent (Eq. (3.21)) and in a good solvent (Eq. (3.22)), respectively.

a θ-solvent. Hanke *et al.* [136] have derived an equivalent relation for polymer chains in the excluded volume limit (i.e., for polymer chains with excluded-volume monomer-monomer interactions (ev)),

$$q_s^{(ev)}(q_0) = \left(1 + 3q_0 + 3c_2 q_0^2 - 3c_3 q_0^3 + \ldots\right)^{1/3} - 1\,, \tag{3.22}$$

where $c_2 = \pi(1 - 5\pi/8 + 17/36 + \pi\sqrt{3}/4)/(4\,x^2) = 0.7576$ and $c_3 = \pi(1673\pi/48 - 551/15 - 40\sqrt{3}/\pi)/(24x^3) = 0.0325$. In Fig. 3.2, we plot q_s as a function of q, where $q = q_0/p$ according to Eq. (3.19). The lower curve corresponds to polymers in a good solvent (Eq. (3.22)) and the upper curve is the result for a θ-solvent (Eq. (3.21)). As proposed by Fleer and Tuinier [141,154], q_s can be approximated by simpler power laws, namely

$$q_s^{(mf)}(q_0) = 0.842\, q_0^{0.9}\,, \tag{3.23}$$

and

$$q_s^{(ev)}(q_0) = 0.814\, q_0^{0.88}\,. \tag{3.24}$$

These are indicated in Fig. 3.2 by dots (mean-field chains) and squares (excluded-volume chains). As expected, the depletion thickness around a sphere is smaller compared to the depletion thickness close to a flat plate. Furthermore, the depletion thickness due to polymer chains in a good solvent (excluded-volume chains) is smaller as compared to polymers in a θ-solvent. The deviations become more pronounced with increasing q. The $q > 2$ regime is, however, less relevant as

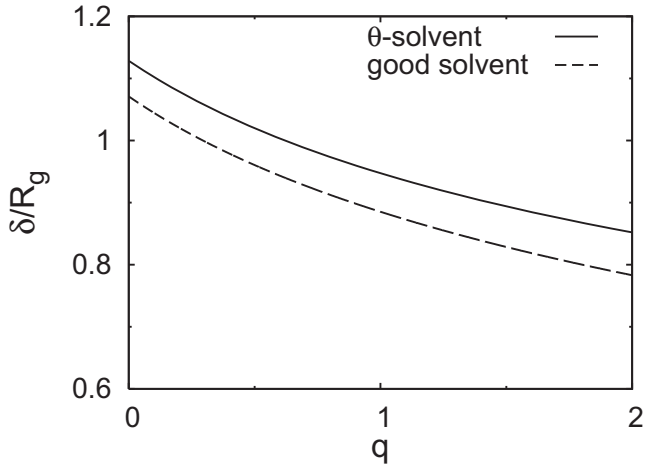

Figure 3.3: Influence of the polymer-to-colloid size ratio $q = R_g/a$ on the depletion thickness around a sphere in units of the radius of gyration, δ/R_g. The solid curve describes the size ratio dependence of δ/R_g for polymer chains in a θ-solvent and the dashed one the influence of the curvature for good solvent conditions.

we shall see. In addition, we show the influence of q on the depletion thickness around a sphere, δ, relative to the radius of gyration R_g for good and θ-solvent conditions in Fig. 3.3. As can be seen clearly, δ/R_g decreases with increasing q and is well below one if q exceeds one.

3.3.3 Polymer solutions in a θ-solvent (mean-field approximation)

For polymer chains in a θ-solvent, the scaling exponent τ becomes equal to its mean-field value $\tau = 1$. The parameters that follow from the combination rules that link the semi-dilute regime of the osmotic pressure and the depletion thickness towards zero polymer volume fraction are $A = 4.1$ and $B = 5.94$ [142], respectively. The polymer concentration derivative of the reduced osmotic pressure is

$$\frac{\partial \hat{\Pi}_p^r(q,y)}{\partial y} = q^{-3}\left[1 + 12.3\, y^2\right] , \tag{3.25}$$

and the depletion thickness-to-colloid radius size ratio is

$$q_s(q,y) = 0.938\left(q/\sqrt{1 + 5.94\, y^2}\right)^{0.9} . \tag{3.26}$$

Eq. (3.26) follows directly by replacing q_0 with the reduced depletion thickness for dilute *and* semi-dilute polymer solution, δ_p/a, introduced in Eq. (3.20), and using Eq. (3.19).

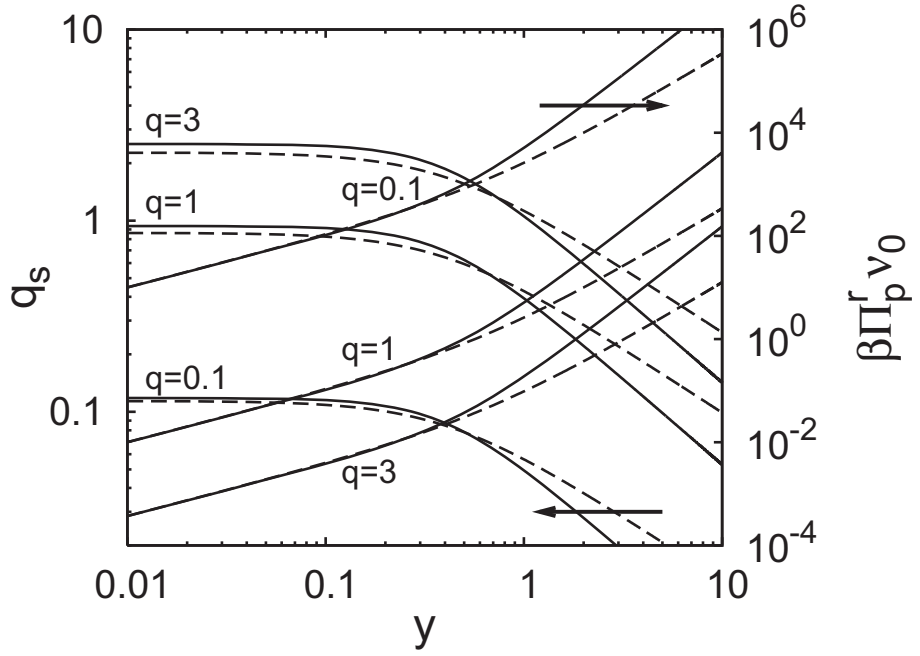

Figure 3.4: Influence of the polymer concentration y on the relative depletion thickness around a sphere, $q_s = \delta/a$, and on the reduced polymer osmotic pressure $\hat{\Pi}_p = \beta\,\Pi_p^r\,\nu_0$. The solid curves describe the influence of y on q_s and $\hat{\Pi}_p$, respectively, for polymer chains in θ-solvent and the dashed curves for polymers in good solvent.

3.3.4 Interacting polymer solutions in good solvent

In a semi-dilute polymer solution, the de Gennes scaling exponent τ equals 0.77 under good solvent conditions. The parameters A and B now read $A = 1.615$ and $B = 3.95$ [142]. Therefore,we have

$$\frac{\partial\hat{\Pi}_p^r(q,y)}{\partial y} = q^{-3}\left[1 + 3.73\,y^{1.31}\right], \tag{3.27}$$

and

$$q_s(q,y) = 0.865\left(q/\sqrt{1 + 3.95\,y^{1.54}}\right)^{0.88}. \tag{3.28}$$

Note that in contrast to the classical FVT [104], $\partial\hat{\Pi}_p^r/\partial y$ and q_s in Eqs. (3.25)-(3.28) now depend on the polymer concentration y.

In Fig. 3.4, the effective size-ratio q_s is given as a function of the polymer concentration y for $q = 0.1$, 1 and 3. The solid curves describe polymer chains in θ-solvent and the dashed curves polymers under good solvent conditions. The effective size-ratio, $q_s = \delta/a$, is nearly independent of y at small polymer concentrations ($y \lesssim 0.1$) and decreases rapidly with increasing y. It follows that

the effective size-ratio is smaller for polymer chains in a good solvent as compared to chains in a θ-solvent for low polymer concentrations, but decreases less rapidly with increasing y so that for high concentrations the effective size-ratio in a good solvent is larger than q_s in a θ-solvent. Also shown in Fig. 3.4 is the reduced polymer-induced osmotic pressure $\beta\Pi_p^r v_0$, which describes the osmotic work to insert a particle without depletion layer. As expected, the work required for inserting a colloidal particle increases with increasing polymer concentration. However, $\beta\Pi_p^r v_0$ increases more rapidly for polymer chains in a θ-solvent as for chains in good solvent. We note that the polymer concentration is normalised with the overlap concentration. The overlap concentration for polymer chains in a good solvent is significantly smaller as for θ-chains due to chain swelling.

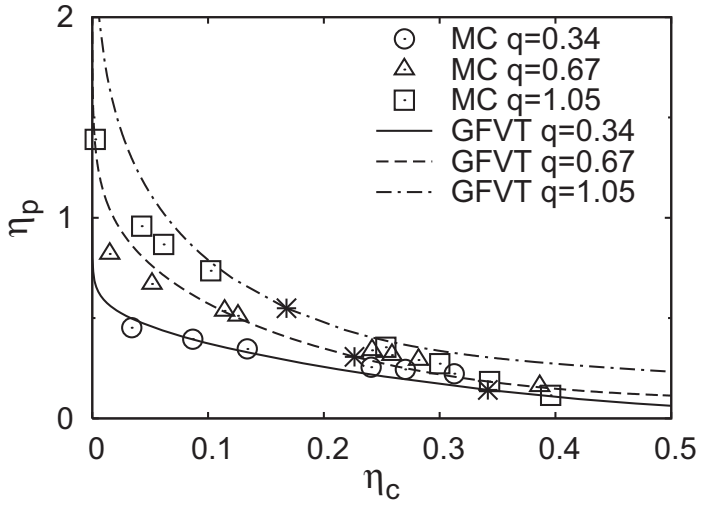

Figure 3.5: Gas-liquid coexistence curves for size-ratios q as indicated in the colloid limit ($q \lesssim 1$) and for equal size for mixtures of interacting polymer in a good solvent plus hard-sphere colloids. The open symbols are results from computer simulations by Bolhuis *et al.* [155] using a Gaussian core model for the polymer chains. The curves are calculated gas-liquid binodals using generalised free-volume theory. The asterisks indicate the theoretical critical point.

3.4 Results and discussion

3.4.1 Phase behaviour of uncharged colloid-polymer mixtures: comparison with simulation results

We first compare the generalised free-volume theory with computer simulation data by Bolhuis *et al.* [132,155] on uncharged colloid-polymer mixtures. In [132], these authors computed the gas-liquid phase coexistence curves for mixtures of hard spheres plus a polymer solution of interacting chains modelled as Gaussian cores with $q = 0.34$, 0.67 and 1.05. Thus, the colloid regime ($q < 1$) and a colloid-polymer mixture with equal size were explored. Gas-liquid binodals in the protein regime ($q > 1$) were computed for hard spheres plus excluded volume chains on a discrete lattice using Monte Carlo (MC) techniques for $q = 3.86$, 5.58 and 7.78. In Fig. 3.5, the simulation data for size ratios $q = 0.34$, $q = 0.67$ and $q = 1.05$ are compared with the gas-liquid coexistence curves predicted from generalised free-volume theory (GFVT). The theoretically predicted gas-liquid coexistence curve agrees well for $q = 0.34$ with the computer simulation data. With increasing size ratio (i.e., at $q = 0.67$ and $q = 1.05$) the binodals predicted from GFVT start to deviate slightly from the simulation data. In fact, the polymer concentration at which phase separation first occurs is slightly overestimated by GFVT.

This deviation increases with increasing colloid volume fraction. In Fig. 3.6, the

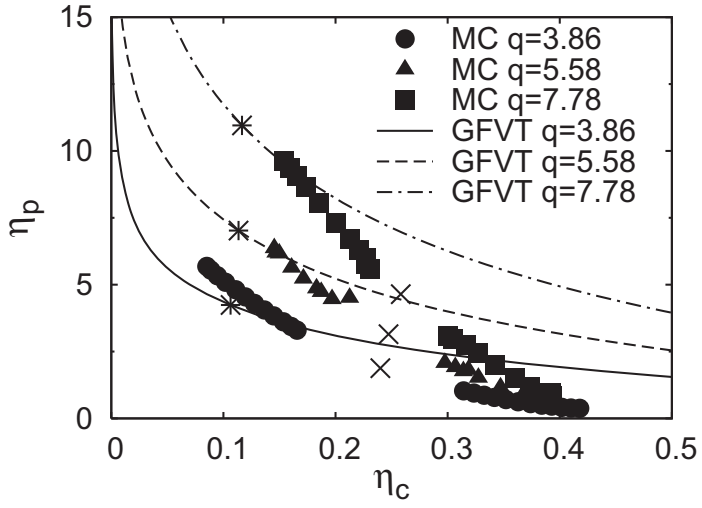

Figure 3.6: Gas-liquid coexistence curves at different size-ratios q in the protein limit ($q > 1$) for hard spheres and interacting polymer chains in a good solvent. The coexistence curves are calculated from generalised free-volume theory. The asterisks are the critical points calculated from theory. The solid binodal data points are taken from Bolhuis *et al.* [155], and the crosses indicate critical points extracted from these computer simulation data.

calculated gas-liquid phase coexistence curves from GFVT are plotted together with MC data in the protein limit ($q = 3.86$, $q = 5.58$ and $q = 7.78$), and larger deviations are found. At low η_c the binodals are underestimated by GFVT (i.e., phase separation is predicted at too low polymer volume fractions), whereas the stability region of the homogeneous colloid-polymer mixture is significantly overestimated at high η_c. The colloidal volume fraction at the critical point is underestimated and the critical polymer volume fraction is overestimated by the GFVT by a factor of two. Thus, we conclude that the GFVT describes colloid-polymer mixtures in the colloid limit reasonably well, but is less adequate to quantitatively predict the MC simulation results of the phase coexistence curves in the protein limit. This limited accuracy of GFVT for size ratios of $q \geq 1$ could be due to the fact that the polymers are treated within the SPT as a small perturbation to the hard-sphere colloidal reference system. In fact, one assumes that the configurations of the colloids do not change if a small polymer chain is inserted. Obviously, this assumption holds only if the polymer coil is small compared to the colloid size. We note that computer simulations are of course not exact in the sense that that they approximate real systems. PRISM gives critical colloid volume fractions in the protein limit that are quite close to GFVT predictions [154]. Besides some quantitative mismatch, it has been shown by Fleer and Tuinier [141] that GFVT predicts the q-scaling behaviour quite accrately [155]. In addition, the critical colloid volume fraction observed within

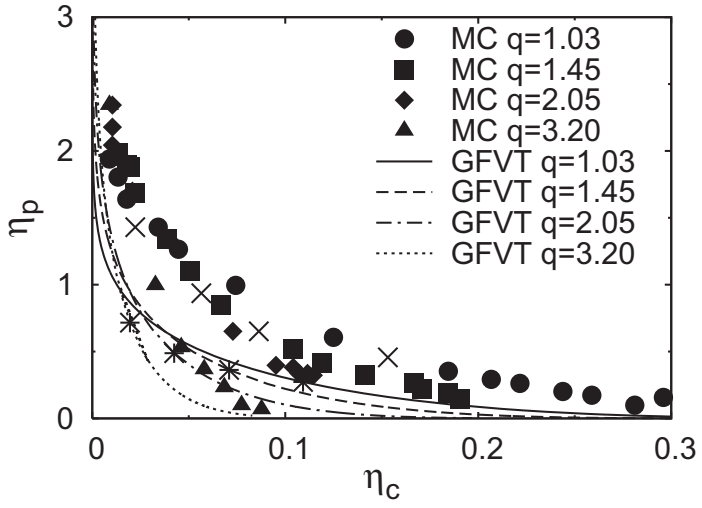

Figure 3.7: Gas-liquid coexistence curves at different size-ratios q for ideal, non-interacting polymer chains. The coexistence curves are calculated from generalised free-volume theory. The asterisks mark the GFVT critical points. The solid data binodal points are taken from Bolhuis *et al.* [155], with the crosses indicating the extracted critical points from these MC computer simulation data.

GFVT is nearly constant as found also in MC simulation and PRISM. The theory and computer simulations show that the critical polymer concentration increases with increasing q.

In Fig. 3.7, we compare binodals for mixtures of ideal (non-interacting) polymers and colloids from MC [155] and GFVT. The expressions for ideal polymers are obtained from Eq. (3.25) and Eq. (3.26) for $y \to 0$. In contrast to interacting polymer chains, the critical volume fraction shifts to smaller values with increasing q, while the critical polymer volume fraction increases at the same time as observed in interacting polymers solutions. But whereas the region where a stable homogeneous colloid-polymer mixture is increasing in interacting polymer solutions, the area underneath the binodal shrinks with increasing q in an ideal polymer solution. In summary, we note that the general trends of the phase behaviour are recovered by the GFVT even in the protein limit. Thus, we conclude that GFVT gives quantitative predictions for $q \lesssim 1$ (colloid regime) and describes polymer-colloid mixtures qualitatively for $q > 1$ (protein regime), capturing the general trends correctly.

Finally, we note that there is a urgent need for simulations of the fluid-solid and gas-liquid-solid phase behaviour to compare with our analytical theory.

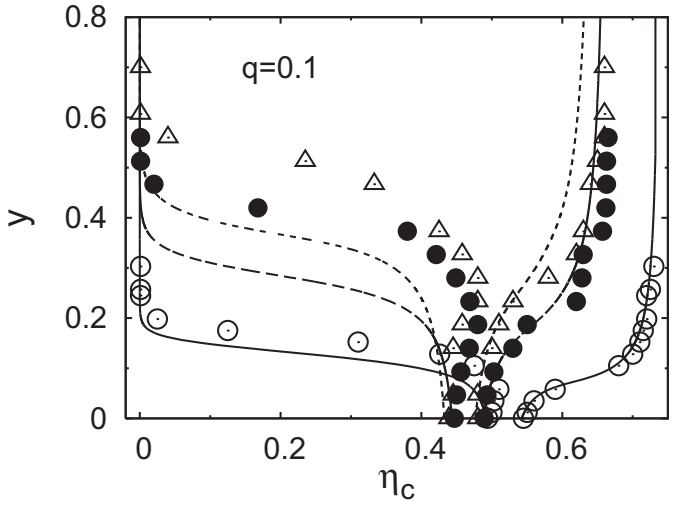

Figure 3.8: Phase diagram for a mixture of charged colloids and ideal polymers with polymer-to-colloid size ratio $q = 0.1$. The data points described the phase boundaries obtained from computer simulations taken from [140] for for various $2\kappa a$ values ($2\kappa a \to \infty$, $m = 1.0$ ($\circ$); $2\kappa a = 100$, $m = 1.110$ ($\bullet$); $2\kappa a = 80$, $m = 1.138$ ($\triangle$)). The curves correspond to the binodals calculated from GFVT for ideal polymers (solid curve: $m = 1.0$, dashed curve: $m = 1.110$, short dashed curve: $m = 1.138$).

3.4.2 Comparison with previous Monte Carlo simulations on charged colloid-polymer mixtures

In Figs. 3.8, 3.9 and 3.10 we compare the phase diagram calculated from GFVT for mixtures of charged colloids and ideal polymer with computer simulations from Fortini *et al.* [140] for $q = 0.1$, $q = 0.6$ and $q = 1.0$. The expressions for the Helmholtz free energy of charged colloids and ideal polymer solutions are obtained from Eq. (3.25) and (3.26) in the limit $y \to 0$. As seen in Fig. 3.8, GFVT predicts the the solid branch of the fluid-solid coexistence curve (solid curve) well for $m = 1.0$ and $q = 0.1$, but slightly underestimates the fluid branch for increasing colloid volume fractions. In case of charged colloids (dashed and short dashed curves in Fig. 3.8), GFVT systematically underestimates the fluid branches of the fluid-solid coexistence curves. For $q = 0.6$ (Fig. 3.9), GFVT predicts the location of critical point in the phase diagram astonishingly well for all values of m under consideration, but the theory fails to recover the widening of the fluid-solid coexistence curve with increasing polymer concentration. Thus, GFVT overestimates significantly the polymer concentrations at the triple point. For $q = 1.0$ (Fig. 3.10) the gas-liquid coexistence predicted from GFVT are too narrow as compared to the computer simulation data, indicating that GFVT underestimates the polymer induced osmotic pressure.

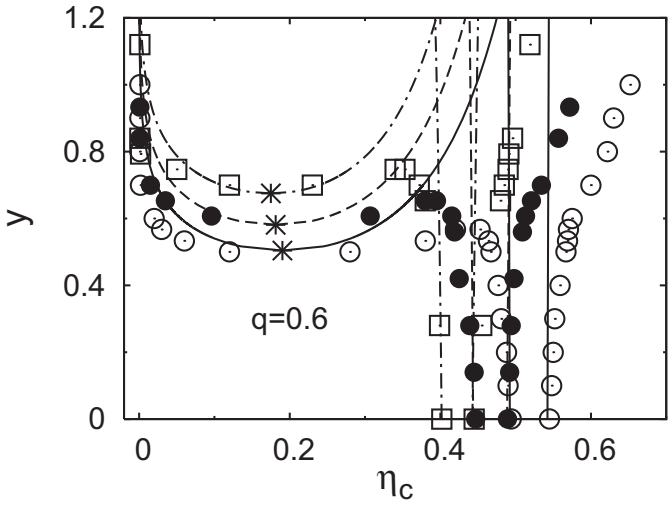

Figure 3.9: Phase diagram for a mixture of charged colloids and ideal polymers with polymer-to-colloid size ratio $q = 0.6$. The data points described the phase boundaries obtained from computer simulations taken from [140] for for various $2\kappa a$ values ($2\kappa a \to \infty$, $m = 1.0$ ($\circ$); $2\kappa a = 100$, $m = 1.110$ ($\bullet$); $2\kappa a = 80$, $m = 1.225$ ($\square$)). The curves correspond to the binodals calculated from GFVT for ideal polymers (solid curve: $m = 1.0$, dashed curve: $m = 1.110$, dashed-dotted curve: $m = 1.225$).

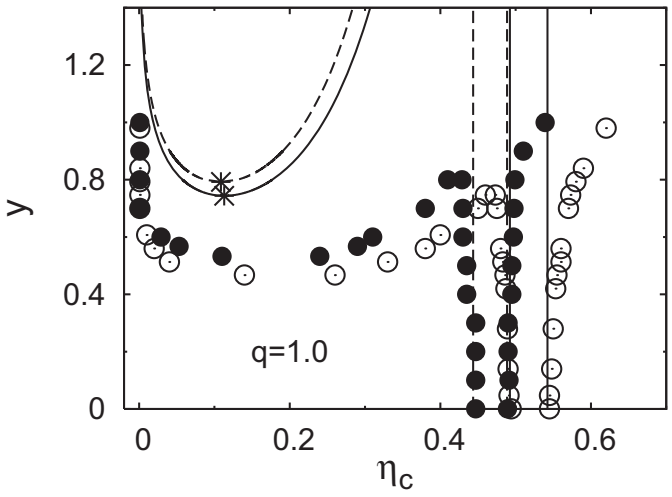

Figure 3.10: Phase diagram for a mixture of charged colloids and ideal polymers with polymer-to-colloid size ratio $q = 1.0$. The data points described the phase boundaries obtained from computer simulations taken from [140] for for various $2\kappa a$ values ($2\kappa a \to \infty$, $m = 1.0$ ($\circ$); $2\kappa a = 100$, $m = 1.110$ ($\bullet$)). The curves correspond to the binodals calculated from GFVT for ideal polymers (solid curve: $m = 1.0$, dashed curve: $m = 1.110$).

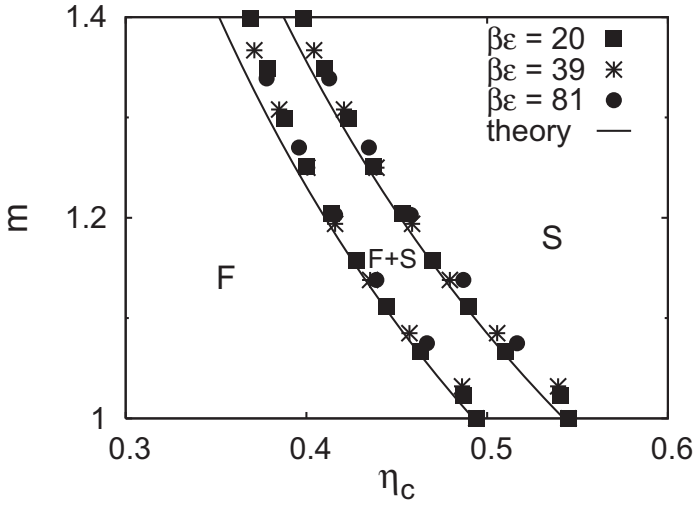

Figure 3.11: Fluid-solid coexistences for various values of the effective volume fraction factor m on the fluid-solid coexistence regime. The capital letters indicate the phase region where a stable fluid (F) or a stable solid phase (S) is observed. A fluid phase coexists with a fcc-solid phase in the gap between the two curves ($F + S$). The solid curves are calculated from our free-energy expressions for the weakly charged spheres (Eq. (3.8-3.10)). The symbols correspond to Monte Carlo simulation data of Hynninen and Dijkstra [156] for three different contact values, $\beta\epsilon$, of the repulsive pair interaction potential (Eq. (3.1)); see legend. The curves represent the binodal curves calculated using the free energy expressions of Eqs. (3.9) and (3.10) for the fluid and fcc-solid, respectively.

3.4.3 Phase behaviour of charged colloid-polymer mixtures

Next we turn to the main topic of this chapter: the phase behaviour of charged colloidal particles and polymers in either a good or a θ-solvent.

First, we focus on a pure hard-sphere dispersion without charges ($1/\kappa = 0$, or, correspondingly, $m = 1.0$) and without any added polymers ($y = 0$). In this limiting case we recover the hard-sphere fluid-solid phase coexistence at $\eta_c = 0.492$ (fluid) and $\eta_c = 0.542$ (solid). These values agree well with the freezing and melting volume fractions of 0.494 and 0.545, respectively, observed in computer simulations [157]. If the colloidal particles are charged ($m > 1$), the effective volume increases (see Eq. (3.4)), and thus, the freezing and melting volume fractions shift to lower values as shown in Fig. 3.11. Here, the included data points are the fluid-solid coexistence data from Hynninen and Dijkstra [156], obtained from Monte Carlo simulations for repulsive contact potentials of $\beta\epsilon = 20$, 39 and 81, respectively. We note from Fig. 3.11 that, as expected, the data collapse for different $\beta\epsilon$-values when m is plotted on the ordinate.

We proceed to elucidate, first, the influence of the solvent quality on the (global) phase behaviour and, secondly, the interplay between charge-induced repulsions

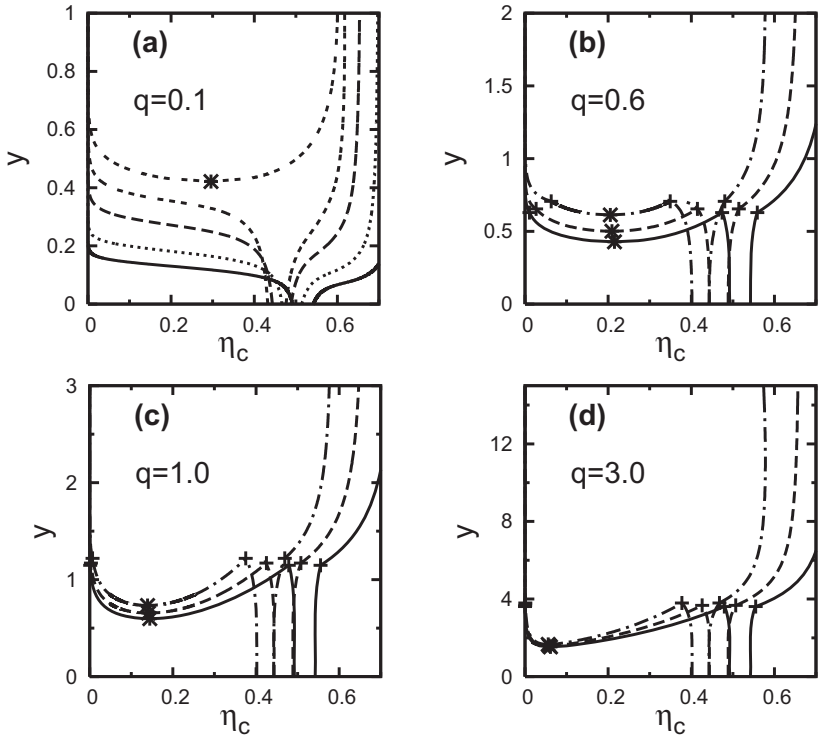

Figure 3.12: Phase diagram for mixtures of colloids carrying screened electrostatic charges and polymers at the θ-condition. The solid curves describe uncharged (infinite screening) colloidal dispersions ($m = 1.0$, or $\kappa a \to \infty$, respectively). The dotted curve is obtained for $m = 1.054$ (or, $\kappa a = 100$ for $\beta\epsilon = 20$) and the dashed curves for $m = 1.110$ (or, $\kappa a = 50$ for $\beta\epsilon = 20$). The short-dashed curve describes the phase coexistence obtained for $m = 1.138$ (or, $\kappa a = 40$ for $\beta\epsilon = 20$) and the dashed-dotted curves represent the phase coexistence curves for $m = 1.225$ (or, $\kappa a = 25$ for $\beta\epsilon = 20$). The plus symbols indicate the triple points, and the asterisks mark the critical points of the gas-liquid phase transition. Note that the reservoir polymer concentration is plotted as the ordinate. Thus, the tie-lines are parallel to the abcissa.

versus polymer-induced attractions. Figs. 3.12 and 3.13 show the phase behaviour for four different size ratios ($q = 0.1$, $q = 0.6$, $q = 1.0$ and $q = 3.0$), for polymers in a θ-solvent (Fig. 3.12) and under good solvent conditions (Fig. 3.13), respectively. Note that we plot the phase diagrams in the η_c-y plane, with y denoting the normalised reservoir polymer concentration. Thus, the tie-lines (not shown) are horizontal.

Adding non-adsorbing polymers induces an attractive interaction, and for small q the fluid-solid coexistence region widens upon increasing the polymer concentration (see, e.g., Figs. 3.12 (a) and 3.13(a)). For $q = 0.1$, the depletion-induced attractive interactions are too short-ranged to induce a stable gas-liquid phase separation and only a stable (or equilibrium) fluid-solid phase separation is ob-

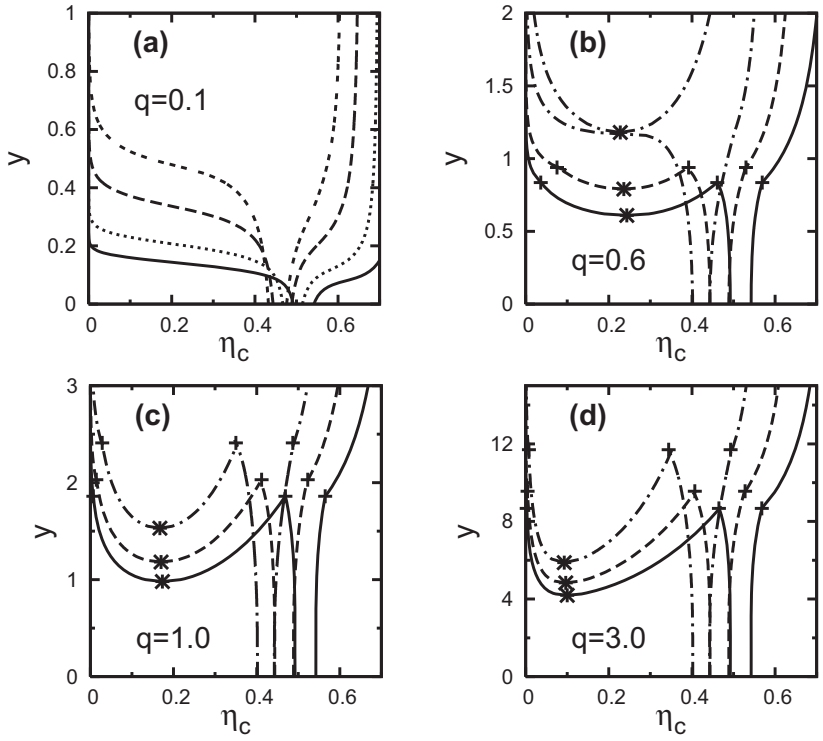

Figure 3.13: Phase diagram for mixtures of colloids carrying screened electrostatic charges and polymers at good solvent conditions. The solid curves describe uncharged (infinite screening) colloidal dispersions ($m = 1.0$, or $\kappa a \to \infty$, respectively). The dotted curve is obtained for $m = 1.054$ (or, $\kappa a = 100$ for $\beta\epsilon = 20$) and the dashed curves for $m = 1.110$ (or, $\kappa a = 50$ for $\beta\epsilon = 20$). The short-dashed curve describes the phase coexistence obtained for $m = 1.138$ (or, $\kappa a = 40$ for $\beta\epsilon = 20$) and the dashed-dotted curves represent the phase coexistence curves for $m = 1.225$ (or, $\kappa a = 25$ for $\beta\epsilon = 20$). The plus symbols indicate the triple points and the asterisks mark the critical points of the gas-liquid phase transition. Note that the reservoir polymer concentration is plotted as ordinate. Thus, the tie-lines are parallel to the abcissa.

served. The metastable gas-liquid coexistence curve lies within the fluid-solid coexistence region as shown for $m = 1.138$ in Fig. 3.12 (a). In Fig. 3.12 (a) and 3.13 (a), the fluid-solid coexistence curves shift to higher reservoir polymer concentration y with increasing Debye screening length κ^{-1}, or, correspondingly, with increasing m. Hence, the one-phase region underneath the fluid-solid coexistence curves, where a stable mixture at low polymer and colloid concentrations exists, increases with increasing m. This behaviour is expected since the short-ranged depletion-induced interactions are more and more compensated by the increasing electrostatic repulsions with decreasing κ.

For larger q, the depletion-induced attraction becomes longer-ranged and a stable gas-liquid phase coexistence is manifested. The polymer-to-colloid size

	m	q^{cep}	$q_{\mathrm{s}}^{\mathrm{cep}}$	y^{cep}	α^{cep}	$\eta_{\mathrm{c}}^{\mathrm{cep}}$
θ-solvent:	1.0	0.34	0.29	0.31	0.36	0.32
	1.11	0.40	0.30	0.43	0.43	0.27
	1.225	0.49	0.30	0.59	0.51	0.23
good solvent:	1.0	0.39	0.27	0.43	0.38	0.32
	1.11	0.47	0.27	0.68	0.46	0.27
	1.225	0.61	0.25	1.21	0.57	0.22

Table 3.1: Values obtained from the generalised free-volume theory that characterise the critical end point for colloids mixed with polymers in a θ-solvent (upper part) and in a good solvent (lower part). The effect of charges is embodied in the parameter m (see text). For $m > 1$, the colloids are charged.

ratio, at which this transition from a metastable to a stable phase coexistence between two fluids with low and high colloidal density takes place, is described by the critical end point [148]. This quantity marks the boundary condition for a colloidal liquid. The values that characterise the critical end point obtained from GFVT are summarised in Table 3.1 for colloids mixed with polymer in a θ-solvent and in a good solvent. Here, $m = 1$ corresponds to the hard sphere case, $\kappa \to \infty$, and $m = 1.110$ corresponds to a inverse screening length of $\kappa a = 50$, and $m = 1.225$ to $\kappa a = 25$, with $\beta\epsilon = 20$ assumed throughout.

As shown in Figs. 3.12 (b,c,d) and 3.13 (b,c,d), in the hard-sphere case of infinite screening, ($m = 1$) and for $m = 1.110$, a gas-liquid coexistence curve manifests itself at low reservoir polymer concentrations with respect to the fluid-solid phase coexistence curve for $q = 0.6$, 1.0, and 3.0. In contrast, Fig. 3.13 (b) for $q = 0.6$, $m = 1.225$ shows a metastable gas-liquid coexistence line (dashed-dotted curve), which nearly touches the fluid-solid coexistence curve. For $q = 1.0$ and $q = 3.0$, the fluid-solid curves are stable for $m = 1.225$.

In the hard-sphere limit (solid curves) and for small q (i.e., $q = 0.1$), there is nearly no difference between the fluid-solid phase coexistence curves for polymers in a θ-solvent and for polymers in a good solvent (compare Figs. 3.12 (a) with Fig. 3.13 (a)). The critical colloid volume fraction is also similar for both solvent conditions (see Fig. 3.16 and 3.17, and the discussion on this later on). With increasing q, the stability of the mixed phase increases. Furthermore, the binodals are shifted to higher reservoir polymer concentrations for polymers in good solvent conditions, as compared to chains in a θ-solvent at larger size ratios. To induce a gas-liquid phase transition at good solvent conditions, y is about a factor of two higher than for polymers in a θ-solvent. Similar trends have been observed by Schmidt and Fuchs [133].

Electrostatic repulsions between the colloids in general stabilise the homogeneous phase. Hence, more polymers have to be added to induce sufficient attrac-

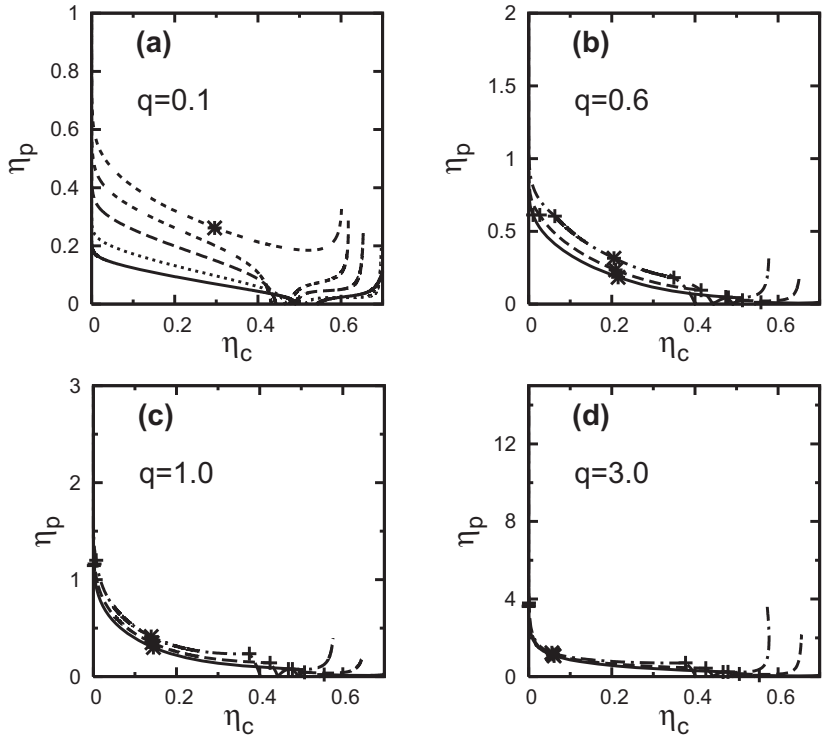

Figure 3.14: Phase diagram for mixtures of colloids carrying screened electrostatic charges and polymers at the θ-condition. In contrast to Fig. 3.12, the coexistence curves are plotted here in the η_p-η_c plane with the system polymer concentration. The solid curves describe uncharged (infinite screening) colloidal dispersions ($m = 1.0$, or $\kappa a \to \infty$, respectively). The dotted curve is obtained for $m = 1.054$ (or, $\kappa a = 100$ for $\beta\epsilon = 20$) and the dashed curves for $m = 1.110$ (or, $\kappa a = 50$ for $\beta\epsilon = 20$). The short-dashed curve describes the phase coexistence obtained for $m = 1.138$ (or, $\kappa a = 40$ for $\beta\epsilon = 20$) and the dashed-dotted curves represent the phase coexistence curves for $m = 1.225$ (or, $\kappa a = 25$ for $\beta\epsilon = 20$). The plus symbols indicate the triple points and the asterisks mark the critical points of the gas-liquid phase transition.

tion, and hence, the phase separation curves shift to higher y-values as observed in all phase diagrams. Interestingly, the influence of electrostatic repulsions on the location of the phase boundaries is much more pronounced in case of good solvent conditions than for a θ-solvent. The effect of the solvent quality on the phase behaviour becomes especially apparent in the protein limit (i.e., when $q = 3.0$), see Fig. 3.12 (d) and Fig. 3.13 (d). In case of a θ-solvent, the binodal at low colloid volume fraction is almost unaffected by the electrostatic repulsion (Fig. 3.12 (d)), whereas in a good solvent the homogeneous fluid phase becomes considerably stabilised with increasing m (Fig. 3.13 (d)). This is due to the fact that q_s is much smaller than q at the binodal for $q = 3.0$ especially under good solvent conditions. To make this explicit we give some values at the gas-liquid

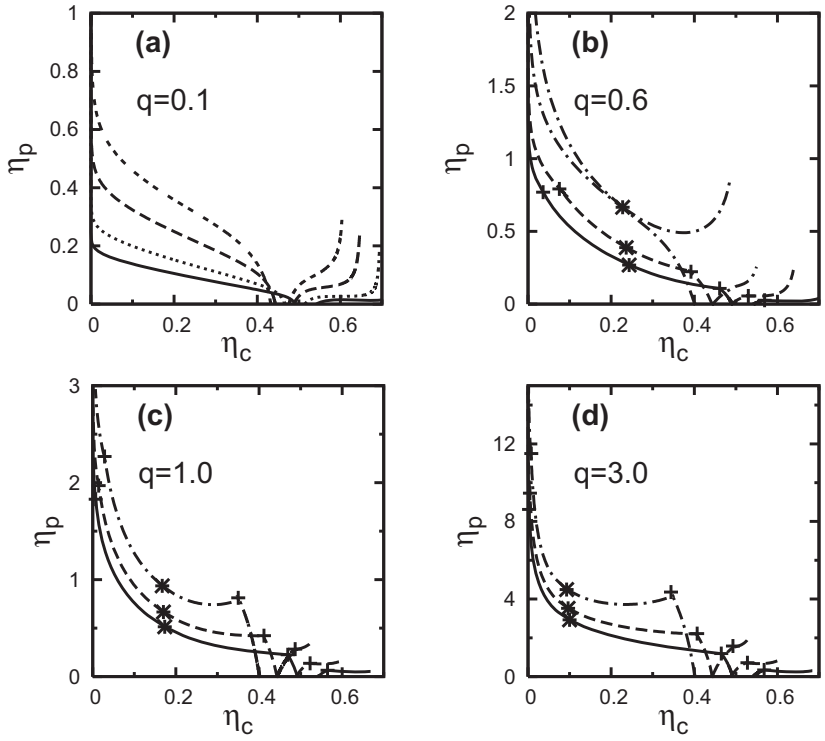

Figure 3.15: Phase diagram for mixtures of colloids carrying screened electrostatic charges and polymers at good solvent conditions. In contrast to Fig. 3.13, the coexistence curves are plotted here in the η_p-η_c plane with the system polymer concentration. The solid curves describe uncharged (infinite screening) colloidal dispersions ($m = 1.0$, or $\kappa a \to \infty$, respectively). The dotted curve is obtained for $m = 1.054$ (or, $\kappa a = 100$ for $\beta\epsilon = 20$) and the dashed curves for $m = 1.110$ (or, $\kappa a = 50$ for $\beta\epsilon = 20$). The short-dashed curve describes the phase coexistence obtained for $m = 1.138$ (or, $\kappa a = 40$ for $\beta\epsilon = 20$) and the dashed-dotted curves represent the phase coexistence curves for $m = 1.225$ (or, $\kappa a = 25$ for $\beta\epsilon = 20$). The plus symbols indicate the triple points and the asterisks mark the critical points of the gas-liquid phase transition.

critical point where $q_s = 0.5$ at $m = 1.0$ and $q_s = 0.4$ at $m = 1.225$ for colloidal spheres plus polymer chains in a good solvent, while in a θ-solvent, $q_s = 0.7$ at $m = 1.0$ and $q_s = 0.7$ at $m = 1.225$.

Actually, the depletion thickness becomes of the order of the correlation length ξ for $q > 1$ (protein regime) in semi-dilute polymer solutions and decreases with increasing y. Thus, even a short-ranged repulsion due to charges might be sufficient to compensate the depletion-induced attractions and, therefore, can have a large influence on the phase diagram.

As a practical illustration we plot the phase diagrams in Fig. 3.14 and 3.15 for $q = 0.1$, 0.6, 1 and 3 in the η_p-η_c representation employing the *system* polymer concentration. These can be compared with experimental data.

To discuss the influence of electrostatic repulsion and the effect of different solvent qualities on characteristic points that quantify the global phase behaviour, i.e. the critical point, the critical end point, and the triple point, we turn to Figs. 3.16 and 3.17. Here, these characteristic state points are plotted as a function of the colloid-to-polymer size ratio $1/q$. Pluses (+) indicate the triple points and open diamonds ($\diamond$) the critical points. The critical end points are marked by an asterisk ($*$). The curves interconnect the volume fractions of the gaseous, liquids and solid phase coexisting at the triple point as a function of q. A curve connecting several critical points as a function of q is called a critical line. The full curve interconnects characteristic state points for $m = 1.0$, and the dotted and dashed curves link the triple and critical points for $m = 1.110$ and $m = 1.225$, respectively. The critical end points shift to larger q-values with increasing electrostatic repulsions, which is at variance with Figs. 3.12 and 3.13. In addition, the volume fractions at the triple point and the critical points reduce to lower values when increasing the electrostatic repulsions. Due to the fact that the depletion thickness reduces by increasing the solvent quality, gas-liquid phase separation sets in at larger q-values in case of interacting polymers in a good solvent. Adding electrostatic repulsions strongly reduces the liquid window; the range of colloid concentrations and polymer-to-colloid size ratios where a colloidal liquid exists. When comparing this with mixtures of charged spheres with non-interacting polymers, one observes that the phase diagrams with interacting polymers are shifted

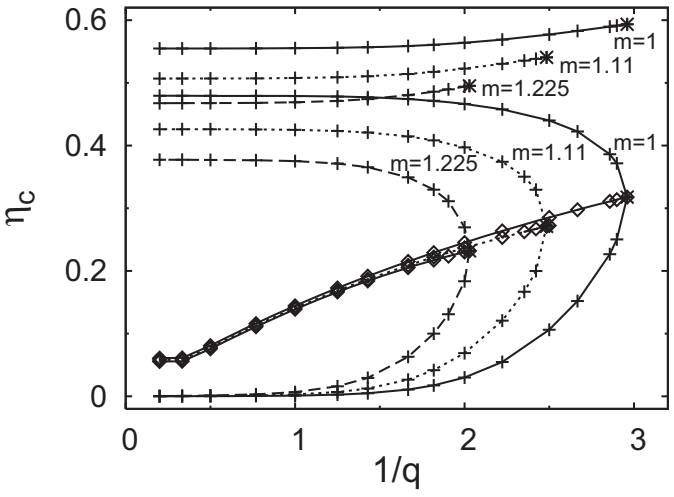

Figure 3.16: Triple points (+), critical points ($\diamond$) and critical end points ($*$) as a function of the inverse of polymer-to-colloid size ratio, $1/q = a/R_g$, for mixtures of non-adsorbing polymers in a θ-solvent and uncharged colloids ($m = 1.0$, solid curve) and for colloids carrying screened electrostatic charges ($m = 1.110$, dotted curve and $m = 1.225$, dashed curve).

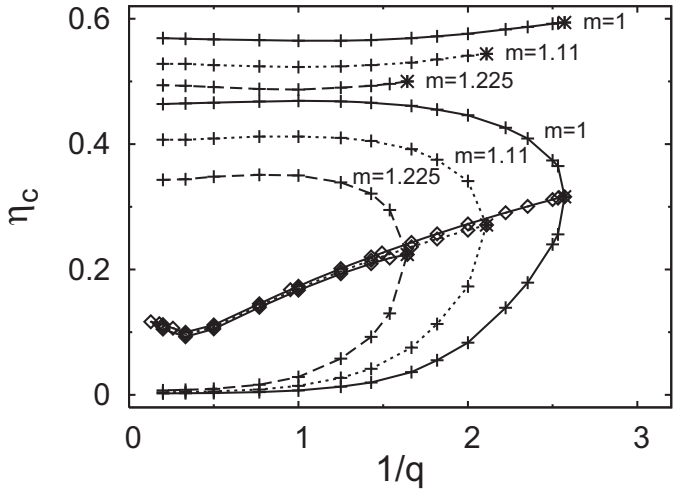

Figure 3.17: As in Fig. 3.16 but now for interacting polymers in a good solvent.

to significantly higher polymer concentrations for $q > 0.5$ [140].

Fig. 3.16 and 3.17 show that the critical colloid volume fraction, η_c^{crit}, converges towards a finite value in the protein limit (i.e., for $q \to \infty$), as observed by Bolhuis *et al.* [132,155]. But whereas η_c^{crit} approaches a constant value in case of a θ-solvent (Fig. 3.16), η_c^{crit} has a minimum for $q = 3.0$ and then increases again slightly for $q \to \infty$ in case of a good solvent (Fig. 3.17). This observation can be explained again by the fact that η_c^{crit} is determined by the range of attraction, i.e., by the effective polymer-to-colloid size ratio. In the semi-dilute limit the effect size δ becomes of the order of ξ ($\xi \ll R_g$) and, thus, becomes independent of q. Therefore, η_c^{crit} approaches a constant for $q \to \infty$. In case of a θ-solvent, the depletion-induced range of attraction, δ, is, even for $q \to \infty$, larger than the range of repulsion caused by the hard-sphere plus Coulomb repulsion, and, hence η_c^{crit} continuously decreases for increasing q. In contrast, in case of a good solvent, δ is small to such a degree (compare Fig. 3.3) that it is overcompensated by the repulsive interactions so that η_c^{crit} goes through a minimum at $q \approx 3$ and then slightly increases for larger q-values (Fig. 3.17). We note further, that the dominant contribution to the repulsive interactions is due to the hard-sphere contribution for all κ-values under investigation. Therefore, η_c^{crit} becomes independent of m for $q \to \infty$ in both cases.

We note as a critical remark that conceptual difficulties arise is mapping the screened electrostatic Coulomb interactions onto hard-sphere ones. Here, one has to be aware of the problems which might occur in conjunction with such a procedure as indicated in the following (see also [158] for a general discussion on effective pair interaction potentials). In general, as long the polymer chains do not carry charges (i.e., as long we do not consider polyelectrolytes as

depletion agents) the polymer-induced depletion interactions are driven by geometrical, excluded volume effects and are thus 'entropy driven' [5]. On the other hand, the repulsive pair interactions of the charged colloids are transmitted by an electric field caused by the surface and (microionic) space charges. Thus, polymer-induced depletion effects and screened electrostatic interactions are of a different physical origin, and, hence, independent from each other. However, by mapping the screened electrostatic Coulomb interactions onto effective hard-sphere ones, the two physically independent interactions becomes geometrically related. In particular, it is unclear whether the depletion thickness must be added to the effective hard-sphere particle or to the bare one, or, whether the polymer size has to be scaled so that the colloid-polymer mixtures remains additive as proposed by Denton and Schmidt [139]. Such a mapping obviously fails completely if the range of the repulsive screened Coulomb interactions exceeds the range of the attractive interaction potential, u_{attr}, induced by the polymer chains in solution or when $\beta u_{\mathrm{attr}} \sim \mathcal{O}(1)$. Thus, our model describes mixtures of charged colloids and polymers dispersed in an electrolyte solvent only in the limit of weakly charged or, respectively, highly screened colloidal particles with thin double layers. This procedure might lead to non-physical predictions when used ad-hoc without precaution.

3.4.4 A mixture of globulin proteins and dextran in an aqueous salt solution

As a practical example, we compare in the following our theoretical results with the phase behaviour of globulin dispersions with added non-absorbing dextran. Fortini *et al.* [140] have shown that mapping the screened electrostatic repulsive interactions onto effective hard-sphere ones is accurate for $m \lesssim 1.225$ (see [140], Fig. (2), p. 7789, and Fig. (3.11) in this work). Such high salt conditions are often encountered to screen the Coulomb interactions and, thus, to induce crystallisation. Hoskins *et al.* [159] have experimentally determined the phase behaviour of mixtures of globulin and dextran which falls into that regime. In particular, they observed gas-liquid demixing with increasing dextran concentration using turbidity measurement. The solutions with varying polymer concentrations were prepared at $pH = 6.4$ in the presence of $c_{\mathrm{s}} = 0.5\,\mathrm{mol/l}$ NaCl. At this pH, globulin is assumed to carry $Z = 25$ negative charges [160]. It's mass density is $1.351\,\mathrm{g/cm^3}$ [161] and it has a Stokes radius of $a = (5.7 \pm 0.3)\,\mathrm{nm}$ [161] and a molar mass of $150\,\mathrm{kg/mol}$ [159]. The samples were stored at $T = (290 \pm 2)\,\mathrm{K}$. At this temperature the Bjerrum length is $l_{\mathrm{B}} = 0.71\,\mathrm{nm}$.

Under these conditions, we have $\beta\epsilon = 0.19$ as contact potential, and $\kappa a = 13.3$ for the Debye screening parameter, where we have assumed $\rho_{\mathrm{c}} = 0$ in Eq. (3.2). Then, from Eq. (3.4) and Eq. (3.3), we obtain $m = 1.020$. Thus, our model calculations are applicable here. We note that m always decreases with increasing

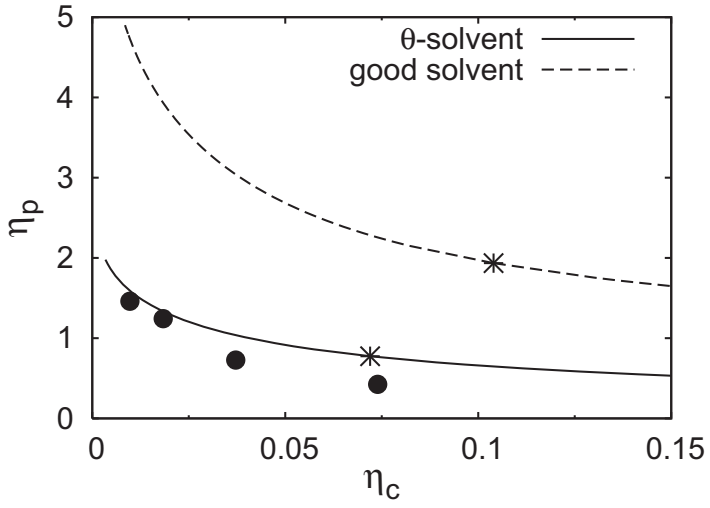

Figure 3.18: Phase diagram of a mixture of globulin and dextran at $pH = 6.4$ in 0.5 mol/l NaCl. The data points are redrawn from Hoskins *et al.* [159]. The solid curve is the theoretically predicted binodal obtained using GFVT for weakly charged spheres plus interacting polymers for $q = 2.3$ and $m = 1.020$ at $T = (290 \pm 2)$ K, assuming θ-solvent conditions. The dashed curve is the theoretically predicted binodal for $q = 2.3$ and $m = 1.020$, assuming a good solvent. The asterisks mark the critical points calculated from GFVT.

η_c within the DLVO-approximation, due to the contribution to the electrostatic screening by the surface released counter-ions (see Eq. (3.2)). It follows that the condition on m is also fulfilled for all non-zero protein volume fractions η_c. For example, one obtains $m = 1.018$ at $\eta_c = 0.4$ and $c_s = 0.5$ mol/l (i.e., $\beta\epsilon = 0.18$ and $\kappa a = 13.8$). However, for simplicity we will neglect the (colloidal) density dependence of κ in the following. Therefore, we use $m = 1.020$. Hoskins *et al.* [159] used dextran with a molar mass of $M_w = 267$ kg/mol, which has a radius of gyration of $R_g = 13$ nm [162]. Hence, we use $q = 2.3$. In Fig. 3.18, we compare the experimentally observed phase diagram of Hoskins *et al.* [159] with our from theoretically predicted GFVT binodal on assuming θ-solvent conditions. Additionally, Fig. 3.18 shows the theoeretically predicted binodal for good solvent conditions (dashed curve). The theoretical gas-liquid coexistence curve slightly overestimates the polymer concentration at which phase separation sets in slightly with increasing η_c. In contrast, the calculated binodal for a good solvent (dashed curve) overestimates largely the polymer concentration at the gas-liquid coexistence. The remaining deviation of the theoretically predicted binodal from the experimental data points might be due to the branched structure of dextran [162], and presumably also due to the polydispersity in R_g, leading to an underestimation of the osmotic pressure and of the range of attraction and, thus, to a shift of the calculated gas-liquid coexistence curve to larger

polymer concentrations. Nevertheless, the theoretical and experimental binodals agree overall well, considering that no adjustable parameters have been used.

3.5 Conclusions

We have investigated the influence of additional, charge-induced repulsions between the colloids, and the effect of interacting polymers in good and θ-solvent conditions, on the phase behaviour of colloid-polymer mixtures. This has been be accomplished by incorporating colloidal electrostatic repulsions into a recently formulated generalised free-volume theory. First, we have demonstrated that the proposed theory is in quantitative agreement with previously performed Monte Carlo computer simulation results for uncharged colloids for polymer-to-colloid size ratios smaller than one, and in overall good semi-quantitative agreement for size ratios above unity. Secondly, for charge-stabilised colloidal particles, we find a strong influence of the range of repulsion on the phase stability of mixtures of polymer chains and charged spheres. The charge-induced repulsion between the colloids stabilises colloid-polymer mixtures against gas-liquid phase separation. In addition, with increasing repulsion the crystallisation curve shifts to lower colloid volume fractions. Thirdly, we find that the solvent quality also affects the phase diagram significantly. The stability region where a stable fluid is found, is larger for a good solvent than for a θ-solvent; the influence of the solvency is stronger for a larger polymer-to-colloid size ratio. This is due to the fact that phase separation takes place at larger polymer concentrations (normalised with the polymer overlap concentration). Finally, we find good agreement when comparing our theoretically predicted and experimentally observed binodal in an aqueous mixture of charged globulin (protein) and dextran (polysaccharide). From our work it follows that it is useful for experimentalists working on biological systems such as protein-polysaccharide mixtures to characterise the solvent quality of the biopolymers in solution. The solvent quality can significantly alter the phase stability.

4 Polymer depletion-driven cluster aggregation and demixing in charged-stabilised colloidal dispersions

In chapter 3, we have theoretically investigated the phase behaviour of mixtures of charge-stabilised colloidal spheres and non-adsorbing polymers. To exploit the phase behaviour and the stability of such mixtures also experimentally, we study in the following an aqueous dispersion of amorphous charged silica spheres with added dextran macromolecules. Due to surface-released counterions, the silica spheres carry negative surface charges which can be screened by adding sodium chloride. Attractive interactions between the colloidal particles are induced by adding dextran, a slightly branched polysaccharide, which does not adsorb on the silica-water interface, as we have explicitly verified in our experiments. Different from the theoretical model discussed earlier, these silica particles do not behave as hard spheres. Instead, the van der Waals forces induce strong attractions at close distances, causing aggregation at sufficiently high salinity. We demonstrate in the following that this aggregation can drastically influence the solution properties at sufficiently high salt concentrations, when the electrostatic repulsion is partially screened out. We find that the cluster-aggregation rate increases, as expected, with increasing salt concentration, and the dispersion becomes stable at sufficiently low salinity. This makes it possible to tune the strength of repulsion at will, depending whether one is interested in aggregation processes or equilibrium properties. By adding non-adsorbing polymers, a depletion-driven attraction is induced. In the present experimental study, we first investigate the influence of the range of colloidal repulsion and attraction on the cluster growth rate at low colloid volume fractions, using photon correlation spectroscopy. The polymer chains add an additional attraction to the van der Waals forces, so that the Coulomb barrier is lowered. As a consequence, an accelerated cluster growth rate is observed. If the polymer molar mass is sufficiently high, the polymers induce a long-range

attractive interaction, which can drive a fast initial phase separation, accompanied by a proceeding slow aggregation process. When the dispersed colloidal particles are not density matched, larger aggregates sediment under gravity, and a concentrated phase of colloidal clusters is formed at the container bottom (cluster fluid). Second, the time evolution of the non-equilibrium phase diagram, recorded for a varying range of the colloidal repulsion, and the resulting phase behaviour, is discussed in terms of an initial phase separation process. From comparing the non-equilibrium state diagram with the equilibrium phase diagram obtained from GFVT, we suggest that demixing procedes the slow aggregation of colloidal particles at high polymer concentrations, high colloid volume fractions and low salt concentrations.

4.1 Introduction

4.1.1 DLVO-theory of colloidal stability

Cluster-aggregation processes are ubiquitous in physics, chemistry and astrophysics and, therefore, have received intensive attention during the past [163,164]. Common to all these phenomena is the formation of fractal, statistically self-similar structures describable by universal scaling laws [165]. Accordingly, the formation and growth of non-equilibrium clusters has been intensively investigated in colloidal systems, where these structures can be directly imaged using, e.g., electron microscopy [166] and more recently, confocal microscopy techniques [167–169]. A first explanation for the coagulation of charged colloidal particles has been given by Derjaguin, Landau, Verwey and Overbeek (DLVO) in their theory of colloidal stability [12]. According to the classical DLVO theory, a colloidal dispersion can be stabilised against aggregation by sufficient electrostatic repulsion. This is due to the fact that the attractive van der Waals (dispersion) force acts only at short inter-particle distances typically of the order of about 10% of the particle diameter. The van der Waals (vdW) attraction of two dispersed spheres can be approximately described by the effective pair potential [6],

$$u_{\mathrm{vdW}}(r) = -\frac{A_{\mathrm{H}}}{6}\left(\frac{2a^2}{r^2-4a^2}+\frac{2a^2}{r^2}+\ln\left[1-\frac{4a^2}{r^2}\right]\right), \tag{4.1}$$

for $r > 2a$. Here, r is the centre-to-centre particles distance, a is the radius of a colloidal sphere, and A_{H} is the Hamaker constant. The dispersion potential decays as $u_{\mathrm{vdW}}(r) \sim 1/r^6$ for large r, and diverges as $u_{\mathrm{vdW}}(r) \sim -(r-2a)^{-1}$ near contact distance $r = 2a$ [69]. The screened electrostatic inter-particle repulsion is described in the DLVO theory by the effective pair potential, $u_{\mathrm{el}}(r)$, with

$$\beta u_{\mathrm{el}}(r) = \frac{Z^2\, l_{\mathrm{B}}}{(1+\kappa a)^2}\,\frac{\exp\left[-\kappa(r-2a)\right]}{r}, \tag{4.2}$$

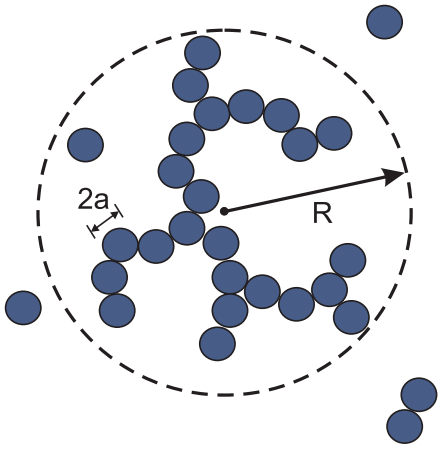

Figure 4.1: Sketch of an aggregation cluster of size R consisting of colloidal particles of radius a.

for $r > 2a$, with $1/\beta = k_\mathrm{B}T$, Bjerrum length $l_\mathrm{B} = e^2/\left(4\pi\varepsilon_0\varepsilon k_\mathrm{B}T\right)$, (effective) number of elementary charges, Z, on the colloidal surface, and the Debye screening parameter κ with $\kappa^2 = 4\pi l_\mathrm{B}\left(|Z|\rho_\mathrm{c} + 2\rho_\mathrm{s} + \rho_\mathrm{b}\right)$. Here, ρ_c, ρ_s, and ρ_b are the number densities of colloidal particles, monovalent salt ions, and ionic buffer molecules, respectively. The strength of the electrostatic potential part is quantified by the contact value $\beta\epsilon = Z^2 l_\mathrm{B}/[(1+\kappa a)^2 2a]$. The total pair potential of charged colloids in an electrolyte solution consists thus of the hard-sphere potential, $u_\mathrm{hs}(r)$, describing the excluded volume interaction of two spheres of diameter $2a$, the van der Waals attraction part, $u_\mathrm{vdW}(r)$, and the contribution $u_\mathrm{el}(r)$ describing the screened electrostatic repulsion arising from overlapping electric double layers. At sufficiently low salt concentration and large particle charge, the total effective pair potential,

$$u_\mathrm{DLVO}(r) = u_\mathrm{hs}(r) + u_\mathrm{vdW}(r) + u_\mathrm{el}(r)\,, \tag{4.3}$$

is dominated by $u_\mathrm{el}(r)$, and the system is practically purely repulsive. By adding salt, i.e., by increasing κ, the electrostatic repulsion decreases. If the range, κ^{-1}, of electrostatic repulsion becomes comparable to the range of the attractive dispersion forces, it becomes more likely that the surface-to-surface distance of two particles becomes so small that the dispersion attraction dominates. Under such a high-salt condition, the maximum in the pair interaction potential can be so small (Fig. 4.2) that the dispersion becomes unstable against aggregation (see Fig. 4.1). Then two particles stick irreversibly together after a collision event, since they are trapped in the deep primary minimum of the pair interaction potential. If a third particle collides with a dimer, a trimer is created and so on. Thus, particle clusters are growing in time and one speaks of an irreversible aggregation (IA) process. Cluster-aggregation processes in colloidal dispersions have been under investigation both experimentally [170–172] and theoretically [173,174] since the

early eighties. It has been verified experimentally that the kinetics of cluster formation depends significantly on the underlying aggregation mechanism. If the particles or clusters stick together irreversibly upon the first collision, the cluster growth rate is mainly determined by the diffusivity of the monomers (and clusters), and one refers to a diffusion-limited (cluster) aggregation (DLA, or DLCA, respectively) process. If, however, several collision events are required for two constituents to stick together irreversibly, the cluster-growth rate is determined by the monomer-monomer, or, more generally, the cluster-cluster, reaction kinetics. The corresponding process is called reaction-limited (cluster) aggregation (RLA, or RLCA, respectively). As one expects, a cluster grows faster in a DLA than a RLA process. In the former case, the cluster radius, R, obeys a power-law time dependence, according to $R(t) \sim t^{1/d_\mathrm{f}}$, characterised in three dimensions by a cluster fractal dimension $d_\mathrm{f}(\mathrm{DLA}) = 1.75 \pm 0.03$ [164]. For RLA, the cluster size is described by an exponential growth rate, $R(t) \sim \exp(t/\tau_a)$, characterised by the aggregation time τ_a. The clusters are obviously more compact in the case of RLA, since the monomers can diffuse deeper into the cluster, resulting in a larger fractal dimension of $d_\mathrm{f}(\mathrm{RLA}) = 2.1 \pm 0.1$ [164].

In contrast to the high salinity case considered so far, where the Coulomb barrier is so small ($\sim k_\mathrm{B}T$) that two particles can reach the primary minimum that causes irreversible aggregation after collision, there can be also circumstances where aggregation becomes reversible. Reversible aggregation (RA), or reversible flocculation, can occur when the electrostatic repulsion is only partially screened. With increasing electrostatic repulsion, the repulsive barrier, named Q (see Fig. 4.2), grows and can become much larger than $k_\mathrm{B}T$, so that irreversible aggregation becomes very unlikely. However, if the secondary minimum, which occurs at relatively large inter-particle distances, is relatively deep compared with k_BT, the colloidal particles can form loose and reversible bounded aggregates.

We note that the irreversible aggregation processes encountered in DLA and RLA are distinctly different from the reversible cluster aggregation [43]. The structures arising from reversible aggregation can be described by equilibrium statistical physics like, e.g., in the case of microphase separation [42], whereas the irreversible aggregation phenomena discussed in the present chapter require stochastic theory and kinetic equations for their description. The growth of a colloidal cluster has been described successfully for the first time by Smoluchowski in his rate equation for the evolution of the distribution function, $n(x,t)$, for the number of clusters of size x in time t [176],

$$\frac{\partial n(x,t)}{\partial t} = -n(x,t)\int_0^\infty dy\, K(x,y)\, n(y,t) + \frac{1}{2}\int_0^x dy\, K(y,x-y)\, n(y,t)\, n(x-y,t)\,. \tag{4.4}$$

Here, the collision rate in which a cluster of size x collides with a cluster of size y and forms a cluster of size $x+y$, is described by the kernel function $K(x,y)$. Obviously, $K(x,y)$ is symmetric in it's two arguments. The first loss term on

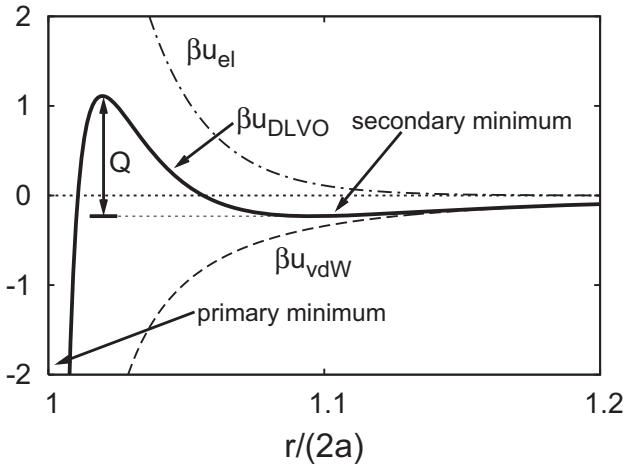

Figure 4.2: Typical DLVO pair potential ($a = 12\,\mathrm{nm}$, $Z = 440$, $c_\mathrm{s} = 0.3\,\mathrm{mol/l}$, $c_\mathrm{b} = 0.02\,\mathrm{mol/l}$, $\phi = 0.01$, $A_\mathrm{H} = 0.8 \times 10^{-20} (k_\mathrm{B}T)^{-1}$ [175], $T = 295\,\mathrm{K}$) of an unstable aqueous silica dispersion. The dashed-dotted line describes the repulsive potential part, $u_\mathrm{el}(r)$, (Eq. (4.2)) and the dashed curve the attractive part, $u_\mathrm{vdW}(r)$, (Eq. (4.1)). The solid curve is the total pair potential, $u_\mathrm{DLVO}(r)$. The height of the Coulomb barrier is denoted as Q. If Q is small and two particles approach each other, the primary minimum causes irreversible aggregation. However, if Q is large ($Q \gg 1$) and the vdW attraction strong, two spheres can get trapped transiently in the secondary minimum and reversible aggregation can occur.

the right-hand side of Eq. (4.4) accounts for the loss of clusters of size x due to the collision with clusters of size y, and the formation of a larger cluster of size $x + y$. The second (gain) term describes the formation of a cluster of size x due to the collision of a cluster of size $y \leq x$ with clusters of size $x - y$. The factor $1/2$ corrects for the double-counting in the number of combinations. If one assumes for simplicity that the two clusters of size x and y stick together only upon contact, the aggregation rate is given by [177],

$$K(x, y) = 2\pi D_0 a \frac{(x + y)^2}{xy}\,, \tag{4.5}$$

where D_0 is the single colloid (monomer) diffusion coefficient given by the Stokes-Einstein relation, and a is the colloid radius. This expression holds true for observation times $t \gg a^2/D_0$. As can be seen from integrating Eq. (4.4) over the interval $[0, \infty)$, this kernel ensures the conservation of mass (or particles) at $t = 0$, so that $\int_0^\infty dx\, n(x, 0) = n(a, 0) \equiv n_0$. Eqs. (4.4) and (4.5) are formulated such that the aggregation of clusters is solely determined by the Brownian diffusion of monomers (colloids) and clusters, i.e., they describe diffusion-limited aggregation or rapid flocculation. Note that the derivation of the rate equation for the formation of dimers at the initial stage of Brownian flocculation is summarised in appendix A, following Russel's derivation [178].

If the particle concentration is very small and the inter-particle attraction much larger than k_BT, a system-spanning fractal network is observed [179]. At far higher colloid volume fraction, ϕ, a gel-like structure is formed, which becomes glass-like with further increasing ϕ [180].

4.1.2 Depletion-induced non-equilibrium phase separation

Consider now what happens if, in addition to the vdW attractions, another source of attraction becomes operative. This is experimentally accomplished, for example, by a polymer-induced depletion interaction. The colloid attractions induced by adding non-adsorbing polymers to a colloidal suspension of spheres of radii a, can be described at small polymer concentrations by the Asakura-Oosawa-Vrij (AOV) model. In this simplifying model, the effective depletion pair potential is given by the product of the osmotic pressure of the polymer solution in the reservoir, Π_p^r, and the overlap volume $V_{\rm ov}(r)$, e.g., $u_{\rm AOV}(r) = -\Pi_p^r \cdot V_{\rm ov}(r)$ [98–100]. The effective depletion pair potential between two colloidal spheres due to phantom chains (described as mutually penetrable spheres) has been originally derived by Vrij and reads [100]

$$\beta u_{\rm AOV}(r) = -\frac{c}{c^*}\frac{(1+q)^3}{q^3}\left(1 - \frac{3r}{4(1+q)a} + \frac{r^3}{16(1+q)^3a^3}\right), \qquad (4.6)$$

where $2a < r < 2\,[a + R_{\rm g}]$. Here, $q = R_{\rm g}/a$ is the size ratio between the polymer radius of gyration, $R_{\rm g}$, and the radius of a colloidal sphere. The polymer concentration (mass per volume) is denoted by c, and the polymer overlap concentration is estimated by $c^* = 3M/(4\pi R_{\rm g}^3 N_{\rm A})$.

If one adds non-adsorbing polymers to the solution, the cluster-aggregation gets accelerated, because the polymer chains induce an additional depletion attraction to the DLVO-like pair interaction potential, which decreases the electrostatic repulsions and, as a consequence, aggregation due to the primary minimum becomes more likely. We note that the diffusivity of the colloidal particles is not significantly hindered when a dilute solution of polymers is added. In contrast to this, one finds dramatic effects on the phase behaviour when the range of attraction increases. For sufficiently large q, the solution can become unstable against a gas-liquid-like phase separation (see Fig. 4.3). For $q = 0.059$, Lu *et al.* [181] showed that the bi-continuous amorphous colloid structure initiated by spinodal decomposition becomes arrested. It has been shown that the spinodal decomposition arrest arise since the colloid particles aggregate, or experience a glass-like arrest in the denser colloidal phase [182–185]. Then, a sponge-like rigid structure is formed which behaves viscoelastically. The length scale for which spinodal decomposition becomes arrested can be determined by the interplay between the fastest growing wavelength of the density fluctuations leading to a demixing of the fluid, and the aggregation kinetics, which depends on ϕ, the colloid diffusion coefficient, and the specific form of the interaction potential. Thus, it is

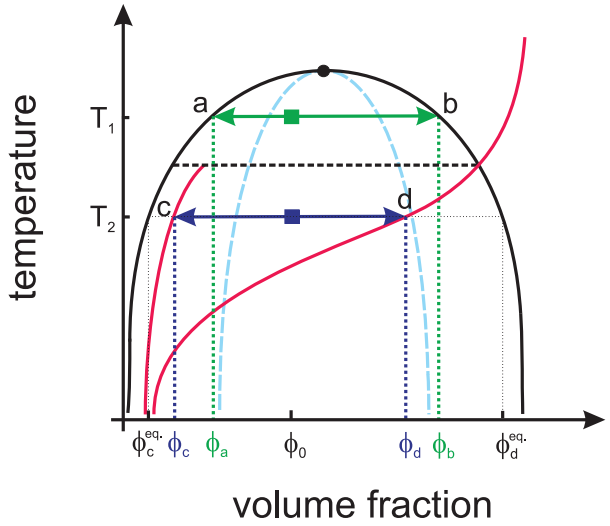

Figure 4.3: Sketch of a phase diagram in the temperature-colloid volume fraction phase space, as encountered in a colloid-like dispersion with short- and long-ranged attractive pair interactions. In case of polymer-induced depletion attractions, the inverse polymer concentration replaces the temperature axis. The solid black curve indicates the binodal line which terminates at the critical point (•), and the dashed blue curve marks the spinodal line. At shallow temperature quenches (■), the solution separates into a colloid-poor phase of volume fraction ϕ_a and a colloidal-rich phase ϕ_b along the tie-line (green double arrow). At two points of the black dashed horizontal line, the gel line (right red curve) intersects with the binodal. At deep temperature quenches (■) below the horizontal black dashed line, $\beta u_{vdW}(r)$ decreases due to the factor β, and gelation occurs in the colloid-rich phase at ϕ_d. Due to a glassy or percolation arrest in this denser phase, the spinodal decomposition of colloidal spheres gets arrested before equilibrium is reached, so that $\phi_c > \phi_c^{eq.}$ and $\phi_d < \phi_d^{eq.}$.

interesting to explore how the critical slowing down occurring during spinodal decomposition affects the aggregation process of colloidal particles.

Arrested spinodal decomposition occurs typically for colloid volume fractions in between 0.01 and 0.4, depending on the range of attractions. An explanation of the glass-like arrest of spinodal decomposition has been given by Manley *et al.* [185] based on mode-coupling theory (MCT). Even though MCT does not predict spinodal decomposition, the experimental data are explained quantitatively by this theory, which has been designed originally to describe the hard-sphere glass transition of the colloid-rich phase that occurs experimentally at $\phi \approx 0.58$. The reason why the MCT is useful also in describing arrested phase separation is the separation of time scales. In fact, phase separation sets in immediately after the sample mixing, leading to the aforementioned bi-continuous network of growing characteristic length scale, ξ, that characterises the width of the gills of the network. In contrast, the particles get arrested at later times after mixing when the density of the colloidal-rich phase is above the glass-transition value. When short-ranged attractive interactions between the colloidal particles are operative,

so that they can stick together after a collision event, clusters are formed instead during spinodal decomposition in the denser liquid phase [186–189]. This cluster formation is expected to take place at lower volume fractions, and on a shorter time scale during the spinodal decomposition process. The resulting clusters can sediment to the container bottom, and by this circumvent the formation of a container-spanning network. It should be emphasised that the kinetics of cluster-aggregation processes depends crucially on the colloid volume fraction, the strength and range of the repulsive electrostatic interactions, the binding mechanism (i.e., whether the colloids are chemically or physically connected), and the form of the reversible or irreversible aggregation mechanism. Thus, a large variety of mechanisms can lead to gelation.

Whereas at low ϕ the aggregation process can be well described by kinetic equations, and glassy solidification is captured quite well by the MCT approach, no general description exists so far for intermediate volume fractions, where non-equilibrium aggregation processes and equilibrium phase separation are operative. On the one hand, this complexity is certainly due to the fact that the dense concentration regime is not amenable to perturbation methods such as a virial expansion, since multi-body interactions are important. On the other hand, continuum theories describing appropriately the equilibrium phase behaviour do not capture aggregation phenomena.

Bergenholtz and Fuchs [190] have been the first to describe gel formation in colloidal dispersions with short-ranged attractive interactions using the MCT of non-ergodic arrest, used before only to study the liquid-glass transition. Thereafter, the similarities between gelation and glass transition, e.g., their kinetic origin, the basically unchanged fluid-like structure factor at the transition, the occurrence of two time-separated relaxation modes, have been experimentally observed by Segrè *et al.* [191]. As experimentally shown by Pham *et al.* [192], the MCT theory successfully describes the attractive glass transition for $\phi_c \geq 0.4$. Due to the success of MCT in predicting the phase behaviour of attractive glasses, and further experimental studies by Sedgwick *et al.* [169,193,194], Kroy *et al.* [195] have made an attempt to extend MCT to lower volume fractions. In the absence of a spinodal decomposition, i.e., for sufficiently short-ranged attractions, larger clusters are formed on a shorter time scale, as observed by experimentally by Segrè *et al.* [191]. When all monomers have been absorbed by the growing clusters, aggregation stops and gelation only occurs after these cluster have diffused sufficiently in space to get stuck (jammed) at a later stage. Kroy *et al.* have applied MCT to these clusters to describe this glass-like arrest. Accordingly, the theory is referred to as the cluster mode-coupling theory (CMCT). Besides these theoretical approaches, only a number of ad hoc explanations have been given to explain the experimental observations (see, e.g., Lu *et al.* [181] for a short overview).

Notwithstanding the lack of a complete theoretical understanding, to deepen our physical insight, we study in the following the dynamics of colloidal par-

ticles in a dextran solution in situations, where phase separation and cluster-aggregation interfere. We note that a gelation process which interrupts spinodal decomposition is often encountered in protein solutions (see chapter 2, and [57, 79]), where cluster-aggregation is unwanted because it inhibits protein crystallisation. Aside from proteins, materials made of such foam-like rigid structures (e.g., by drying the arrested network) have also the potential for technical applications [196].

In the present work, we investigate mixtures of nano-sized Ludox silica particles and dextran in water. We focus here on the effect of long-ranged depletion attractions where $0.49 \leq q \leq 2.6$. In section 4.2, the samples are characterised and the light scattering technique and the data evaluation are explained. We first demonstrate that the dextran polymers do not adsorb on the particle surface at the solvent conditions met in our experiments. In using light scattering, the growth of clusters is monitored. Thus, we concentrate on the percolation regime, where non-equilibrium clusters and a low-volume fraction gel are formed. In section 4.3, we first monitor the growing cluster size as a function of the added electrolyte, in the absence of added polymers. Then, dextran polymers are added which induce an additional depletion attraction between the charged colloidal spheres, and a depletion-driven cluster-growth is observed (section 4.4). In section 4.5, we monitor the effect of the salt concentration on the precipitation lines and construct a non-equilibrium state diagram. In addition, we discuss an initial phase separation and irreversible aggregation processes which are driven by an interplay of short-ranged vdW and long-ranged depletion attractions. Our experimental and theoretical results are summarised in the final section.

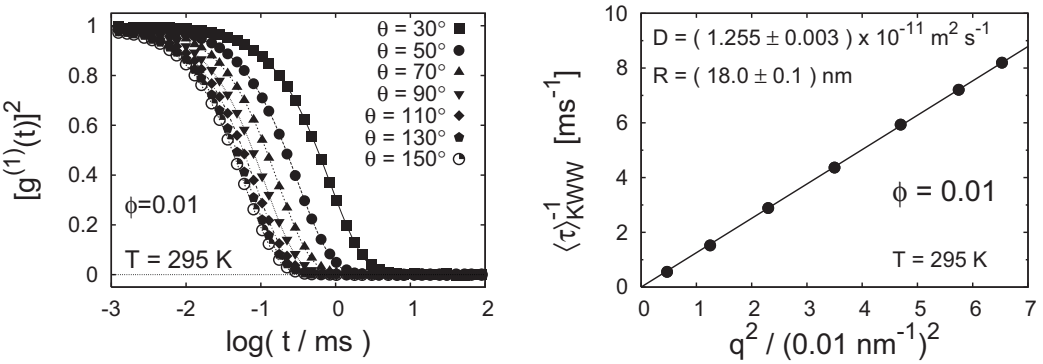

Figure 4.4: Left: Square of the normalised electric field autocorrelation function, $[g_1(t)]^2$, of a sample with $\phi = 0.01$ and $c_s = 0.15\,\mathrm{mol/l}$ for various scattering angles θ as indicated. Right: Inverse of the corresponding mean relaxation time, $\langle\tau\rangle_{\mathrm{KWW}}$, as a function of the square of the scattering wave number q.

4.2 Experiments

4.2.1 Sample materials

Silica particles (Ludox$^{\mathrm{TM}}$ TMA) were kindly provided by Grace Davison (Worms, Germany). These amorphous particles were supplied in a deionised aqueous stock dispersion of $p\mathrm{H} = 6.9$. The dispersion contains a mixture of 5-chloride-2-methyl-2H-isothiazol-3-on and 2-methyl-2H-isothiazol-3-on with a total volume fraction of 0.0025% to prevent fungal decay and bacterial growth. The density of the amorphous silica particles of $\rho_c = (2.1 \pm 0.1)\,\mathrm{g/cm^3}$ was determined from the weight loss when drying a known amount of dispersion, the colloidal dispersions density, and the density of water.

Dextran from Leuconostoc with molar masses $M = 4\times10^4\,\mathrm{g/mol}$, $5\times10^5\,\mathrm{g/mol}$ and $2\times10^6\,\mathrm{g/mol}$, respectively, were purchased from Fluka. The radius of gyration, R_g, of dextran is estimated, using the results from Nordmeier [162], to $R_g = 0.0633\times M^{0.427} = (5.8\pm0.4)\,\mathrm{nm}$, $(17\pm1)\,\mathrm{nm}$ and $(31\pm2)\,\mathrm{nm}$, respectively, on assuming a polydispersity of 15%. We note that the exponent of $0.427 < 0.5$ is indicative of a somewhat branched chain structure. The polymer overlap concentration, c^*, is estimated as $c^* = 3M/(4\pi N_{\mathrm{A}} R_{\mathrm{g}}^3)$, resulting in $c^* = 0.0796\,\mathrm{g/cm^3}$, $0.0391\,\mathrm{g/cm^3}$, and $0.0265\,\mathrm{g/cm^3}$ for $M = 4\times10^4\,\mathrm{g/mol}$, $5\times10^5\,\mathrm{g/mol}$, and $2\times10^6\,\mathrm{g/mol}$, respectively. The mass density of dextran is $\rho_p = 1.637\,\mathrm{g/cm^3}$ [197]. To ensure that dextran does not adsorb on the silica-water interface and to increase the colloidal stability, an ammonium-chloride buffer has been used (see below). The buffer concentration, c_b, was set to $0.02\,\mathrm{mol/l}$ with $p\mathrm{H} = 9.2\pm0.1$, and the ionic strength was varied by adding sodium chloride (Sigma-Aldrich). The aqueous Ludox dispersion was dialysed against the ammonium-chloride buffer solution for two weeks. For all solutions, the aqueous medium was taken from a Millipore ultra-clean facility. All solutions where properly sealed to

prevent evaporation of the dissolved ammonia. To avoid bacterial growth, N-methylisothiazolon-HCl (Chemos, Regenstauf, Germany) was added at a volume fraction of 0.0025%. Furthermore, the silica-containing dispersion was stored in plastic containers to prohibit wall-induced aggregation occurring in glass containers. The samples have been prepared from stock solutions to ensure rapid mixing of the polymer and the colloidal solutions. For this purpose, the dextran powder was dissolved in a buffer solution containing already the desired sodium chloride concentration. Stirring of the polymer solution was avoided to prevent disrupting the polymer chains. Shortly before the samples were prepared, the dialysed Ludox dispersion was mixed with a proper amount of a high concentrated sodium chloride solution (1 mol/l). Afterwards, the desired colloid-polymer mixture was prepared by adding proper amounts of the colloidal stock solution, the polymer solution and the salt-containing buffer solution. The suspension was then gently mixed. In this way, the polymer, colloid, buffer and salt concentrations are precisely known.

4.2.2 Experimental techniques and sample characterisation

Dynamic light scattering (DLS) experiments were performed on a ALV/CGS-8F S/N 060 laser goniometer system (ALV, Langen, Germany), using a 22 mW Helium-Neon-Laser (JDS Uniphase, Milpitas, USA) and a single avalanche photo diode detector. The temperature was set to $T = 295\,\mathrm{K}$ during all DLS measurements. Samples containing the colloidal dispersion only were filtered through a $0.45\,\mu$m pore-size Nylon filter (Roth, Karlsruhe, Germany) to remove dust. Mixtures of colloids and polymers were filtered with Cameo Nylon filters of pore size $5.0\,\mu$m. Transparent solutions were filled into cylindrical glass cells (Hellma, Müllheim, Germany) of 10 and 20 mm diameter. Mixtures which become turbid right after mixing, were filled into 5 mm NMR tubes (VWR, Darmstadt, Germany). All samples where sealed with Teflon tape.

Colloidal particle size and polymer radius of gyration

The size of the silica sphere was determined from the measured diffusion coefficient for various colloid concentrations at $T = 295\,\mathrm{K}$, and a salt concentration of $c_\mathrm{s} = 0.15\,\mathrm{mol/l}$. To illustrate this size determination, consider a dispersion of Ludox particles of volume fraction $\phi = 0.01$. For each scattering angle θ, the hardware records the scattered intensity $I(t)$ over a period of time. Simultaneously, the hardware correlator calculates the normalised intensity auto-correlation function $g^{(2)}(t) = \langle I(0)I(t)\rangle / \langle I^2(0)\rangle$. The function $g^{(2)}(t)$ is related to the normalised auto-correlation function of the scattered electric field, $g^{(1)}(t) = \langle \vec{E}^*(t)\cdot\vec{E}(0)\rangle / \langle |\vec{E}(0)|^2\rangle$, by the Siegert relation $g^{(2)}(t) = 1 + \left[g^{(1)}(t)\right]^2$ [198]. In Fig. 4.4, the result of such a light scattering experiment is shown. In the left figure, $\left[g^{(1)}(t)\right]^2$ is plotted for various scattering angles θ as indicated. For a

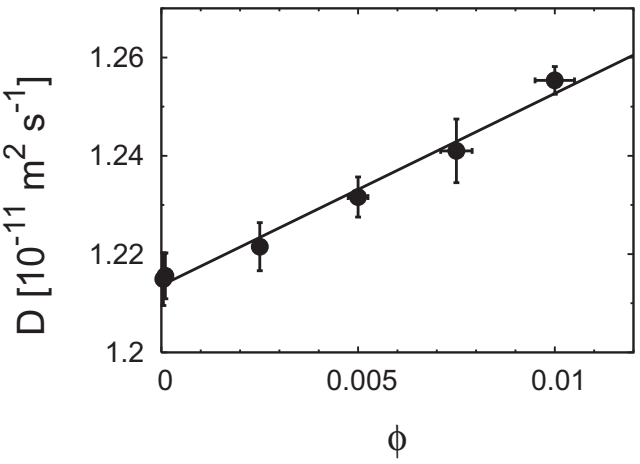

Figure 4.5: Measured collective diffusion coefficient, D, obtained by dynamic light scattering as a function of the silica particle volume fraction, ϕ, for salt concentration $c_\mathrm{s} = 0.15\,\mathrm{mol/l}$.

dilute suspension of monodisperse spherical particles that are uncorrelated, the normalised field auto-correlation function decays single exponentially according to $g^{(1)}(t) = f_c \exp\left[-(t/\tau)\right]$, where $f_c < 1$ describes the coherence area factor limited by the applied optics. Only if one were able to focus the detector onto a single speckle, $f_c = 1$ could be achieved. To date, values of $f_c \approx 0.95$ are reached using single mode fibre optics. The relaxation time, τ, of density fluctuations of wavelength $2\pi/q$ is related for a very dilute sample to the single particle diffusion coefficient, D_0, according to $1/\tau = D_0 q^2$, where $q = (4\pi n/\lambda)\sin(\theta/2)$ is the scattering wave number for light of vacuum wavelength λ in a medium of refractive index n. Thus by fitting a single exponential function to the measured correlation function, as depicted in Fig. 4.4, D_0 is obtained. In practice, however, colloidal particles are not ideally monodisperse and a superposition of exponentials is measured. For simplicity, we globally describe it by a stretched exponential, namely the Kohlrausch-William-Watts (KWW) expression, $g^{(1)}(t) = f_c \exp\left[-(t/\tau)^{\beta_\mathrm{KWW}}\right]$, with a stretching exponent β_KWW, that characterises the overall size polydispersity [199]. For $\beta_\mathrm{KWW} > 0.9$, the polydispersity becomes negligible. The mean relaxation time on a polydisperse sample is then given by $\langle\tau\rangle_\mathrm{KWW} = (\tau/\beta_\mathrm{KWW})\Gamma(1/\beta_\mathrm{KWW})$, where Γ denotes the Gamma-function. In the right figure in Fig. 4.4, the average relaxation time is plotted as a function of q^2. From the slope of its line fit, D_0 is deduced. The so-obtained value of D_0 can be related to the hydrodynamic radius, R_0, of the particles using the Stokes-Einstein relation $D_0 = (k_\mathrm{B}T)/\,(6\pi\eta R_0)$, including the solvent shear viscosity η. The viscosity of the solvent (water) at $T = 295.15\,\mathrm{K}$, taken from the literature, is $\eta = 0.959\,\mathrm{mPa}\cdot\mathrm{s}$ [200].

In Fig. 4.5, the measured collective diffusion coefficient for samples of varying

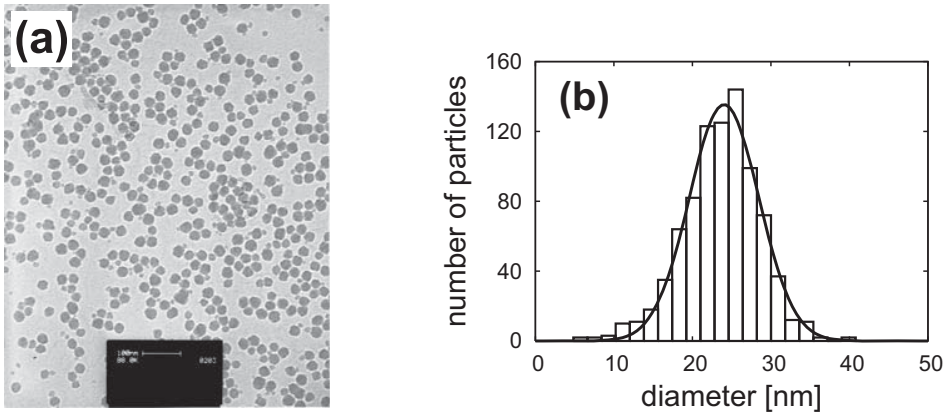

Figure 4.6: Left (a): TEM picture of the dried Ludox particles dispersion. Right (b): Size distribution of Ludox particles observed from image analysis. The mean particle radius is $\langle a \rangle = (12 \pm 2)\,\mathrm{nm}$ (see text for details).

volume fractions is plotted. The line represents a fit to the expression $D(\phi) = D_0(1 + k_\mathrm{d}\phi)$, which describes a low-density expansion of the collective diffusion coefficient, $D(\phi)$, in terms of ϕ applicable for sufficiently large κa [201]. For vanishing ϕ, the single-particle diffusion constant D_0 is recovered. From our fit we find $D_0 = (1.214 \pm 0.001) \times 10^{-11}\,\mathrm{m^2\,s^{-1}}$. Using the Stokes-Einstein relation, we can estimate the hydrodynamic radius of the Ludox silica particles in our DLS measurements as $R_0 = (18.6 \pm 0.1)\,\mathrm{nm}$. The virial coefficient is estimated to be $k_\mathrm{d} = 3.2 \pm 0.2$. Since $k_d = -24\phi \int_0^\infty dx\, x^2(\exp[-\beta u(x)] - 1)$, for $x = r/(2a)$, without hydrodynamic interactions (HI) and since the negative valued HI correction to k_d is quite small for the large salt content considered [202, 203], a positive k_d indicates that the pair potential is practically repulsive. For a monodisperse hard-sphere dispersion, one finds instead that $k_\mathrm{d} = 1.454$ [201].

A Transmission-Electron-Microscope (TEM) picture of Ludox particles is shown in Fig. 4.6. Assuming a Gaussian distribution of the particle diameter d given by $p(d) = p_0 \exp[-(d - \langle d \rangle)^2/(2\sigma^2)]$, with amplitude $p_0 = 135 \pm 4$, mean value $\langle d \rangle = 24\,\mathrm{nm}$ and standard deviation $\sigma = 4.4\,\mathrm{nm}$, the mean colloid radius is $\langle a \rangle = \langle d \rangle/2 = (12 \pm 2)\,\mathrm{nm}$. The z-averaged particle radius is defined as $\langle a \rangle_z = \int_0^\infty da\, p(a)\, a^6 \,/\, (\int_0^\infty da\, p(a)\, a^5)$, resulting in $\langle a \rangle_z = (14 \pm 2)\,\mathrm{nm}$ for our system. This value is slightly smaller than the observed hydrodynamic radius, $R_0 = (18.6 \pm 0.1)\,\mathrm{nm}$, obtained by DLS. We note that the mean radii from TEM and DLS are often quite different [204–207]. The colloidal particles are made of amorphous silica material. Hence, the particles can shrink when drying the suspension in order to make a TEM picture. In addition, our measurements might be influenced to a small extent by electrokinetic effects. However, κa in our measurements is typically much larger than 1, and thus electrokinetic effects are quite small. In the following, we use the value observed from TEM in all our model calculations. Note that for simplicity we will denote the mean colloidal sphere

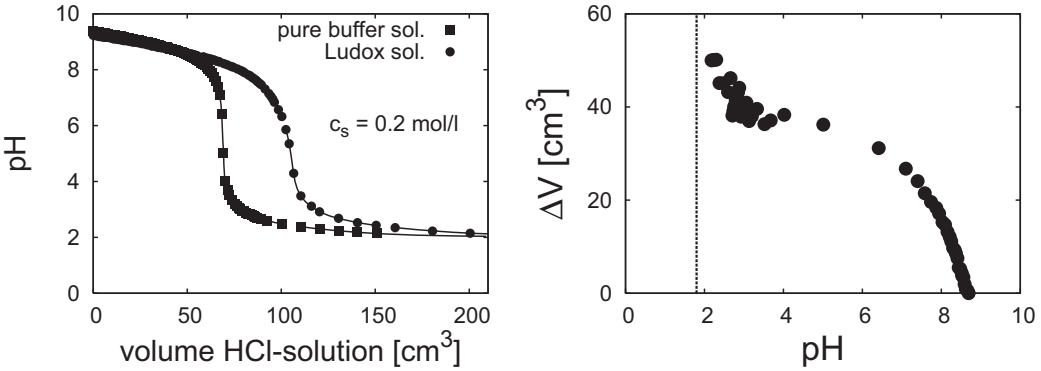

Figure 4.7: Left: Titration curve of the pure buffer solution without salt ($c_s = 0\,\mathrm{mol/l}$) (●), and of the colloid dispersion containing silica particles dissolved in the same buffer solution (■). Right: Difference, ΔV, between the volume of hydrogen chloride solution (0.01 mol/l) added to the colloid solution and the pure buffer solution as a function of the pH-value. The vertical dashed line marks the pH-value of the hydrogen chloride solution.

radius $\langle a \rangle$ as a in the following. Furthermore, we define the polymer-to-colloid size ratio as $q = R_\mathrm{g}/a$. Accordingly, for $M_\mathrm{w} = 4 \times 10^4\,\mathrm{g/mol}$, $5 \times 10^5\,\mathrm{g/mol}$, and $2 \times 10^6\,\mathrm{g/mol}$, we obtain $q = 0.49 \pm 0.03$, 1.4 ± 0.1, and 2.6 ± 0.2, respectively.

Initially after the sample preparation, an angular-dependent DLS measurement was done for each sample. The so-obtained diffusion coefficient, $D(t = 0)$, was then used to normalise the subsequent time-dependent DLS measurements, made at a fixed scattering angle of $\theta = 60°$.

Charge titration

The number of surface charges on the silica particles was estimated by charge titration. For this purpose, a 0.01 mol/l hydrogen chloride (HCl) solution was added stepwise to the colloidal dispersion of known volume fraction, and known salt and buffer concentrations. During addition, the pH value was monitored as a function of the added volume of HCl solution. The procedure was then repeated for the buffer solution at the same salt concentration but without Ludox (see Fig. 4.7, left). The number of titration charges, Z_titr, follows then from the difference of HCl solution additionally added to saturate the hydroxyl-groups on the silica surface (see Fig. 4.7 right and Fig. 4.8). A MATLAB (Math Works Inc., USA) routine was encoded to evaluate the measurements.

According to Fig. 4.8, Z_titr increases with increasing salt content. If the electrolyte concentration is increased, the Debye screening length decreases. The number of surface charges is caused by the dissociation of silanol groups, according to $\mathrm{SiOH} + \mathrm{H_2O} \rightleftharpoons \mathrm{SiO^-} + \mathrm{H_3^+O}$. In equilibrium, the concentration of hydronium ions and protonated and deprotonated silanol groups are characterised by the dissociation constant in the mass action law. As a consequence of the mass

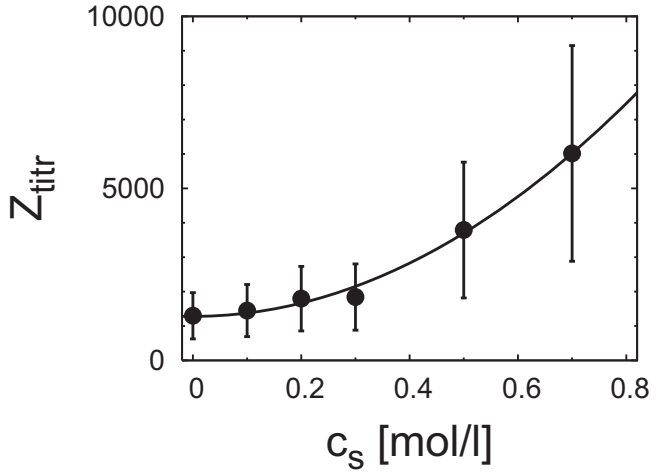

Figure 4.8: Number of titration charges, Z_{titr}, of Ludox silica particles obtained from charge titration as a function of the sodium chloride salt concentration c_{s}. The depicted error bars for Z_{titr} are mainly caused by the uncertainty in a.

action law and the fact that the hydronium concentration near the colloidal surface is affected by the electric surface potential, one obtains in combination with the Poisson-Boltzmann equation that the number of SiO^-, i.e., the number of surface charges, increases with the salt concentration [6, 208]. For later use, we have fitted the data points to the quadratic form $Z_{\mathrm{titr}}(c_{\mathrm{s}}) = a_1 c_{\mathrm{s}}^2 + a_2$, with the two parameters given by $a_1 = (9671 \pm 415)\,\mathrm{l}^2/\mathrm{mol}^2$ and $a_2 = 1280 \pm 95$.

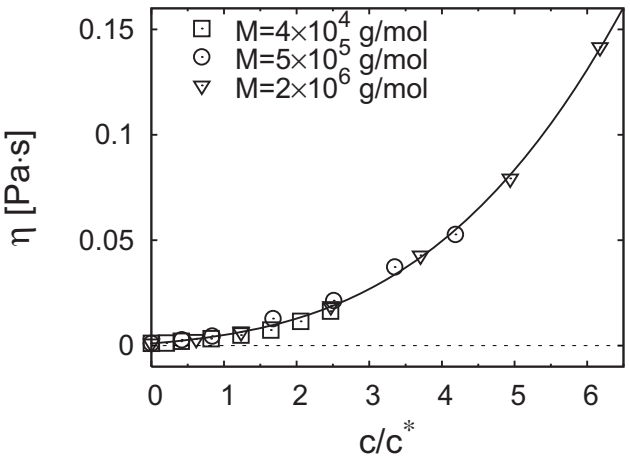

Figure 4.9: Shear viscosity of a pure dextran solution as a function of the reduced volume fraction of polymer coils, $c/c^\star$, for three different molecular weights (see legend) at $T = 295\,\mathrm{K}$. The solid curve is a fit to the experimental data (see text).

Viscosity of the polymer solution

To be able to account for the increase in the intrinsic shear viscosity of the colloidal dispersion with increasing polymer concentration, the shear viscosity, η, of pure Dextran solutions has been measured using an Ares 4LS1 rheometer (TA Instruments, USA) with a Cuette cell of 17 mm inner diameter. The polymer was diluted in the pure buffer solution without salt. In Fig. 4.9, the measured viscosity of the dextran solution is shown as a function of the reduced density of polymer coils for molar masses of $M = 4 \times 10^4\,\mathrm{g/mol}$, $5 \times 10^5\,\mathrm{g/mol}$ and $2 \times 10^6\,\mathrm{g/mol}$, respectively. As expected, η is a function of c/c^* only, independent of the molar mass. The solid curve is a fit to the cubic expansion $\eta(x) = \eta_0(1 + \alpha_1 x + \alpha_2 x^2 + \alpha_3 x^3)$ [209], with $x = c/c^*$, and $\alpha_1 = 3 \pm 1$, $\alpha_2 = 0.7 \pm 0.6$, and $\alpha_3 = 0.43 \pm 0.07$. The solvent viscosity has been taken from literature, $\eta_0(T = 295\,\mathrm{K}) = 0.959 \times 10^{-3}\,\mathrm{Pa \cdot s}$ [200]. The experimentally observed viscosity of the pure buffer solution, $\eta(x = 0) = (1.0 \pm 0.2) \times 10^{-3}\,\mathrm{Pa \cdot s}$, is in agreement with this value. A NaCl concentration of 0.5 mol/l increases the (pure) solvent viscosity only slightly to $(1.1 \pm 0.2) \times 10^{-3}\,\mathrm{Pa \cdot s}$ and, as a consequence, is neglected in the following.

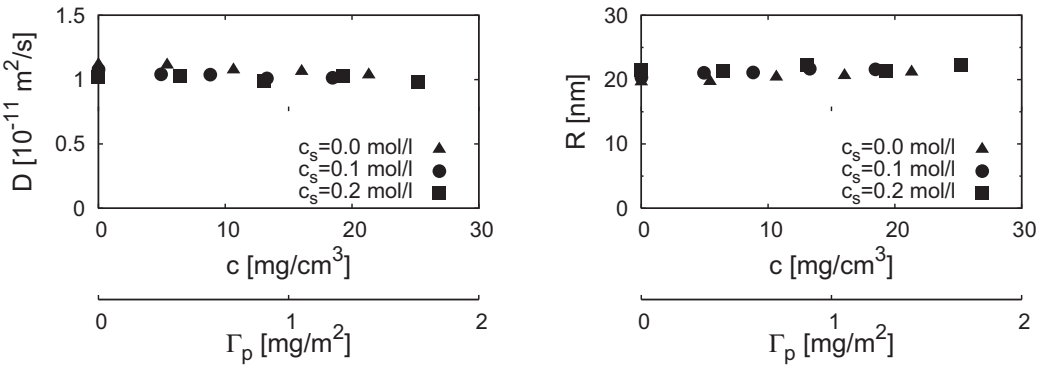

Figure 4.10: Left: Collective diffusion coefficient, D, of a Ludox silica dispersion at $\phi = 5 \times 10^{-3}$ as function of the added dextran concentration, c, ($M_\mathrm{w} = 5 \times 10^5\,\mathrm{g/mol}$) for $p\mathrm{H} = 9.2 \pm 0.1$ and for $c_\mathrm{s} = 0\,\mathrm{mol/l}$, $0.1\,\mathrm{mol/l}$ and $0.2\,\mathrm{mol/l}$, respectively. Right: Hydrodynamic radius, R, obtained from the Stokes-Einstein relation using $\eta_0 = 0.959\,\mathrm{mPa \cdot s}$. The lower scale of the abscissa gives the polymer surface concentration, Γ_p, that would result if all polymers adsorb on the surface of the silica particles. As a rule of thumb, one expects that the surface is completely covered when $\Gamma_p \geq 1\,\mathrm{mg/m^2}$ [210].

Evidence that dextran does not adsorb on the silica-water interface

To investigate whether dextran adsorbs at the silica sphere surfaces, we prepared a dispersion of Ludox and mixed it with dextran solutions of varying concentration. The samples were mixed thoroughly and stored for 24 hours at room temperature to equilibrate before the measurements were conducted. All samples contain the ammonium chloride puffer with $c_b = 0.02\,\mathrm{mol/l}$ and $p\mathrm{H} = 9.2 \pm 0.1$. The volume fraction of Ludox was fixed to $\phi = 0.005$. Figure 4.10 displays DLS measurements on these Ludox-dextran mixtures at varying salt concentrations. As shown, the collective diffusion coefficient, D, and, likewise, the hydrodynamic radius, R, are not affected upon increasing the polymer concentration. In contrast, one expects a significant decrease of D, and conversely, an increase in R in case of adsorbing polymers due to an enlarged hydrodynamic friction caused by the adhering chains. Thus, we can conclude that dextran does not adsorb onto the surface of the Ludox particles at $p\mathrm{H} = 9.2 \pm 0.1$, in accordance with previous findings [211–213].

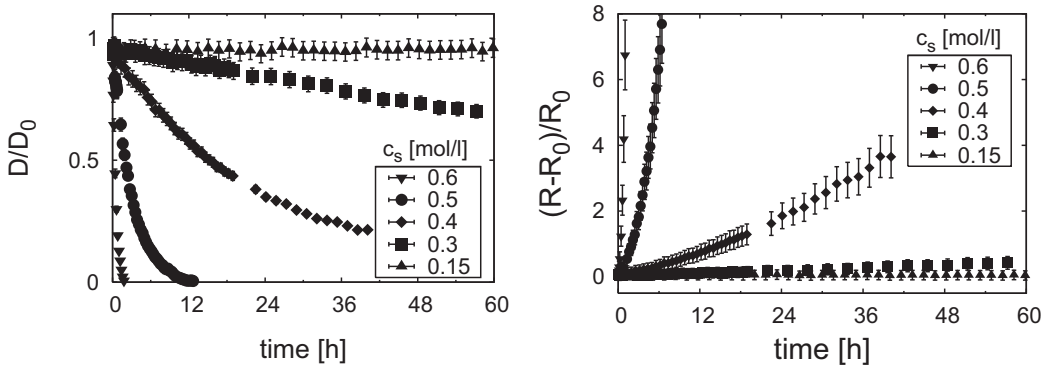

Figure 4.11: Left: Normalised measured collective diffusion coefficient as a function of the elapsed time after sample preparation, for varying c_s (see legend) and $\phi = 0.01$. Right: Reduced hydrodynamic radius as a function of the elapsed time after sample preparation, calculated from the diffusion coefficient in the left figure using the Stokes-Einstein relation.

4.3 Cluster-aggregation in pure silica dispersions

In this section, we first explore aqueous suspensions of fused silica particles without added polymers, which have been under considerably investigation in the past [170, 214–218]. However, earlier studies used slightly different colloidal batches than ours in terms of the particle size and densities, and slightly different solvent conditions. Thus, a direct quantitative comparison of these earlier data with our present measurements is not possible. Our light scattering data on the pure silica-water system discussed in the following serve as the basis to study the additional influence of added polymers on the cluster aggregation rate.

4.3.1 Influence of the electrolyte concentration on the aggregation rate

In the left figure of Fig. 4.11, the collective diffusion coefficient of silica spheres in a Ludox dispersion at $\phi = 0.01$ and $p\mathrm{H} = 9.2$, is measured over several hours for various salt concentrations. The diffusion coefficient has been normalised by the single particle diffusion coefficient, D_0. In the right figure, the corresponding hydrodynamic radius obtained from the Stokes-Einstein relation is shown. As can be clearly seen, the time evolution of the diffusion coefficient depends strongly on c_s. With increasing c_s, the diffusion coefficient decays faster to zero, indicative of a more quickly growing cluster size of aggregates (see the right figure of Fig. 4.11). This observation is explained by the salt-induced screening of the colloid charges. The electrostatic repulsion decreases with increasing c_s, according to Eq. (4.2), so that the particles can overcome the reduced Coulomb barrier more easily during a collision event (see Fig. 4.2), leading to the formation of dimers, trimers and so on. With growing reaction time, increasingly larger aggregates are observed, which

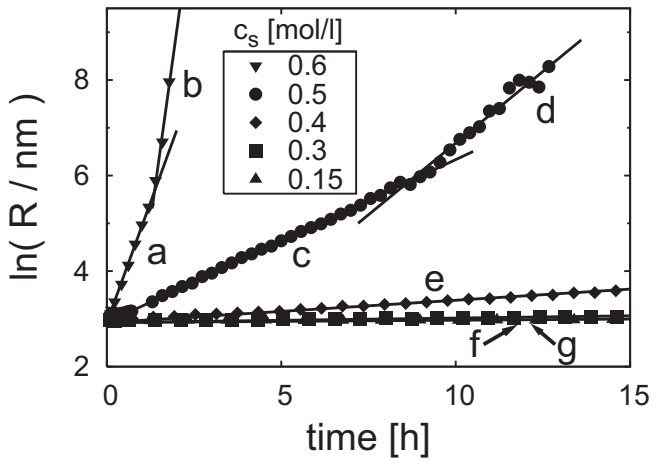

Figure 4.12: Semi-logarithmic plot of the reduced time-dependent hydrodynamic radius of colloid clusters measured for several salt concentrations as a function of time for $\phi = 0.01$. The straight lines are fits to the form $R(t) = R_0 \exp(t/\tau_a)$, with the adjustable time parameter τ_a determined for lines a, b, c, d, e, f and g. $c_s = 0.6\,\mathrm{mol/l}$ (▼): (a) $\tau_a = (0.498 \pm 0.003)\,\mathrm{h}$, (b) $\tau_a = (0.19 \pm 0.02)\,\mathrm{h}$; $c_s = 0.5\,\mathrm{mol/l}$ (●): (c) $\tau_a = (2.93 \pm 0.01)\,\mathrm{h}$, (d) $\tau_a = (1.67 \pm 0.07)\,\mathrm{h}$; $c_s = 0.4\,\mathrm{mol/l}$ (♦): (e) $\tau_a = (23.8 \pm 0.1)\,\mathrm{h}$; $c_s = 0.3\,\mathrm{mol/l}$ (■): (f) $\tau_a = (7.8 \pm 0.1)\,\mathrm{d}$; $c_s = 0.15\,\mathrm{mol/l}$ (▲): (g) $\tau_a = (725 \pm 298)\,\mathrm{d}$, respectively.

consist of several silica particles (monomers). As a consequence, the diffusion coefficient of the aggregates decreases, and likewise, the cluster hydrodynamic radius increases with time.

In Fig. 4.12, the logarithm of the reduced hydrodynamic radius is plotted as a function of the time elapsed after sample preparation. Note that the τ_a for $c_s = 0.15\,\mathrm{mol/l}$ has been monitored by angular-dependent DLS over a period of 16 days. For all salt concentrations considered, a linear relation within the logarithmic-linear plot is observed for initial times. Thus, we conclude that the initial cluster growth is caused by a slow, irreversible reaction-limited aggregation process, where the hydrodynamic radius scales with $\exp(t/\tau_a)$ in time. For $c_s = 0.5\,\mathrm{mol/l}$ and $0.6\,\mathrm{mol/l}$, a second and faster exponential cluster growth regime is observed at later times. This regime can be attributed to a faster irreversible reaction-limited cluster aggregation mechanism, which sets in after the clusters have consumed the monomers in their surroundings. Accordingly, further growth of clusters by capturing monomers is prevented. Instead, bigger aggregates are formed at larger time scales due to cluster-cluster collision.

The short-time aggregation time, τ_a, obtained from the linear fit to the short-time data points in Fig. 4.12, is shown in Fig. 4.13 as a function of c_s. As expected, τ_a increases with decreasing c_s, because of the increasing Coulomb barrier.

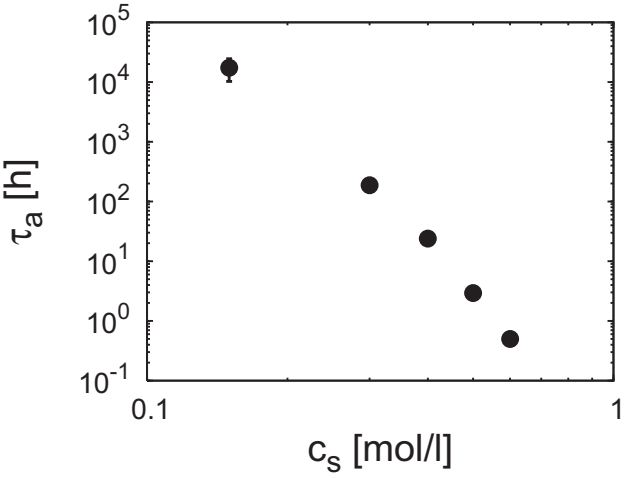

Figure 4.13: Short-time aggregation time, τ_a, as a function of salt concentration c_s, for $\phi = 0.01$.

4.3.2 DLVO-like description of the aggregation kinetics

Having carefully characterised our system in terms of colloid size, titration charge at $p\mathrm{H} = 9.2$, and Hamaker constant $A_\mathrm{H} = 0.8 \times 10^{-20}\mathrm{J}$ [175], we are now in the position to calculate the DLVO pair potential consisting of the van der Waals interaction part, $u_\mathrm{vdW}(r)$, in Eq. (4.1), and the electrostatic pair potential part $u_\mathrm{el}(r)$ in Eq. (4.2).

The pair potential $u_\mathrm{DLVO}(r)$ obtained using the titration charges in $u_\mathrm{el}(r)$ (see Fig. 4.14), is practically purely repulsive for all salt concentrations considered, and does not exhibit a sufficiently small Coulomb barrier that can be overcome by thermal motion. Thus, irreversible cluster-aggregation caused by the primary van der Waals minimum would be entirely inhibited by the strong electrostatic repulsion caused by Z_titr. In contrast to this, we observe experimentally a rapid cluster-growth with increasing c_s. Note here that for $c_s > 0.15\,\mathrm{mol/l}$, a secondary minimum in $u_\mathrm{DLVO}(r)$ appears in Fig. 4.14. However, this weak secondary minimum ($\ll 1\,k_\mathrm{B}T$) is to shallow to cause reversible aggregation. The reason for the difference between the experimental results and the theoretical predictions is that the titration charge, which is an estimate of the bare particle charge, can not be used in the effective potential $u_\mathrm{el}(r)$. For values $l_\mathrm{B}\,|Z|\,/a \gtrsim 1$, the linear Debye-Hückel (DH) theory assumption leading to Eq. (4.2) is not valid any more. In fact, in our Ludox dispersions, $l_B|Z|/a > 50$ for all c_s considered. For larger charges, the DH form of $u_\mathrm{el}(r)$ can still be used, but Z (and also κ) must be replaced by an effective (renormalised) charge number Z_eff, and a renormalised κ, that incorporate the effect of quasi-counterion condensation near strongly charged colloid surfaces. Due to this quasi-counterion condensation, Z_eff can be substantially smaller than the bare charge at lower salinity. Several approximative schemes, mainly based on the Poisson-Boltzmann approach and

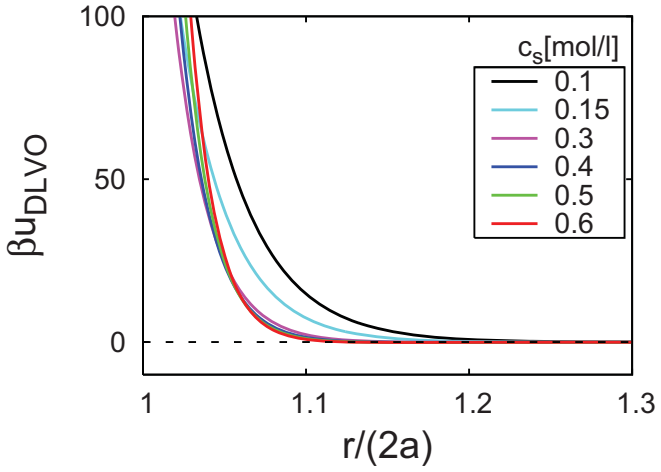

Figure 4.14: DLVO pair potential for the pure Ludox silica dispersion considered in Fig. 4.11, with $\phi = 0.01$ and various c_s-values at $p\mathrm{H} = 9.2$ and $T = 295\,\mathrm{K}$ as indicated. The electrostatic part of the DLVO potential has been calculated here using the colloidal charge number, Z_{titr}, found from titration measurements (see Fig. 4.8). The Hamaker constant in the vdW attraction part is $A_{\mathrm{H}} = 0.8 \times 10^{-20}\mathrm{J}$, for the fused silica particles dissolved in water [175].

additional cell model or jellium model assumptions have been devised to compute $Z_{\mathrm{eff}}(c_s)$ and κ for a given Z, ϕ and c_s [219–221]. We point out that $Z_{\mathrm{eff}}(c_s)$ is determined from matching the calculated τ_a to the experimental one for a single small $\phi = 0.01$. Then $Z_{\mathrm{eff}}(c_s)$ is kept constant when ϕ is changed. Which method of charge renormalisation gives the most reliable result for Z_{eff} is still a matter of debate. Similar problems in experimental studies on dispersions of highly charged silica particles of nanometric size, where the Debye-Hückel approximation is not quantitatively correct, have been encountered before [222].

We note further that the particle distance, where the maximum in $u_{\mathrm{DLVO}}(r)$ occurs, is in the sub-nanometre range for the small and highly charged Ludox particles and for the high salt concentrations considered. Thus, in addition, the continuum description of the solvent used in the mean-field Poisson-Boltzmann theory is not fully justifiable any more, and the discrete nature of the microions and the solvent molecules may play a role. Also, the van der Waals attraction may not be quantitatively describable any more by Eq. (4.1). Furthermore, the particle surface roughness [223, 224], effects of an inhomogeneous surface charge distribution [225, 226], and hydration forces [227, 228] should also be considered in principle. Such a quantitative model description of the experimental system would be extremely demanding and has not been accomplished to date.

Since our present work mainly concentrates on the influence of polymer-induced attraction on the non-equilibrium and equilibrium phase behaviour of charged colloidal dispersion, we are not concerned here with a first-principle theoretical description. Rather, we will restrict ourselves to a DLVO-like description and

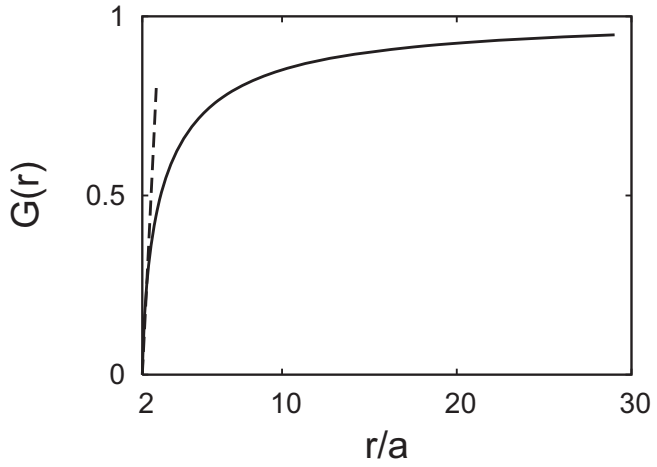

Figure 4.15: Mobility of the relative motion of two spheres along their line of centres [229]. The dashed line indicates the linear lubrication regime, where $G(r) \sim (r-2a)/a$.

consider Z ($= Z_{\text{eff}}$) in $u_{\text{el}}(r)$ as an adjustable parameter, with renormalised $\kappa^2 = 4\pi l_{\text{B}}\ (|Z_{\text{eff}}|\rho_{\text{c}} + 2\rho_{\text{s}} + \rho_{\text{b}})$ for a 1-1 electrolyte in accord with the renormalised jellium model theory of charge renormalisation [220]. The van der Waals forces are approximated by Eq. (4.1) using a Hamaker constant of $A_{\text{H}} = 0.8 \times 10^{-20}\text{J}$ as given in the recent literature [175]. We compare the aggregation time, τ_a, deduced from our experiments with the dimer formation theory of Brownian flocculation [6, 178], where τ_a is given by

$$\tau_a = \frac{\pi\eta\, a^3}{\phi\, k_{\text{B}}T}\, W\,, \tag{4.7}$$

and W is the stability ratio, obtained from

$$W = 2a \int_{2a}^{\infty} \frac{\exp\left(\beta u(r)\right)}{r^2 G(r)}\, dr\,. \tag{4.8}$$

The derivation of Eqs. (4.7) and (4.8) are summarised in the appendix A. The hydrodynamic function $G(r)$ in Eq. (4.8) quantifies the relative mobility of two spheres along their line of centres [230]. The tabulated values for that hydrodynamic function is shown in Fig. 4.15. If two spherical particles approach one another, the liquid in the gap between the two colloids has to be squeezed out. For $r \to 2a$, the pressure in the liquid gap diverges as $\eta V a/(r-2a)^2$ [231], and $G(r)$ decays to zero as $(r-2a)/a$. The two-sphere hydrodynamics described by $G(r)$ leads thus to an increase in τ_a. We note that aggregation is possible because the flux due to the inter-particle forces, and thus, W, remains finite, since the diverging vdW attraction overcomes the vanishing mobility.

For $u(r) = 0$ and $G(r) = 1$, i.e., if the pair interaction potential only acts to stick particles together at contact, and if the hydrodynamics interactions are

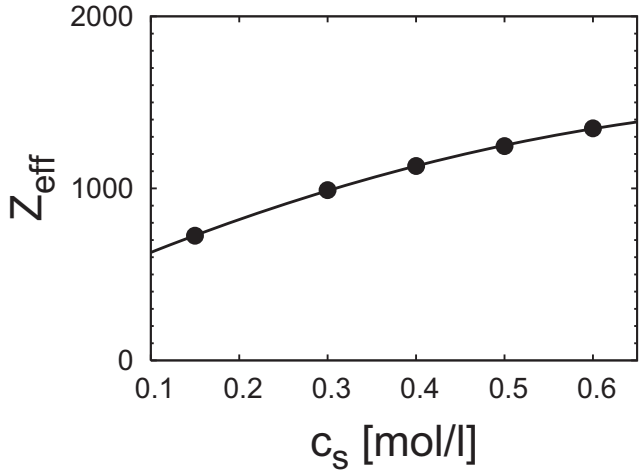

Figure 4.16: Effective colloid charge as a function of the salt concentration, obtained from matching Eq. (4.7) to the experimentally determined initial aggregation time τ_a given in Fig. 4.13. The solid curve is a fit to the form $Z_{\rm eff}(c_s) = b_1 c_s^2 + b_2 c_s + b_3$ with $b_1 = (-1184 \pm 90)\,\mathrm{l}^2/\mathrm{mol}^2$, $b_2 = (2267 \pm 68)\,\mathrm{l/mol}$ and $b_3 = 413 \pm 12$.

neglected, an aggregation time of $\tau_a(Z_{\rm eff}) = 0.13\,\mathrm{ms}$ is obtained for $\phi = 0.01$, and $\tau_a(Z_{\rm eff}) = 0.01\,\mathrm{ms}$ for $\phi = 0.12$, on assuming $a = 12\,\mathrm{nm}$, $\eta = \eta_0$ and $T = 295\,\mathrm{K}$. By substituting $u(r) \equiv u_{\rm DLVO}(r)$ in Eq. (4.8), using $A_{\rm H} = 0.8 \times 10^{-20}\mathrm{J}$ [175], τ_a is estimated by the dimer formation theory in terms of the solutions properties if, in addition, the number of charges is provided. Here, we determine $Z_{\rm eff}$ by matching the τ_a in Eq. (4.7) to the experimental values. Since the major contribution to the integral in Eq. (4.8) comes from the vicinity of the maximum in $u(r)$, we can introduce a lower cutoff radius $a \to a + \epsilon$. Values of ϵ in between 0.1 nm and 0.2 nm have been employed [6]. However, in the present systems of highly screened colloid particles of nanometre size, the location of the maximum in $u_{\rm DLVO}(r)$ is at sub-nanometre distances [222]. Hence, we can select for $a + \epsilon$ the radial distance r_0, where $u_{\rm DLVO}(r)$ crosses zero near contact distance. The so-obtained effective charge number, $Z_{\rm eff}$, is plotted in Fig. 4.16 as a function of c_s. In Fig. 4.17, the corresponding pair potentials are presented.

We point out that, as expected, $Z_{\rm eff} < Z_{\rm titr}$ for all c_s considered. The increase of $Z_{\rm eff}$ with increasing c_s is consistent with the lowering of quasi-counterion condensation due to enlarged screening [220]. Table 4.1 contains the numerical values characterising the pair potential. The location of the maximum (Coulomb barrier), $r_{\rm max}$, and the secondary minimum, $r_{\rm min}$, in $\beta u_{\rm DLVO}$ range from $r_{\rm max}/(2a) = 1.007$ to $r_{\rm max}/(2a) = 1.006$, and from $r_{\rm min}/(2a) = 1.26$ to $r_{\rm min}/(2a) = 1.10$, respectively, when c_s increases from 0.15 mol/l to 0.6 mol/l. At the same time, the pair potential at $r_{\rm max}$, $\beta u_{\rm DLVO}(r_{\rm max})$, decreases from 35 to 25, and the depth of the secondary minimum, $\beta u_{\rm DLVO}(x_{\rm min})$, increases from -0.04 to -0.24. Note that the centre-to-centre distance, r_0, where $u_{\rm DLVO}$ intersects with

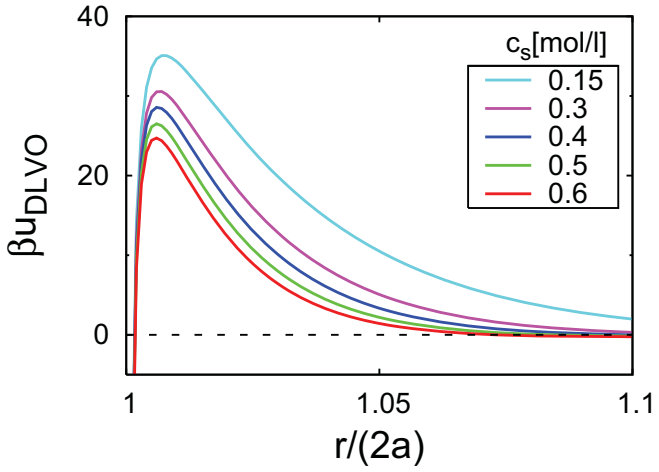

Figure 4.17: DLVO pair potential calculated for parameters obtained from adjusting the effective colloid charge number $Z_{\text{eff}}(c_s)$ entering the calculation of τ_a to the experimentally found initial aggregation time, for a system with $\phi = 0.01$ at $T = 295\,\text{K}$ (see Table 4.1).

the x-axis at near-contact distance, is almost unaffected by the change in the salinity, and is given by $r_0 = 1.002$, whereas the Coulomb barrier height Q is strongly affected. Table 4.1 illustrates how sensitively τ_a depends on the salinity. By increasing c_s from 0.15 mol/l to 0.6 mol/l, τ_a is reduced from several weeks down to only half an hour.

c_s [mol/l]	Z_{eff}	$1/(\kappa\sigma)$	$\beta\epsilon$	Q	τ_a [h]
0.15	725	0.032	56.9	35.1	17408
0.3	990	0.023	55.9	30.7	186
0.4	1130	0.020	55.6	28.7	24
0.5	1246	0.018	54.6	26.7	2.9
0.6	1349	0.016	53.8	25.0	0.5

Table 4.1: Effective charge number and other parameters characterising $u_{\text{DLVO}}(r)$ for several experimentally used salt concentrations. The effective charge number Z_{eff} has been adjusted to match the experimental values of τ_a as described in the text. The Hamaker constant used for the fused silica is $A_{\text{H}} = 0.8 \times 10^{-20}\text{J}$ [175].

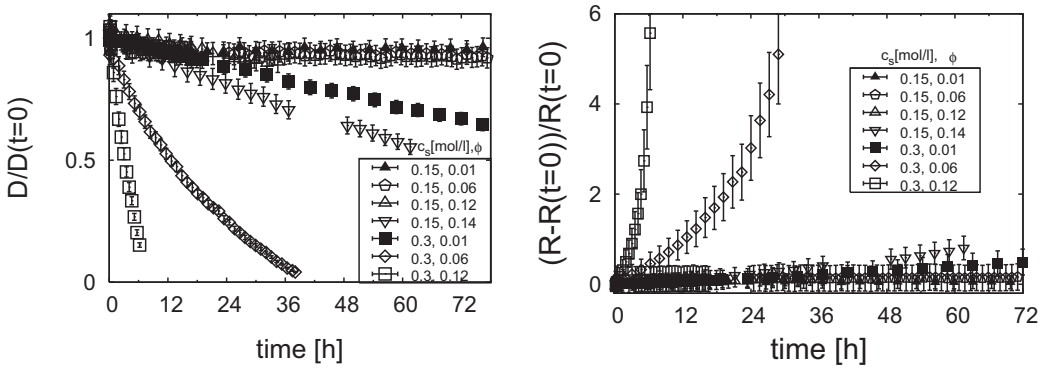

Figure 4.18: Left: Influence of the colloid volume fraction (see legend) on the measured diffusion constant as a function of the elapsed time after sample preparation, for $c_\mathrm{s} = 0.15\,\mathrm{mol/l}$ and $c_\mathrm{s} = 0.3\,\mathrm{mol/l}$. Right: Corresponding reduced apparent hydrodynamic radius calculated using the Stokes-Einstein relation.

4.3.3 Influence of the colloid volume fraction on the aggregation rate

We investigate now the influence of the colloid volume fraction varied in the range from 0.01 to 0.14, for two salt concentrations $c_s = 0.15\,\mathrm{mol/l}$ and $0.3\,\mathrm{mol/l}$. The time-evolution of the collective diffusion coefficient D and the hydrodynamic radius of the growing clusters is shown in Fig. 4.18. The diffusion coefficient increases with increasing ϕ and decreasing c_s, as observed also in equilibrium suspensions of charge-stabilised particles [201]. Hence, the obtained values $D(t = 0) = (1.258 \pm 0.005) \times 10^{-11}\,\mathrm{m^2\,s^{-1}}$ at $c_s = 0.3\,\mathrm{mol/l}$ and $\phi = 0.12$, and $D(t = 0) = (1.434 \pm 0.002) \times 10^{-11}\,\mathrm{m^2\,s^{-1}}$ at $c_s = 0.15\,\mathrm{mol/l}$ and $\phi = 0.12$, are larger than the single-particle diffusion coefficient $D_0 = (1.214 \pm 0.001) \times 10^{-11}\,\mathrm{m^2\,s^{-1}}$. Note that $D(t)$ in Fig. 4.18 is normalised by its value measured directly after sample preparation, $D(t = 0)$, and accordingly, the increment $R(t) - R(t = 0)$ is normalised by $R(t = 0)$. The cluster growth is thus enhanced with increasing ϕ and increasing c_s. The influence of ϕ follows from the fact that the collision probability increases as ϕ^2. When plotting the logarithm of the normalised hydrodynamic radius as a function of time (see Fig. 4.19), a linear relation is observed for short times after sample preparation, indicating a slow reaction-limited aggregation mechanism. However, for $c_s = 0.3\,\mathrm{mol/l}$ and $\phi \geq 0.06$, we observe a non-exponential cluster growth rate at later times. This non-exponential behaviour can be explained by the gelation of the sample, which manifests itself in a power-law-dependent growth rate [232]. In accordance with the observed accelerated growth rate with increasing ϕ, the aggregation time, obtained from the fits to the data points in Fig. 4.19, increases with increasing $1/\phi$ (see Fig. 4.20). Also shown in Fig. 4.20 are the theoretically predicted aggregation times calculated from Eq. 4.7 using $u_\mathrm{DLVO}(r)$ (Eq. 4.3) and Z_eff (see Fig. 4.17). The dimer formation theory for the

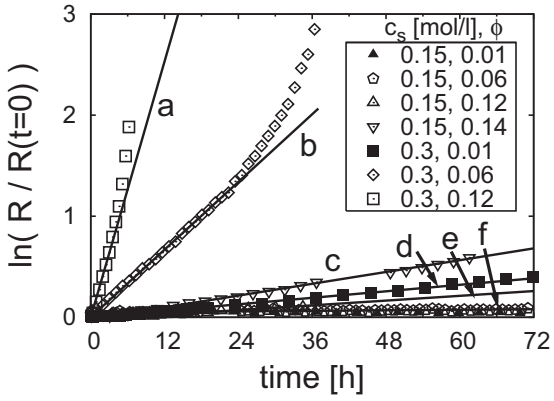

Figure 4.19: Semi-logarithmic plot of the hydrodynamic radius of aggregated colloidal clusters as a function of the elapsed time. The straight lines (a-g) are fits to the form $R(t) = R(t=0)\exp(t/\tau_a)$, with the parameters τ_a and $R(t=0)$ determined right after the sample preparation. The data for $\phi = 0.01$, and $c_s = 0.15\,\mathrm{mol/l}$ and $c_s = 0.3\,\mathrm{mol/l}$ are replotted for comparison from Fig. 4.12. $c_s = 0.15\,\mathrm{mol/l}$: (▲, g) $\phi = 0.01$, $\tau_a = (725 \pm 298)\,\mathrm{d}$; (⬠, f) $\phi = 0.06$, $\tau_a = (94 \pm 9)\,\mathrm{d}$; (△, e) $\phi = 0.12$, $\tau_a = (10.6 \pm 0.2)\,\mathrm{d}$; (▽, c) $\phi = 0.14$, $\tau_a = (4.29 \pm 0.02)\,\mathrm{d}$; $c_s = 0.3\,\mathrm{mol/l}$: (■, d) $\phi = 0.01$, $\tau_a = (7.8 \pm 0.1)\,\mathrm{d}$; (◇, b) $\phi = 0.06$, $\tau_a = (17.9 \pm 0.1)\,\mathrm{h}$; (□, a) $\phi = 0.12$, $\tau_a = (4.7 \pm 0.2)\,\mathrm{h}$.

initial stage of Brownian flocculation describes the experimental data surprisingly well for $\phi \leq 0.14$. In concentrated colloidal suspensions, we expect an accelerated aggregation rate due to correlation effects as found by Sauer and Löwen [233] using computer simulations. In addition, effects on the screening ability of the microions and the additional screening by the intervening macroions have to be accounted for with increasing colloid concentration [51, 234].

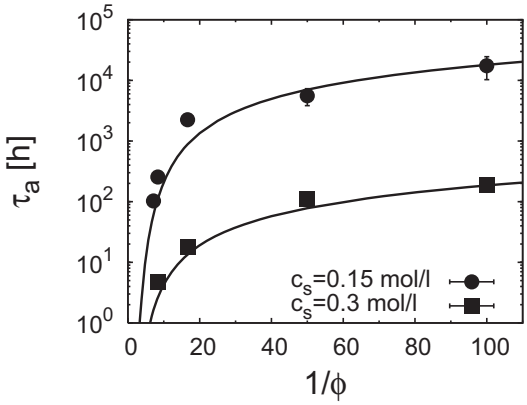

Figure 4.20: Aggregation time, τ_a, as a function of the inverse colloid volume fraction for $c_s = 0.15\,\mathrm{mol/l}$ (•) and $c_s = 0.3\,\mathrm{mol/l}$ (■). The solid curves describe the theoretically predicted aggregation times calculated from Eq. 4.7, using $u_{\mathrm{DLVO}}(r)$ in Eq. (4.3) with Z_{eff} (see also Fig. 4.17).

4.4 Depletion-driven cluster-aggregation

4.4.1 Description of polymer-induced cluster aggregation

In the following, we analyse the influence of the depletion agent dextran on the aggregation kinetics. We account for the influence of added non-adsorbing polymers on the aggregation behaviour of the silica dispersion, by the AOV effective pair potential, $u_{\mathrm{AOV}}(r)$, in Eq. (4.6). We explore polymer-to-colloid size ratios in the range $0.49 \leq q \leq 2.6$. The total colloid pair potential, $u(r)$, which enters into the calculation of the aggregation time, through Eqs. (4.7) and (4.8), consists then of the hard sphere contribution, $u_{\mathrm{hs}}(r)$, the van der Waals attraction part, $u_{\mathrm{vdW}}(r)$, the screened electrostatic repulsive part, $u_{\mathrm{el}}(r)$, and the polymer-depletion induced attractive part, $u_{\mathrm{AOV}}(r)$, so that

$$u(r) = u_{\mathrm{hs}}(r) + u_{\mathrm{vdW}}(r) + u_{\mathrm{el}}(r) + u_{\mathrm{AOV}}(r)\,. \tag{4.9}$$

Using this $u(r)$, the evaluation of W in Eq. (4.8) proceeds as explained in subsection 4.3.2. The AO model assumes that the polymers can freely overlap, and describes them as phantom hard spheres of radius R_g. Hence, the AO model can be expected to apply to infinitely diluted polymer solutions at θ-solvent conditions, for $q \leq 1$ (see, [104], and chapter 3). In fact, dextran is close to its θ temperature value at $T = 295\,\mathrm{K}$ [162]. On considering further that we are mainly interested in polymer concentrations below the overlap concentration c^*, we use the AOV depletion potential throughout to predict τ_a theoretically. Effects arising from non-ideal polymer solution properties, which are expected to become important for semi-dilute polymer concentrations, could be incorporated into the description of the depletion-driven colloidal aggregation kinetics in an additional step. However, this will be left to future work.

4.4.2 Influence of non-adsorbing polymer chains

When adding dextran of a molar mass $M = 5 \times 10^5\mathrm{g/mol}$ ($q = 1.4 \pm 0.1$) to a charge-stabilised Ludox silica dispersion with $\phi = 0.01$, $c_s = 0.15\,\mathrm{mol/l}$, $p\mathrm{H} = 9.2 \pm 0.1$ and $T = 295\,\mathrm{K}$, we do not observe an enhanced creation of clusters even up to $c/c^* = 1.67$, until two days have passed after sample preparation (see, Fig. 4.21). This indicates that, at $c_s = 0.15\,\mathrm{mol/l}$, the polymer-induced depletion attraction cannot compensate enough the Coulomb repulsion. Instead, we observe a strong influence of the polymer concentration on the aggregation behaviour for a larger $c_s = 0.3\,\mathrm{mol/l}$ (see Fig. 4.22). The diffusion coefficient decays faster with increasing c/c^*. Plotting the reduced hydrodynamic radius against time on a logarithmic-linear scale results in a linear relation (see Fig. 4.23). This finding suggests that the addition of non-adsorbing polymers at near-θ solvent conditions does not change the aggregation mechanism. Hence, also in the presence of the polymer chains, the cluster growth is likely be described by the RLA

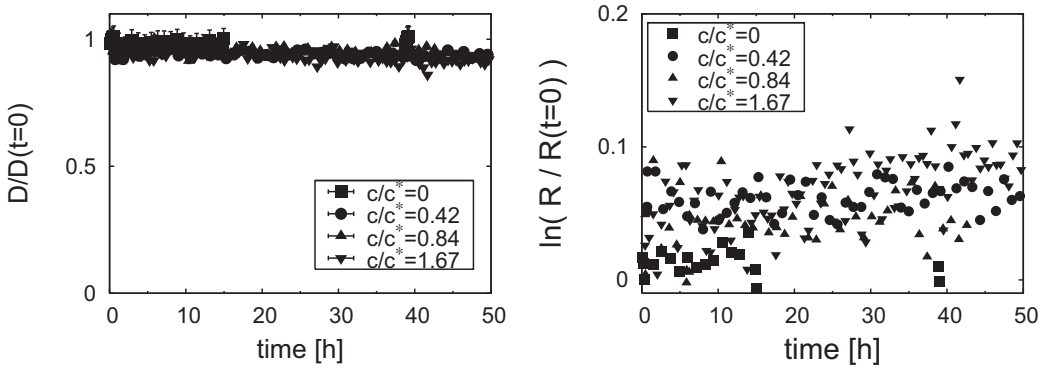

Figure 4.21: Left: Time evolution of the collective diffusion coefficient of Ludox silica particles with varying polymer concentration c, normalised by the overlap concentration c^* (see legend). The colloidal dispersion has been prepared with $\phi = 0.01$ and $c_s = 0.15\,\mathrm{mol/l}$. The polymer molar mass is $M = 5 \times 10^5 \mathrm{g/mol}$, corresponding to $q = 1.4 \pm 0.1$. Right: Logarithmic plot of the reduced hydrodynamic radius increment calculated using the Stokes-Einstein relation.

mechanism. From the slopes of the curves in Fig. 4.22 we extract the characteristic aggregation time depicted in Fig. 4.24. Decreasing values of τ_a with increasing polymer concentration correspond to an accelerated cluster growth rate. The solid curve in Fig. 4.24 gives our theoretical prediction for $\tau_a(c)$ obtained from Eqs. (4.7-4.8), and based on the DLVO pair potential in conjunction with the AO model. As shown in Fig. 4.24, the effect on τ_a due to the polymer chains is overall well described by the AOV model. The aggregation times predicted by the aggregation theory are moderately larger than the experimental values. This

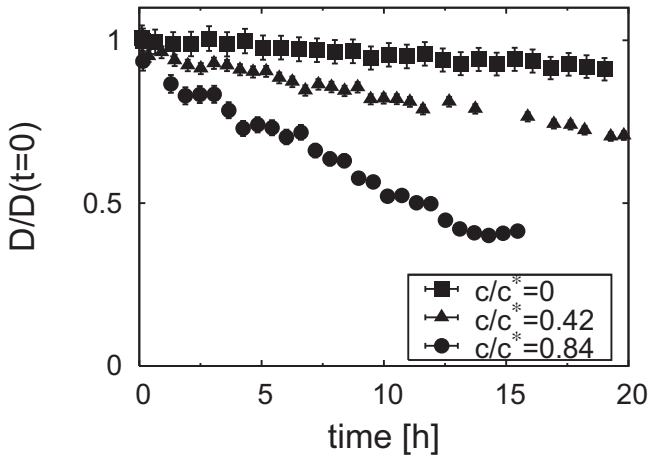

Figure 4.22: Time evolution of the normalised collective diffusion coefficient of Ludox silica particles with varying polymer concentration (see legend) for $\phi = 0.01$, $c_s = 0.3\,\mathrm{mol/l}$, and polymer molar mass $M = 5 \times 10^5 \mathrm{g/mol}$.

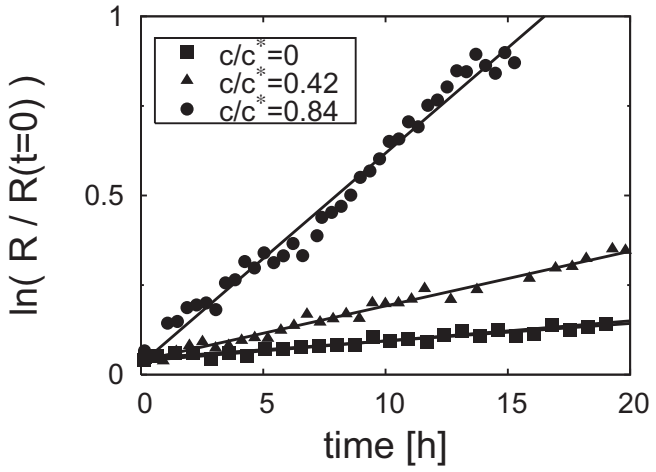

Figure 4.23: Semi-logarithmic plot of the reduced hydrodynamic radius of colloid clusters as a function of elapsed time for a mixture of Ludox silica spheres at $\phi = 0.01$ and dextran at varying concentrations corresponding to $q = 1.4 \pm 0.1$ at $p\mathrm{H} = 9.2 \pm 0.1$, $T = 295\,\mathrm{K}$, and $c_s = 0.3\,\mathrm{mol/l}$. The straight lines are fits to the form $R(t) = R(t = 0)\exp(t/\tau_a)$, with the characteristic time τ_a and the hydrodynamic radius $R(t = 0)$ measured right after sample preparation. The data for $c/c^* = 0$ are replotted from Fig. 4.12 for comparison. $c/c^* = 0$: (■), $\tau_a = (7.8 \pm 0.1)\,\mathrm{d}$; $c/c^* = 0.42$: (▲), $\tau_a = (2.7 \pm 0.1)\,\mathrm{d}$; $c/c^* = 0.84$: (●), $\tau_a = (16.2 \pm 0.1)\,\mathrm{h}$.

discrepancy increases with increasing c/c^*. However, we note that no adjustable parameter has been used for the polymer-induced depletion interactions.

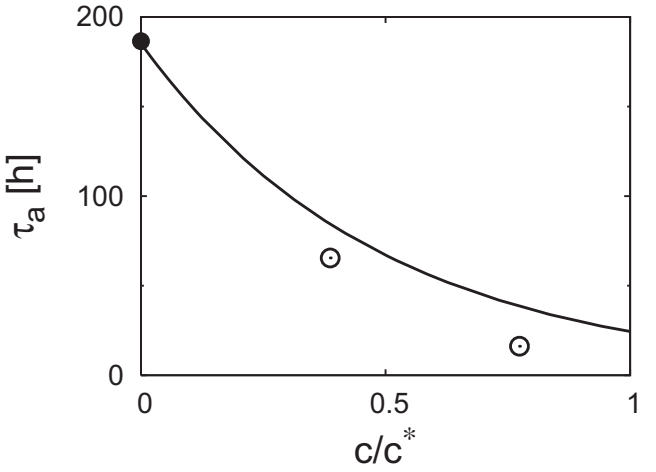

Figure 4.24: Circles: experimentally observed aggregation time as a function of reduced polymer concentration in a mixture of dextran with $M = 5 \times 10^5\mathrm{g/mol}$ and $q = 1.4 \pm 0.1$, and silica particles with $\phi = 0.01$ and $c_s = 0.3\,\mathrm{mol/l}$. The solid curve is the theoretically τ_a obtained using Eq. (4.9) for $u(r)$ and Z_{eff} as explained in subsection 4.4.1.

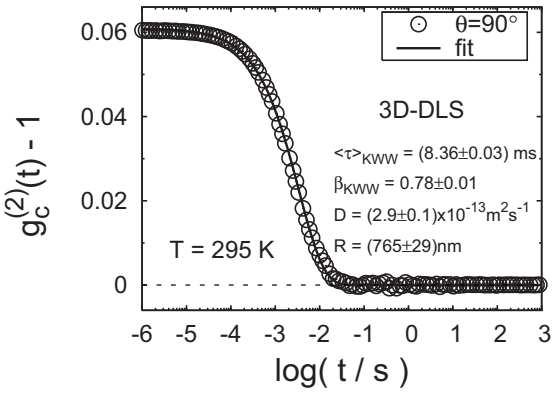

Figure 4.25: Reduced intensity cross correlation function, $g_c^{(2)} - 1$, of a mixture of charge-stabilised Ludox silica particles with $\phi = 0.01$, and dextran with $c/c^* = 0.42$ ($M = 5 \times 10^5$ g/mol), measured using a 3D-DLS setup at $T = 295$ K and $c_s = 0.3$ mol/l.

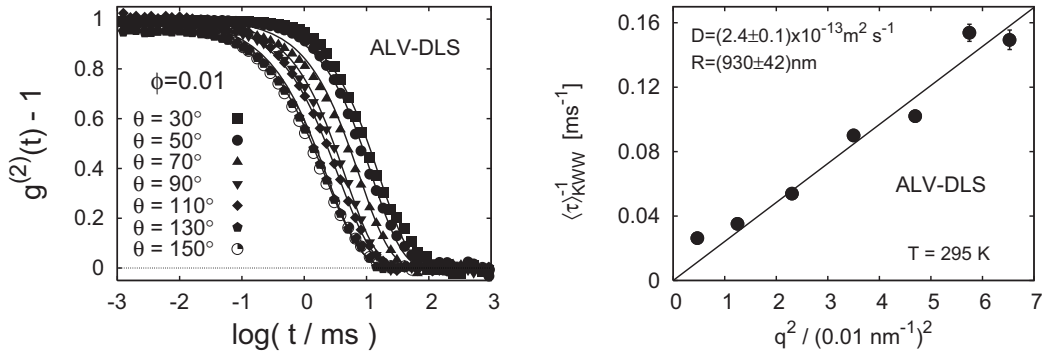

Figure 4.26: Reduced intensity auto-correlation function (left figure) and corresponding angular-dependent relaxation time (right figure) of a mixture of charge-stabilised Ludox particles with $\phi = 0.01$, and dextran with $c/c^* = 0.42$ ($M = 5 \times 10^5$ g/mol), measured using a standard DLS setup at $T = 295$ K and $c_s = 0.3$ mol/l.

4.4.3 Hydrodynamic radius of sedimented colloidal clusters

In Figs. 4.26 and 4.25, we show our results for the size of sedimented clusters for a sample with $\phi = 0.01$, $c/c^* = 0.42$ and $c_s = 0.3$ mol/l, obtained using a standard DLS apparatus and a 3D-DLS setup [235]. The latter setup accounts for multiple scattering in slightly turbid samples. The sample turbidity gradually increases with time, and a lower liquid-like cluster phase is formed after a few days. The hydrodynamic radius of the sedimented aggregates is 0.7 μm, indicating that large clusters have been formed. After shaking the sample, these aggregates sediment to the bottom of the container within an hour and form again a lower turbid fluid-like phase.

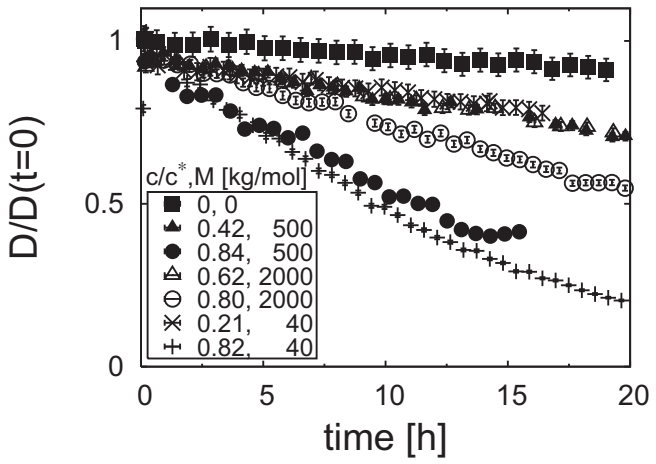

Figure 4.27: Time evolution of the collective diffusion coefficient of silica particles for varying polymer concentrations, and varying polymer molar mass M. The colloidal dispersion has been prepared with $\phi = 0.01$ and $c_s = 0.3\,\mathrm{mol/l}$.

4.4.4 Influence of the polymer-to-colloid size ratio q

Figs. 4.27 and 4.28 show the time evolution of the collective diffusion coefficient, and the scaling behaviour of the hydrodynamic radius, for samples with varying polymer concentration and molar mass at $T = 295\,\mathrm{K}$, $p\mathrm{H} = 9.2 \pm 0.1$, $c_s = 0.3\,\mathrm{mol/l}$, and $\phi = 0.01$. Fig. 4.29 summarises the so-obtained aggregation times in dependence on the polymer concentration. We observe here that τ_a decays with increasing c/c^* for all q considered. It decays, however, faster for smaller q. The curves represent the theoretically calculated $\tau_a(c)$. Good agreement is observed between the theoretical predictions and the experimental data, for polymer concentrations below c^*. For $q = 0.49$, the dimer formation theory agrees well with the experimental τ_a for all $c < c^*$. In contrast, τ_a is predicted correctly by the theory only for $c/c^* \lesssim 0.5$ in case of ratios q much larger than one (i.e, for $q = 2.6 \pm 0.2$). At polymer concentrations near c^* ($c/c^* \approx 0.8$), τ_a decays more rapidly than predicted by the simple dimer formation theory, when $q = 1.4 \pm 0.1$ and $q = 2.6 \pm 0.2$.

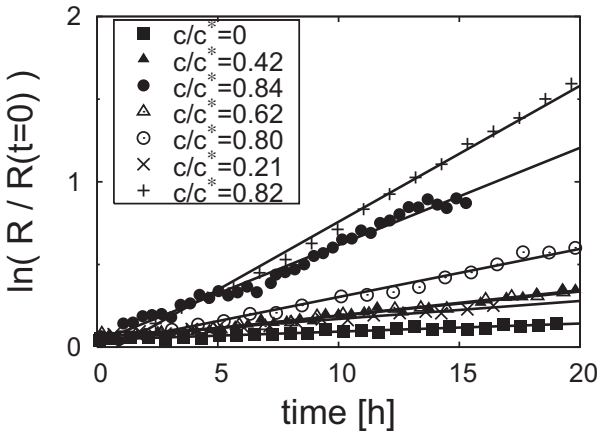

Figure 4.28: Semi-logarithmic plot of the reduced time-dependent hydrodynamic radius of colloid clusters as a function of elapsed time, for a mixture of Ludox spheres at $\phi = 0.01$, and dextran at varying dextran concentrations and molar masses (for $c_s = 0.3\,\mathrm{mol/l}$). The straight lines are fits to the form $R(t) = R(t=0)\exp(t/\tau_a)$, with τ_a and $R(t=0)$ measured right after sample preparation. The data for $M = 5\times10^5\mathrm{g/mol}$ are replotted from Figs. 4.12 and 4.23. (■) $c/c^* = 0$, $\tau_a = (7.8\pm0.1)\,\mathrm{d}$; $q = 0.49\pm0.03$: $M = 4\times10^4\mathrm{g/mol}$, (△), $c/c^* = 0.21$, $\tau_a = (3.8\pm0.1)\,\mathrm{d}$; (□), $c/c^* = 0.82$, $\tau_a = (12.9\pm0.1)\,\mathrm{h}$; $q = 1.4\pm0.1$: $M = 5\times10^5\mathrm{g/mol}$, (▲), $c/c^* = 0.42$, $\tau_a = (2.7\pm0.1)\,\mathrm{d}$; (•), $c/c^* = 0.84$, $\tau_a = (16.2\pm0.1)\,\mathrm{h}$; $q = 2.6\pm0.2$: $M = 2\times10^6\mathrm{g/mol}$, (△), $c/c^* = 0.62$, $\tau_a = (2.8\pm0.1)\,\mathrm{d}$; (○), $c/c^* = 0.80$, $\tau_a = (1.43\pm0.03)\,\mathrm{d}$.

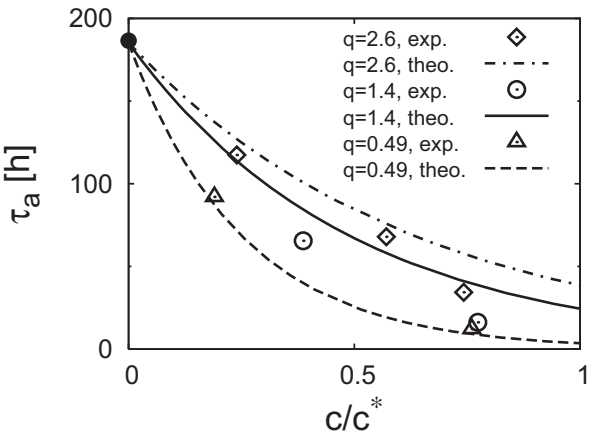

Figure 4.29: The data points (symbols) give the experimentally determined aggregation time as a function of the reduced polymer concentration in a mixture of dextran with varying range of attractions, $q = 0.49\pm0.03$ ($M = 4\times10^4\mathrm{g/mol}$), $q = 1.4\pm0.1$ ($M = 5\times10^5\mathrm{g/mol}$), and $q = 2.6\pm0.2$ ($M = 2\times10^6\mathrm{g/mol}$), and Ludox particles with $\phi = 0.01$ at $c_s = 0.3\,\mathrm{mol/l}$. The curves are the theoretically predicted τ_a based on the AOV potential and Z_{eff} as explained in subsection 4.4.1.

4.5 Non-equilibrium state diagrams

The silica-dextran mixtures investigated so far have a low colloidal volume fraction ($\phi = 0.01$) and low polymer concentrations ($c \lesssim c^*$). These samples form initially a homogeneous and transparent mixture. With increasing delay time after mixing, the samples gradually turn more turbid. In the sections 4.3 and 4.4, we have measured the growth of colloidal clusters using photon correlation spectroscopy, and we have determined the characteristic aggregation time. On the basis of these measurements, we attribute the increasing sample turbidity to the growth of colloidal cluster for samples with $\phi = 0.01$. Samples with $\phi = 0.01$, containing a pure colloidal dispersion without polymers, form a system-spanning gel at later times. When adding polymer chains, the cluster aggregation process is accelerated for $\phi = 0.01$ (see section 4.4).

In contrast, the dispersions behave quite differently when one increases the polymer concentration in the mixture at sufficient high electrolyte concentrations (e.g., for samples with $\phi = 0.01$ and $c_s \gtrsim 0.3\,\mathrm{mol/l}$), or, likewise, when ϕ and c are increased at low salt content ($c_s \leq 0.2\,\mathrm{mol/l}$). At high ϕ, high c and low c_s, the samples become turbid right after mixing of the stock solutions. Then, after several hours, a turbid (milky) and highly viscous fluid forms at the bottom of the container. Depending on the composition of the sample, the bottom turbid phase ceases to flow and forms a white gel within several hours or a few days. The upper

Figure 4.30: Photograph of two samples containing a colloid-polymer mixture of silica spheres and dextran for $c_s = 0.15\,\mathrm{mol/l}$, $\phi = 0.10$, $M = 5 \times 10^5\,\mathrm{g/mol}$, and $c/c^* = 1.67$ at $p\mathrm{H} = 9.2$. Sample (i) was prepared right before the picture has been taken. Sample (ii) has been stored for 1 day at room temperature. The total height of the mixture, h_0, and the height, h, of the more turbid lower phase at the bottom of the tube is indicated by arrows.

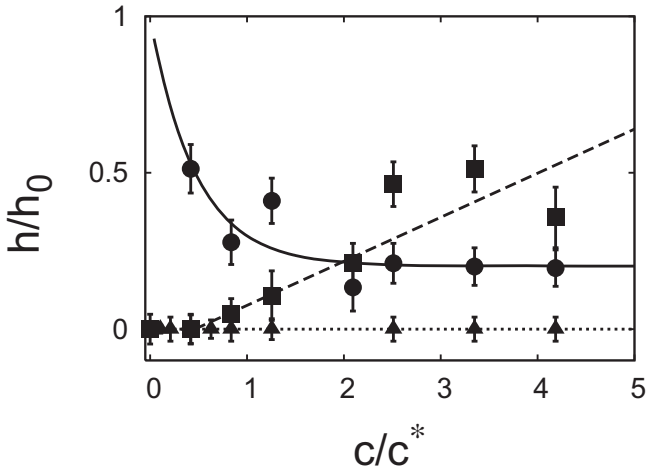

Figure 4.31: Reduced height, h/h_0, of the turbid lower phase formed at the bottom of the sample tube for $\phi = 0.01$ and varying c ($M = 5 \times 10^5$ g/mol). Shown are data for three different salt concentrations: $c_s = 0.15$ mol/l (▲), $c_s = 0.3$ mol/l (■) and $c_s = 0.5$ mol/l (●). The reduced height of the lower phase has been recorded two days after sample preparation, thereafter it has remained constant up to two weeks. The curves are guides to the eye illustrating the general trends.

fluid phase consists of a slightly turbid solution which becomes transparent at later times (see, Fig. 4.30). Furthermore, a sharp interface between the two fluids is visible, which allows to clearly distinguish between the upper and lower phases. Even though we refer here to two fluid phases, this does not imply that these are two equilibrium phases. On the contrary, our time-resolved measurements at low ϕ strongly indicate that this separation process has followed a non-equilibrium route. Note that we describe the region in phase space, where such a phase separation is observed, as unstable. Likewise, we will speak of a stable single-fluid phase otherwise. Note further, however, that clusters can be formed in the single fluid colloidal phase depending on the electrolyte and polymer concentrations. We will discuss in the following whether the observed non-equilibrium phase separation and the measured cluster aggregation processes become related at high colloid volume fractions and high polymer concentrations.

The influence of the electrolyte concentration on the fraction of the system volume occupied by the bottom turbid phase has been studied for $\phi = 0.01$ and $c_s = 0.15$ mol/l, 0.3 mol/l and 0.5 mol/l (see Fig. 4.31). At $c_s = 0.15$ mol/l, the mixture at $\phi = 0.01$ does not demix for all polymer concentrations under investigation. A bottom turbid phase of increasing volume ratio is formed, however, for $c_s = 0.3$ mol/l when c is increased. This deposit can be redispersed by shaking the sample thoroughly. For $c_s = 0.5$ mol/l, we observe a phase separation into a transparent upper and a turbid bottom phase for all c. Interestingly, the volume ratio of the bottom phase, as measured by h, decreases with increasing c. The influence of the polymer molar mass on the volume distribution of the

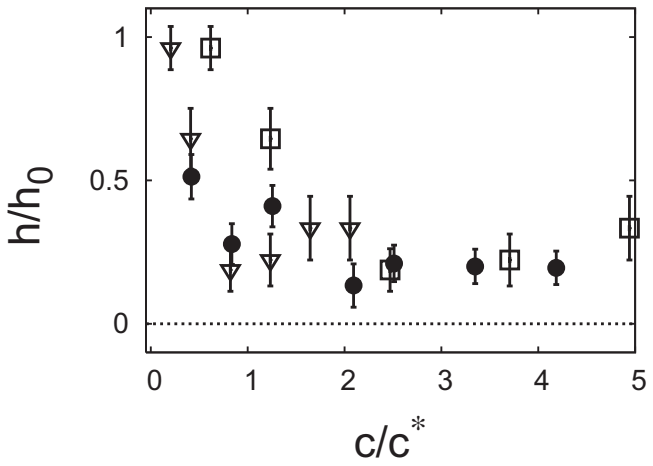

Figure 4.32: Reduced height of the more turbid bottom phase, formed several hours after sample preparation, for a mixture of polymer chains with varying polymer molar mass and Ludox silica particles of $\phi = 0.01$ at $c_s = 0.5\,\mathrm{mol/l}$ and room temperature. The data points (symbols) describe samples of varying polymer molar mass: $M = 4 \times 10^4\,\mathrm{g/mol}$ (▽), $M = 5 \times 10^5\,\mathrm{g/mol}$ (•), $M = 2 \times 10^6\,\mathrm{g/mol}$ (□). The height of the bottom phase is recorded two days after sample preparation, and does not change within a total delay time up to two weeks after sample preparation.

top and bottom phases is recorded in Fig. 4.32 for samples with $\phi = 0.01$ and $c_s = 0.5\,\mathrm{mol/l}$. As depicted in Fig. 4.32, the molar mass has no significant effect on the distribution of the two phases over the system volume.

For c_s in the range between 0.1 mol/l and 0.2 mol/l, the non-equilibrium state diagram has been mapped out in Fig. 4.33. The status of the samples has been recorded two weeks after sample mixing. The curves are guides to the eye to distinguish slightly turbid but homogeneous, one-phase samples (○) from samples which have phase separated (◑), or form a percolated, system-spanning network (gel) (▲). In Fig. 4.34, we show photographs of samples in these different states. The line divides samples forming a single phase from samples which are phase-separated two weeks after preparation. According to Fig. 4.33, this phase line moves to lower ϕ and smaller c with increasing c_s (see, especially, Fig. 4.33 (f)). Furthermore, the phase line shifts to lower ϕ- and c/c^*-values for increasing time (see Fig. 4.35).

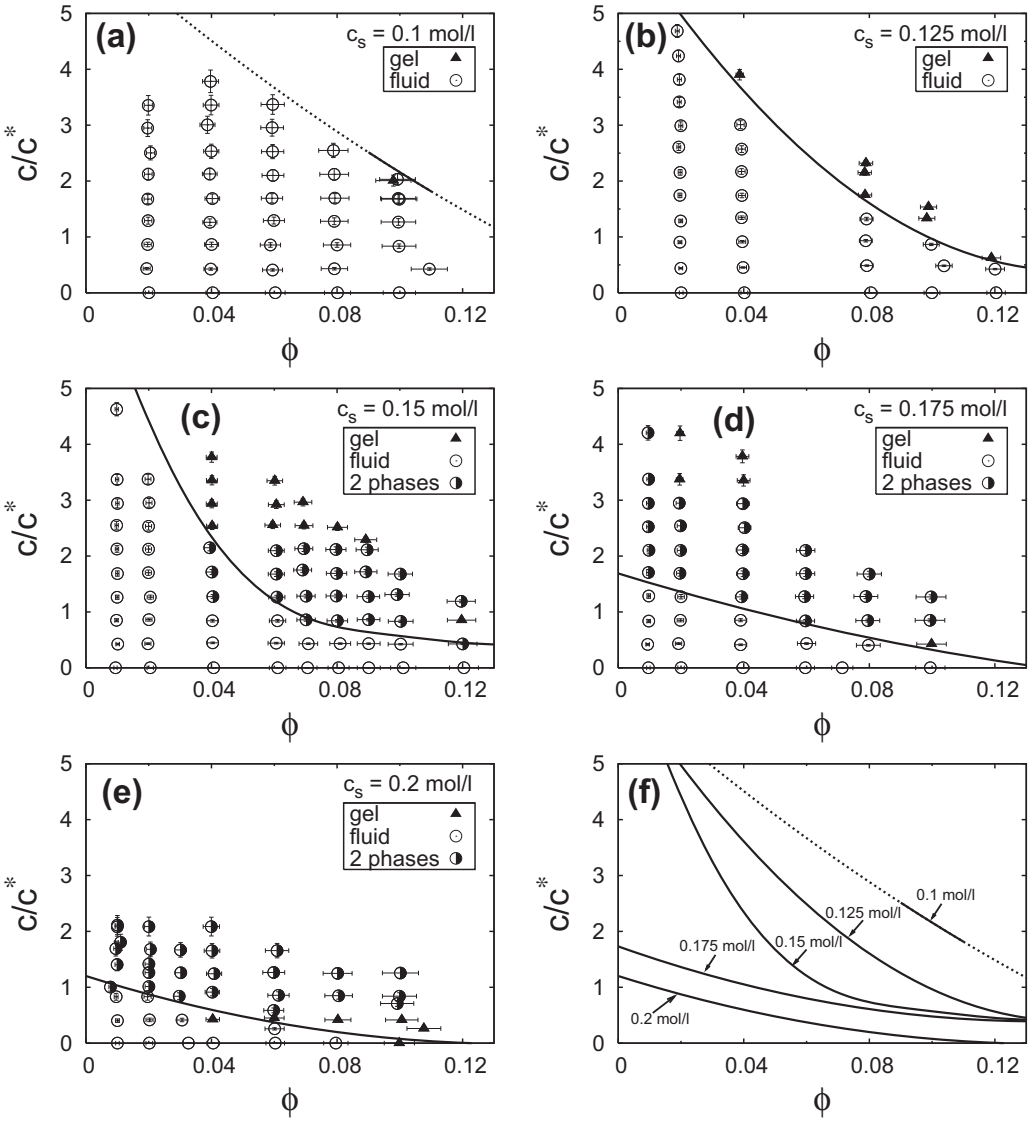

Figure 4.33: Non-equilibrium state diagrams of aqueous mixtures of Ludox silica particles and dextran for varying salt concentrations: chart (a): $c_s = 0.1\,\mathrm{mol/l}$, (b): $c_s = 0.125\,\mathrm{mol/l}$, (c): $c_s = 0.15\,\mathrm{mol/l}$, (d): $c_s = 0.175\,\mathrm{mol/l}$, (e): $c_s = 0.2\,\mathrm{mol/l}$, for $q = (1.4 \pm 0.1)\,\mathrm{nm}$ ($M = 5 \times 10^5\,\mathrm{g/mol}$) at room temperature. The phase diagrams of the samples have been recorded by visual inspection two weeks after sample preparation. Open circles (○) indicate fluid-like homogeneous mixtures. The half-filled circles (◑) describe samples, where a turbid viscous phase is observed at the container bottom. The triangles (▲) mark samples which form a gel throughout the sample. The solid curves separate the single-fluid phase region from the region where phase separation or a system-spanning gel is observed after two weeks. These curves, for all salt concentration considered, are summarised in figure (f).

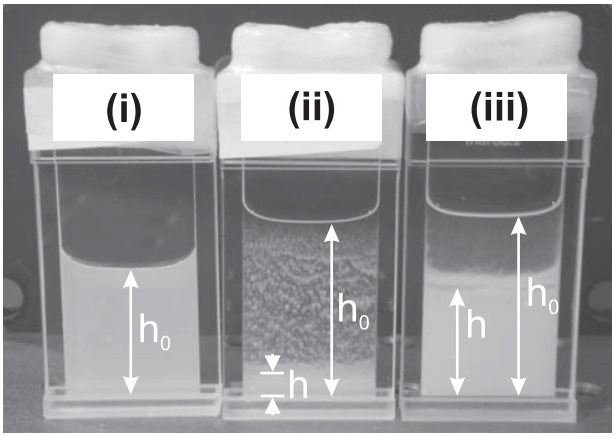

Figure 4.34: Photographs of samples containing a colloid-polymer mixture with $c_s = 0.15\,\mathrm{mol/l}$ (compare to Fig. 4.33(c)), and polymer molar mass $M = 5 \times 10^5\,\mathrm{g/mol}$. The picture has been taken two days after sample preparation. Then, sample (i) ($\phi = 0.04$, $c/c^* = 2.93$) has become turbid and forms a gel at later times. In sample (ii), where $\phi = 0.09$ and $c/c^* = 1.26$, and sample (iii), where $\phi = 0.09$ and $c/c^* = 2.09$, two phases are observed. The total height of the dispersion, h_0, and the height of the more turbid bottom phase, h, are indicated by arrows.

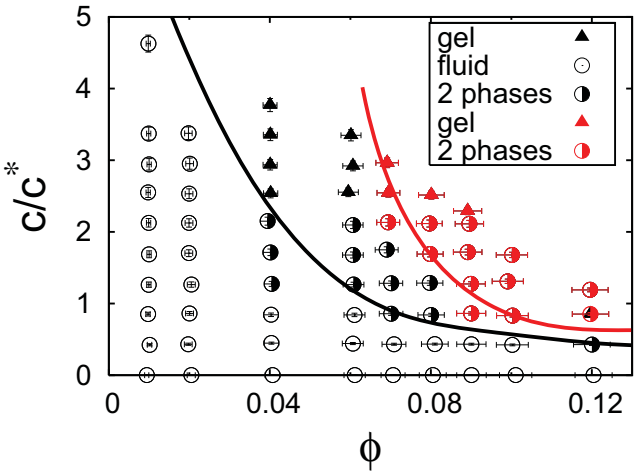

Figure 4.35: Time evolution of the non-equilibrium state diagram for an aqueous mixture of Ludox silica particles and dextran, with $c_s = 0.15\,\mathrm{mol/l}$ and $q = (1.4 \pm 0.4)\,\mathrm{nm}$ ($M = 5 \times 10^5\,\mathrm{g/mol}$). The red symbols give the state of the sample two days after sample preparation. The black symbols describe the sample state after two weeks. The solid curves separate the single-fluid phase region from the phase region where two separated phases or a system-spanning gel are observed.

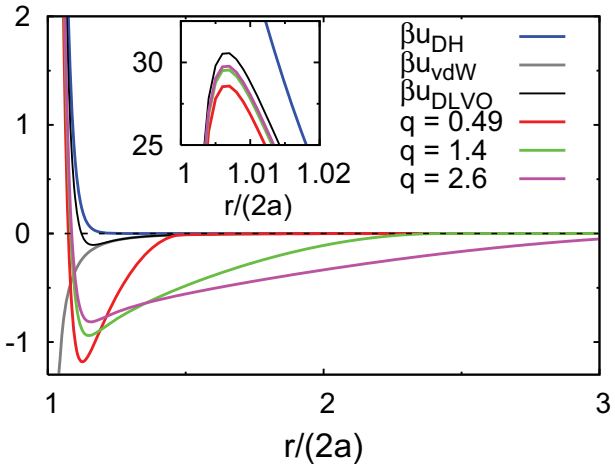

Figure 4.36: Total pair potential $u(r)$ for $q = 0.49 \pm 0.03$ ($M = 4 \times 10^4$g/mol), $q = 1.4 \pm 0.1$ ($M = 5 \times 10^5$g/mol), and $q = 2.6 \pm 0.2$ ($M = 2 \times 10^6$g/mol), with $\phi = 0.01$, $c_s = 0.3$ mol/l, $c_b = 0.01$ mol/l, $T = 295$ K, and constant polymer concentration, $c/c^* = 0.5$. The blue curve is the repulsive electrostatic part, and the grey curve the short-ranged van der Waals part of $u(r)$. The inset focuses on the Coulomb barrier part of $u(r)$ that occurs at smaller particle separations.

4.6 Discussion

We have found that aqueous mixtures of charge-stabilised silica colloids and non-adsorbing dextran polymers aggregate irreversibly into clusters at low colloid volume fractions and small polymer concentrations, with values depending on the strength of the electrostatic repulsion and the polymer-induced depletion attraction. At constant temperature and pH-value, the electrostatic repulsion is tuned by varying the electrolyte concentration.

At a sufficiently low $\phi = 0.01$ and without polymer chains, we observe that the samples are always transparent after mixing. However, the low-ϕ samples gradually turn more turbid, and form a gel after several hours or days for $c_s \geq 0.3$ mol/l. The increasing turbidity is attributed to the formation of clusters, which aggregate to a system-spanning network (gel) at later times. On increasing c_s, the electrostatic repulsion is screened and the Coulomb barrier in $u(r)$ decreases. Thus, at large c_s, smaller inter-particle distances during the rare collision events are probed. At very short distances, the vdW attraction dominates $u(r)$, and the colloids stick irreversibly together, forming clusters of increasing number of particles with increasing delay time. We have found that the cluster growth rate increases with increasing ϕ. This can be attributed to an enlarged collision rate proportional to ϕ^2.

Adding non-adsorbing polymers to a colloidal dispersion adds a depletion attraction part to the DLVO effective pair potential. We find that the polymer concentration and the polymer-to-colloid size ratio strongly affect the aggregation

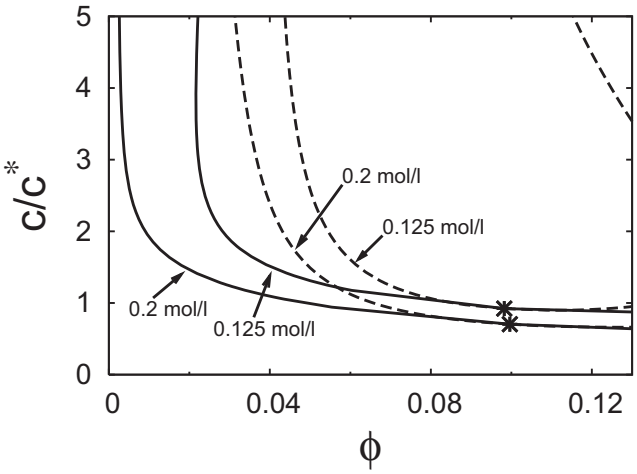

Figure 4.37: Theoretically predicted binodals (solid curves) and spinodals (dashed curves) obtained form GFVT (see chapter 3), for aqueous mixtures of Ludox silica particles and dextran at $c_s = 0.125\,\mathrm{mol/l}$ and $0.2\,\mathrm{mol/l}$, respectively, $c_b = 0.01\,\mathrm{mol/l}$, and $q = 1.4$ on assuming θ-solvent conditions. The asterisks denote the critical point.

kinetics (see Fig. 4.29). With increasing polymer concentration, the aggregation time decreases monotonically for all q considered. Additionally, we observe that the aggregation time decays faster for smaller q where $q < 1$. Furthermore, if the polymer concentration becomes of the order of the overlap concentration, the experimentally observed cluster aggregation rate, for $q = 1.4$ and $q = 2.6$, is faster than predicted by the simple dimer aggregation theory based on the AOV depletion potential.

These findings can be explained as follows: The cluster formation rate grows with increasing polymer concentration due to the increasing osmotic pressure, which pushes the colloidal particles together, and thus, promotes colloidal aggregation. By adjusting the effective colloid charge Z to match the salt-dependent experimental aggregation time, we can quantitatively describe the time-dependent aggregation in mixtures of charge-stabilised colloidal particles and non-adsorbing polymers under θ-solvent conditions, provided that $c < c^*$ (see Fig. 4.29). Note that the depletion attraction is described by the AOV potential without any adjustable parameter. In Fig. 4.36, the pair potential parts of $u(r)$ for $q = 0.49$, 1.4 and 2.6 are plotted for a fixed polymer concentration $c/c^* = 0.5$. Comparing the full pair potential with $u_{\mathrm{DLVO}}(r)$ for varying q, shows that polymer depletion as described by $u_{\mathrm{AOV}}(r)$, adds a long-ranged attraction to $u(r)$. Thus, the polymer-induced depletion reduces the height of the Coulomb barrier in $u(r)$, and creates a pronounced secondary minimum of depth around $1\,k_BT$. Hence, τ_a decreases with increasing c/c^*, and so does W in Eq. (4.8). The range of attraction increases with increasing q as expected for a dilute polymer solution well below c^* (see Fig. 4.36). However, at fixed c/c^*, the strength of the polymer-induced

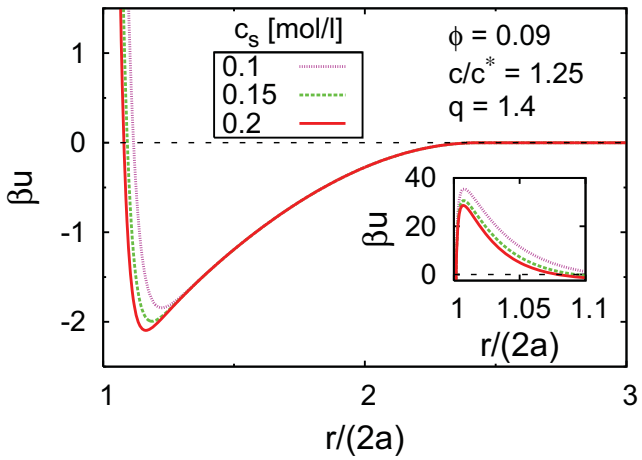

Figure 4.38: Reduced total pair potential, $\beta u(r)$, for $c_s = 0.1\,\mathrm{mol/l}$, $0.15\,\mathrm{mol/l}$ and $0.2\,\mathrm{mol/l}$ with $\phi = 0.09$, $c/c^* = 1.25$, and $q = 1.4$ ($M = 5 \times 10^5 \mathrm{g/mol}$). The inset focuses on the Coulomb barrier part of $u(r)$.

attraction decreases for increasing q like q^{-3} to leading order in a small q, whereas the range of attraction grows linearly in q. Thus, for increasing q, the increasing range of the depletion attraction is outweighted by its decreasing strength (see Fig. 4.36). Accordingly, W and thus τ_a, increase with increasing q for a fixed c/c^*, giving rise to an enhanced colloidal stability. The experimentally observed decrease in τ_a for $q > 1$ and $c/c^* \gtrsim 0.8$, can be explained by the non-ideal solution behaviour of dextran, which is not accounted for in the AO model. As shown in Fig. 3.4 of subsection 3.3.3, the thickness of the depletion layer starts to decrease quickly for polymer concentrations near c^* and for $q > 1$, because the colloid size is then of the order of the polymer correlation length. Therefore, the range of polymer-induced attraction between the colloids decreases with increasing c/c^*. Simultaneously, the osmotic pressure exerted by the polymers on the colloids increases rapidly for $q > 1$ with increasing c/c^* (see Fig. 3.4), and thus, the strength of the depletion attraction increases. Both effects, the decrease in range and the increase in strength of the depletion attractions, enhance the formation of clusters as seen with our experiments.

On increasing ϕ and c, the mixture becomes turbid immediately after sample preparation, and eventually phase separates into a transparent top phase, and a turbid and highly viscous bottom phase at later time (see Fig. 4.34 (i) and (ii)). The region in the non-equilibrium phase diagram where this demixing process occurs, shifts to lower polymer concentrations and lower colloid volume fractions with increasing electrolyte concentration (Fig. 4.33) and, likewise, with increasing time (see Fig. 4.35). The fact that the sample becomes turbid immediately after mixing is reminiscent of critical opalescence occurring during spinodal decomposition. Very recently, Lu *et al.* [181] have provided evidence that gelation is

driven by spinodal decomposition in (model) colloid-polymer mixtures with very short-range attractions ($q = 0.059$). Similar experimental observations have been made earlier by Grant and Russel [236], for a dispersion of sterically stabilised silica particles in an organic solvent. Both groups observed that the gelation line coincides with the spinodal line at low colloid volume fractions. Grant and Russel [236] found that the spinodal line is metastable with respect to the fluid-solid coexistence curve. In systems with longer-ranged colloid attractions, i.e., when $q \gtrsim 0.3$, with the precise value of q depending on the shape of the pair potential, the gel line often lies within the region of the stable gas-liquid coexistence [237]. These findings suggest that gelation in colloid-polymer mixtures can be initiated by spinodal decomposition.

In Fig. 4.37, we show the binodal and spinodal lines obtained using the generalised free-volume theory described in chapter 3, and extended to the present colloid-polymer mixture, for $c_s = 0.125\,\mathrm{mol/l}$ and $0.2\,\mathrm{mol/l}$. In using the GFVT, we disregard the vdW attractions. Furthermore, the range, κ^{-1}, of the electrostatic repulsion in our experimental system is quite large, i.e, we have $m \geq 1.4 > 1.225$ (see Eq. (3.3) of chapter 3, and [140]). Therefore, the GFVT is not quantitatively accurate, and can describe only qualitative trends in our system. At $c_s = 0.1\,\mathrm{mol/l}$, the GFVT predicts a gas-liquid critical point at nonphysically high polymer concentrations of $c/c^* \gtrsim 13$, and it fails to predict the binodal and spinodal lines. Furthermore, the GFVT predicts that the gas-liquid coexistence region reduces for large $c/c^* \gtrsim 3$, as indicated by the spinodal line (long-dashed line) of unphysical negative slope in the top right corner at high ϕ and high c in Fig. 4.37. This unphysical prediction is due to the disregard of the polymer osmotic pressure contribution in the free-volume factor expression in Eq. 3.7 (see chapter 3).

In comparing Figs. 4.35 and 4.37, we see that the experimental phase line in Fig. 4.35, obtained two days after mixing for samples with $c_s = 0.15\,\mathrm{mol/l}$, nearly coincides with the GFVT spinodal line in Fig. 4.37. Hence, a possible explanation for the experimentally observed turbid lower phase goes as follows: First, the sample undergoes spinodal decomposition. During demixing, the colloids aggregate within the denser, colloidal-rich regions. Because the colloids are not buoyancy-matched, the larger clusters sediment to the bottom of the container and form the lower turbid phase observed in the experiment. At later times, the sedimented clusters aggregate, and the bottom phase forms a gel. On diluting a turbid sample ($\phi = 0.09$, $c/c^* = 1.26$, $M = 5 \times 10^5\mathrm{g/mol}$, and $c_s = 0.15\,\mathrm{mol/l}$) with the buffer solution and c_s kept constant a few hours after mixing, we observe a hydrodynamic radius of $R = (21.2 \pm 0.4)\,\mathrm{nm}$ similar to R_0. However, the gel-like bottom phase, which has formed in this sample after a few days, can not be redispersed. To investigate the possible demixing process in more detail, we have plotted $u(r)$ in Fig. 4.38 for $\phi = 0.09$, $c/c^* = 1.25$ and $c_s = 0.15\,\mathrm{mol/l}$. As depicted Fig. 4.35, the polymers induce a long-ranged attraction, which can cause demixing. In addition, a pronounced secondary minimum is formed, which

can cause reversible aggregation. Therefore, we argue that at short times loosely connected aggregates are formed in the denser phase during the polymer-induced phase separation, and that the colloids aggregate irreversible in the denser bottom phase at later times. Note that increasing c_s from 0.1 mol/l to 0.2 mol/l results in a decrease of τ_a from 2845 h to 3 h. Notice further in Fig. 4.33 (f) that we have observed a similar sensitive dependence on c_s for the phase line in our experiments.

However, as noted before, the uncertainties in the theoretically predicted phase diagram are too large to serve as a proof that gelation in our system is always driven by spinodal decomposition, as suggested for similar mixtures by Lu *et al.* [181]. In particular, clear experimental evidence is needed to show that our samples undergo spinodal decomposition at initial times after mixing. Alternatively, one could argue that large sedimented aggregates, which form the turbid bottom phase, have formed within the homogeneous fluid phase without a preceding spinodal decomposition. Our measurements discussed in subsections 4.3.3 and 4.4.2 have shown that τ_a decreases rapidly for increasing ϕ and c, respectively. Thus, one might argue that the formation of larger clusters at high ϕ and high c is solely caused by the enhanced aggregation kinetics. The formation of such a cluster fluid phase has been reported by Lu *et al.* [238] for their buoyancy- and refractive-index-matched model colloid-polymer mixtures. Concerning the observed long-time evolution of the non-equilibrium phase diagrams in Figs. 4.33 and 4.35, we note that the shift of the phase line to lower ϕ and c with increasing time might be attributed to the slow aggregation at low salt conditions. We argue here that large clusters have formed in the mixture. These clusters sediment then to the tube bottom and form a turbid fluid-like phase (see section 4.4.3). Because the Coulomb barrier decreases with increasing c_s, the phase line is shifted to lower ϕ and lower c at larger c_s, as depicted in Fig. 4.33. We have experimentally verified the existence of such micrometre-sized colloidal clusters in the single-fluid phase region, also predicted the GFVT discussed in section 4.4.3, using a 3D-DLS setup. Furthermore, we have shown that these large clusters are free to diffuse in the suspension. In addition, in Figs. 4.31 and 4.32 we have studied the relative height of the bottom phase as a function of c_s and q, respectively, for $\phi = 0.01$. Yet, no systematic effect could be observed. As pointed out by de Hoog *et al.* [167], the final structure of the sediment is caused by a complex interplay between several parameters (see [9] for a thorough discussion).

Interestingly, for 0.125 mol/l $\leq c_s \leq$ 0.2 mol/l the GFVT predicts a large gap in the phase diagram between the binodal and the spinodal lines. In this region of the phase space, the system demixes by nucleation and growth, which might affect the cluster morphology. Yet, our data obtained by visual inspection are too crude to relate the observed phase separation unequivocally to the region in phase space where spinodal decomposition is expected. However, our experiments and the comparison with our theoretical prediction for the equilibrium phase diagram point to an initial phase separation in combination with a

slower ongoing irreversible aggregation process, for low salt concentrations, high polymer concentrations and high colloid volume fractions.

4.7 Conclusions

We have studied the aggregation kinetics and phase behaviour in aqueous mixtures of charge-stabilised silica spheres (Ludox) and non-adsorbing neutral homopolymers (dextran). By varying the polymer molar mass, and the polymer and electrolyte concentrations, we can tune the range and strength of the depletion attraction and electrostatic repulsion at will. In addition, the colloids strongly attract each other at very short inter-particle distances due to van der Waals forces, which can trigger irreversible colloidal aggregation depending on the strength of the Coulomb barrier. For low ϕ, we have measured the time-resolved colloid cluster aggregation rate using photon correlation spectroscopy. From these measurements, we find that the formation of clusters is enhanced with increasing electrolyte and polymer concentrations, and increasing colloid volume fraction. Furthermore, we observe that the cluster aggregation rate decreases with increasing q at fixed c/c^*. It has been demonstrated that the combined effect of salt-induced electrostatic screening, depletion attraction and van der Waals attraction on the initial colloid aggregation, can be quantitatively described for $c < c^*$ by the Smoluchowski dimer formation theory with two-particle hydrodynamic interactions included. We have accounted for the screened electrostatic repulsion using an effective colloid charge determined from adjusting the theoretically obtained τ_a to the experimental one, for a pure colloidal dispersion without added polymers. The depletion attraction is described in our calculations by the AOV potential. At polymer concentrations close to c^*, we find that the aggregation rate is faster than theoretically predicted by the AO model. This effect might be attributed to the non-ideal solution behaviour of dextran for $c/c^* \approx 1$.

With increasing ϕ and c, we observe a few days after sample preparation the formation of a turbid, viscous phase at the container bottom. Thus, a macroscopic phase separation is observed. We find that the phase line shifts to smaller ϕ and smaller c with time. In addition, we find that this line shifts faster to smaller ϕ- and c-values in phase space with increasing electrolyte concentration, due to the enlarged electrostatic screening. This non-equilibrium phase behaviour has been compared to the equilibrium phase diagram predicted by the GFVT devised in chapter 3. We observe that the experimental phase line obtained after two days nearly coincides with the GFVT spinodal line. Therefore, we argue that the long-ranged effective potential $u(r)$, which has a well-developed secondary minimum of about $2\,k_BT$, can drive an initial phase separation into a denser (more turbid) and a less dense phase, accompanied by a more slowly progressing reversible aggregation process. The aggregation can be expected to progress faster in denser regions of the sample.

This scenario of combined initial phase separation and reversible aggregation at short times after sample mixing is evidenced by the observation that the phase-separating sample can be rediluted within a couple of hours into a dispersion of essentially non-aggregated colloidal particles. Furthermore, the formation of a gel-like bottom phase, which can not be rediluted, indicates irreversible aggregation at later times. However, we cannot distinguish clearly between this aforementioned initial phase separation process and the formation and sedimentation of large clusters, which might form in the suspensions in the absence of a preceding spinodal decomposition. Future experiments will be helpful to explore in more detail the demixing mechanism underlying these combined reversible phase separation and irreversible aggregation processes. This will require advanced experimental techniques like small angle x-ray and small angle neutron scattering, to observe at higher ϕ the low-wavelength divergence of the structure factor that signals the onset of the spinodal decomposition. Furthermore, we note that x-ray photon correlation spectroscopy in particular is an appropriate technique at higher ϕ to study the dynamic arrest of silica particles of nanometre size, because it is less plagued by multiple-scattering than light scattering techniques.

Systems with tunable attractive and repulsive interactions will be of interest in future studies for an additional reason: As shown by Pini *et al.* [239] and Archer *et al.* [41], the region in phase space where critical fluctuations become dominant, can largely extend into the thermodynamically stable fluid phase region, for long-ranged weakly repulsive and relatively short-ranged attractive interactions. Hence, in such systems one can explore the dynamics of the cluster aggregation process in the presence of critical density fluctuations and in the absence of spinodal decomposition. We note that these non-equilibrium cluster-aggregation processes should also be compared to equilibrium aggregates formed in those systems after microphase separation [40–42, 239–241]. As an alternative system, it will be useful to design a colloidal dispersion of particles with hard-sphere plus repulsive Yukawa interactions dispersed in a polymer solution. For such a mixture, irreversible aggregation could be prohibited, e.g., by short polymer brushes grafted on the colloid surfaces. These dispersions could be used to extend previous research on hard-sphere-like systems, which has been proven so instructive in the past [96, 169, 181, 191, 192, 238, 242]. A possible candidate for such a system are charged brush-coated poly(methyl methacrylate) (PMMA) spheres.

A Dimer formation theory of initial flocculation

Consider a dispersion which initially consists of non-aggregated colloidal spheres randomly distributed in the system volume V. The spheres describe a Brownian random walk due to solvent collisions. Whenever two particles approach each other so that the short-range inter-particle attractions become dominant, they can form a dimer. If the dispersion is highly diluted, we can neglect three-body and higher order collision events at short times. Then, the formation of dimers can be described by the following evolution equation for the pair probability density, $P_2(r,t)$, of finding two spheres at time t at a centre-to-centre distance r, [6, 178],

$$\frac{\partial P_2(r,t)}{\partial t} = \frac{1}{r^2}\frac{\partial}{\partial r}\left[2D_0\,G(r)\frac{\partial P_2(r,t)}{\partial r} + 2D_0\,G(r)\,P_2(r,t)\frac{d\beta u(r)}{dr}\right]. \qquad \text{(A.1)}$$

The first term in the bracket on the right-hand side arises from the diffusive flux part. This thermally driven diffusion of the colloids tends to smooth out local accumulations of colloidal particle, which occur due to fluctuations in the colloid concentration. The single particle diffusion constant here is $D_0 = k_BT/(6\pi\eta a)$. The second term on the right-hand side accounts for the relative flux arising from the pair potential $u(r)$. At very short inter-particle distances, when the van der Waals attraction dominates $u(r)$, this term becomes negative, favouring a local accumulation of colloidal spheres. Initially, $P_2(r,0) = n_0^2$, where $n_0 = n(t=0)$ is the initial number density of randomly distributed colloids (monomers). The boundary conditions at infinite colloidal separation and on contact distance are $P_2(\infty,t) = n_0^2$ and $P_2(2a,t) = 0$, respectively, assuming a random distribution of spheres for $r \to \infty$ and irreversible dimer formation at contact, respectively. From solving Eq. (A.1) with the aforementioned initial and boundary conditions, the collision rate is obtained to [178],

$$J_{11} = 4\pi\,(2a)^2 \lim_{r\to 2a^+} 2D_0\,G(r)\,\left[\frac{\partial P_2(r,t)}{\partial r} + P_2(r,t)\frac{d\beta u(r)}{dr}\right]. \qquad \text{(A.2)}$$

The time-dependent monomer number concentration, $n(t)$, is then obtained from the rate equation, $dn(t)/dt = -J_{11}$, with $n(t=0) = n_0$, that describes the disappearance of monomers from the suspension. Using a steady-state approximation [178], the solution to Eq. (A.1) reads,

$$P_2(r,t) = n_0^2 \frac{\exp\left[-\beta u(r)\right]\int_{2a}^{r} dr' \frac{\exp\left[\beta u(r')\right]}{r'^2\,G(r')}}{\int_{2a}^{\infty} dr' \frac{\exp\left[\beta u(r')\right]}{r'^2\,G(r')}}, \qquad \text{(A.3)}$$

and the collision rate follows as

$$J_{11} = \frac{8\pi\, D_0 n_0^2}{\int_{2a}^{\infty} dr' \frac{\exp\left[\beta u(r')\right]}{r'^2\, G(r')}}\,, \tag{A.4}$$

For $u(r) = 0$ and $G(r) = 1$, Eq. (A.4) reduces to the classical result of Smoluchowski, first observed for diffusion limited aggregation processes, namely $J_0 = 16\,\pi\, a\, D_0\, n_0^2$. The stability ratio W is defined by

$$W = \frac{J_0}{J_{11}} = 2a \int_{2a}^{\infty} dr \frac{\exp\left[\beta u(r)\right]}{r^2\, G(r)}\,, \tag{A.5}$$

and the characteristic aggregation time for dimer formation follows then as

$$\tau_a = \frac{\pi\, \eta\, a^3}{\phi\, k_B T}\, W\,. \tag{A.6}$$

5 Summary and outlook

In summary, we have investigated theoretically the equilibrium phase behaviour of protein solutions, and mixtures of charge-stabilised colloids and interacting polymer chains. Furthermore, we have studied experimentally the initial aggregation kinetics and non-equilibrium phase behaviour in a model system of charge-stabilised silica particles and non-adsorbing polysaccachride chains in water.

In the first part of this thesis (chapter 2), we have presented and analysed a simple patchy model to describe the equilibrium phase behaviour of charged lysozyme proteins. Our model description accounts for the anisotropic attractive interactions and the electrostatic Coulomb repulsions between the globular proteins. Previous work either addressed the phase diagram on a DLVO-level by assuming purely isotropic interactions [13–15, 19, 57, 243, 244], or the effect of anisotropic interactions was examined using a simple attractive square-well potential only [26, 29, 30, 33, 36, 245]. In our patchy model, we describe the electrostatic repulsion part due to the charges on the protein surfaces by the one-component macroion fluid pair potential, characterised by an effective protein charge [51]. The repulsive interaction part is completely characterised by the solvent conditions, i.e., the electrolyte, protein and buffer concentrations, and the pH-value, which determine the effective charge number of a protein. The anisotropic attractive interaction part is accounted for in our model by an angular-modulated patchy pair potential of Yukawa-type [246]. We have calculated the Helmholtz free energies for the fluid and solid phases by employing the thermodynamic perturbation theory by Barker and Henderson [59], using hard spheres as the reference system. Because the perturbational attractive, and repulsive pair potential parts are angular-averaged over all protein-protein orientations in the free energy calculation, only the surface coverage factor, χ, which describes the surface fraction covered by the attractive patches, enters into the calculation. The parameter χ, and the range and strength of the attractive potential part, have been determined using information on the gas-liquid critical point. Based on this information, we have calculated the complete phase diagram. Our patchy protein model describes the gas-liquid phase coexistence quite well when a temperature-dependent coupling parameter is included which influences the strength of the attractive potential part. In particular, our model nicely captures the influence of added salt on the stability of the liquid phase. Furthermore, the range of attraction predicted in our calculations is in good agreement with experimental data by Israelachvili and Pashley [85], where the force between two hydrophobic-

coated surfaces immersed in water has been measured as a function of their distance. This strongly suggest that the attractive interactions caused by hydrophobic patches on the protein surfaces dominate the phase behaviour in the lysozyme solutions. The overall good agreement between the binodal predicted from our free energy calculations, and the experimental binodal, supports the assumption by Hoskins *et al.* [247] that the local, asymmetric distribution of charges over the protein surface is negligible for solution *p*H-values that are of $2-3$ units away from the isoelectric point. Notwithstanding this success of our model, a more accurate estimate of the χ-factor of lysozyme would be useful, because the surface coverage factor of $\chi \approx 70\%$ obtained in our calculations is near the border of the χ-range for which Kern and Frenkel [28] predict, from their computer simulations, that pre-avering of the interaction potential is still feasible. An accurate value of χ, would allow us to see if micro-ion correlation effects significantly affect the phase behaviour of lysozyme and, if this is the case, we could study these effects in detail. Moreover, further research is necessary to explain the strong widening of the gas-liquid coexistence curves observed in the experiments. From our simple model, we cannot decide whether this is due to the temperature-dependence of the hydrophobic interactions, or to the random distribution of patches across the protein surface. As a test of our model, we have predicted the fluid-solid coexistence curve (the solubility curve), using interaction parameters obtained from experimental data on the gas-liquid critical point. On assuming a fcc lattice structure, reasonable agreement between the experimental and the theoretically predicted solubility curves has been observed. Indeed, predicting state points at which crystals are formed in a protein solution is a highly relevant task in biology. In praxis, the proteins must be in a crystal state before the atomic structure can be investigated using scattering techniques. For this reason, the practical use of such a simple model is evaluated by it's accuracy in predicting the fluid-solid coexistence curve. Therefore, it will be worth to extend our calculations of the solubility curve using a more realistic simple cubic crystal lattice structure. On accounting for the observation by Wukovitz and Yeates [89], that about 36% of all proteins crystallise into the same space group, it might then turn out that a simplistic description of the crystall symmetry is sufficient do predict the solubility curve for a large number of globular proteins [248]. Concerning the practical goal of finding rapid crystallisation paths, in a next step we can use the information gained so far about the interactions of lysozyme proteins to calculate crystal nucleation rates [34], and to improve the design of protein crystallisation reaction containers [249]. Besides the equilibrium phase diagram discussed in chapter 2, it is also very challenging to understand the gel-line discovered in lysozyme dispersions [49]. Here, for example, it is unclear to date whether the anisotropic hydrophobic interactions influence the structure of the network formed by a kinetically arrested spinodal decomposition [79].

In chapter 3, we have derived and analysed the generalised free volume theory (GFVT) in its ability to predict the equilibrium phase behaviour of mixtures of

charge-stabilised spherical colloids and polymer chains of different sizes. To this end, we have compared its predictions for the phase diagram both with computer simulations and experimental data. From this comparison, we have mapped out the conditions for which the free-volume approach can be successfully applied. The GFVT is a thermodynamic description of mixtures of spherical colloidal particles and non-adsorbing polymer chains. It describes such a colloid-polymer binary mixture in a semi-grand canonical ensemble where the mixture is in osmotic equilibrium with an infinite reservoir of polymers chains. The semi-grand canonical free energy in this description consists of two contributions: the canonical free energy of the colloidal dispersion, and a grand-free energy contribution from a reservoir of polymers, which is in contact with the mixture by a semi-permeable membrane impenetrable to the large colloids [250]. The latter term involves the product of the reservoir osmotic pressure of polymers and the free volume, V_{free}, accessible to the polymers in the mixture. Thus, the polymers enter into the free energy calculation only geometrically through V_{free}, which is directly related to the depletion layer around the colloidal sphere, and through the polymer osmotic pressure. By describing the colloid-polymer mixture in the semi-grand canonical ensemble, GFVT accounts for the partitioning of the polymers between the adjacent phases.

In the present work, the GFVT was used to calculate the phase behaviour of mixtures of weakly charged colloids and interacting polymers at $\theta-$ and good solvent conditions. The effects of the solvent quality and of concentrated polymer solutions on the colloid phases was accounted for by interpolating between exact expression for the depletion thickness, and the osmotic pressure, in the dilute limit, and using scaling relations for semi-dilute polymer solutions in good and θ-solvents. Thus, the depletion thickness around a sphere, δ, and the osmotic pressure become a function of the polymer concentration. In semi-dilute polymer solutions, δ becomes of the order of the correlation length, i.e., proportional to the polymer blob size. We have also accounted for curvature effects, that lead to a smaller δ as compared to its value near a flat plane, δ_p. The influence of the solvent quality enters the GFVT calculations in form of scaling exponents and numerical prefactors that depend on the solvent quality. We have described the electrostatic repulsion between the colloidal particles using the repulsive part of the standard DLVO potential. Since we have been primarily interested in colloid-polymer mixtures with relatively thin electric double layers, we have been in the position to map the repulsive Yukawa-type system on an effective hard-sphere system using the first-order BH description of TPT [60]. Consequently, the electrostatic repulsions enters into the free energy expression only by the effective colloid diameter. The free volume accessible to the polymer chains is approximated using the scaled-particle theory [105]. This theory, which allows to calculate the work required to create a cavity for a polymer in the hard-sphere fluid, has recently been extended by Fortini *et al.* [140] to account for electrostatic repulsion, by inserting the effective colloid volume fraction into the Percus-Yevick

compressibility relation. We have compared the result of GFVT with available computer simulation data for the gas-liquid coexistence curve. In the colloid limit, i.e., for polymer-to-colloid size ratios, q, smaller than one, we find nearly quantitative agreement with the simulation data. For $q < 1$, we observe in accord with the simulation data that the gas-liquid coexistence curve shifts to higher critical polymer concentrations with increasing q. Likewise, with increasing q, the colloid volume fraction at the critical point shifts to smaller values both in good and θ-solvent conditions. In case of charged colloidal particles and for $q < 1$, we observe that the colloid-polymer mixtures are stabilised against gas-liquid phase separation with increasing electrostatic repulsion. In the so-called protein, or nano-particle regime, where the colloidal particles are small compared to the polymers ($q > 1$), larger deviations from the simulation data are observed. Thus, for $q > 1$, our calculations can predict only general trends in the phase behaviour in the protein regime. Moreover, for $q > 1$, we observe a strong effect of the solvent quality on the phase behaviour of weakly charged colloids. The gas-liquid coexistence curve in a θ-solvent becomes at low ϕ unaffected by the electrostatic repulsion, whereas in a good solvent the region in the phase diagram, where a homogeneous mixture can be found, increases for $q > 1$ with increasing electrostatic repulsion. This effect is explained from noting that the depletion thickness decreases for increasing q more rapidly for polymer chains in good than in θ-solvent conditions. We conclude that the solvent quality can significantly affect the phase behaviour of mixtures of charge-stabilised colloids and non-adsorbing polymers for $q > 1$.

The colloidal particles usually differ in size and charge in most colloidal suspensions. This polydispersity makes a quantitative comparison with experimental data rather difficult. Hence, it will be rewarding in future work to include polydispersity effects into the free-volume theory. The good accuracy of this theory for $q \leq 1$ is likely due to its self-consistency in the osmotic pressure description, as noted by Dijkstra *et al.* [112]. In fact, the GFVT accounts in a non-systematic way for higher-order terms in the polymer fugacity z_{p} [109]. In this way, the truncation after the first-order term of the expansion of the semi-grand canonical free energy in terms of z_{p} is to some extend compensated. A possible reason for the less good accuracy of the GFVT for $q > 1$ is that we did not account for the fact that the colloids penetrate the polymer coils for $q > 1$. For $q > 1$, the fact that the polymer segments are connected along a chain, and that the depletion thickness becomes of the order of the polymer correlation length, leads to a restriction on the allowed polymer configurations, and thus decreases the free energy [133, 251]. Furthermore, the assumption made in the SPT that the presence of the polymers causes only a small disturbance of the colloidal suspension may be not justifiable in the protein regime so that a more refined description must be used, which accounts explicitly for all polymer conformations in a given positional configuration of colloids [118, 138]. In this refined approach, the depletion forces are attributed to the change of the polymer conformational entropy when

an additional colloid is inserted into the polymer solution. The colloids disturb the chains by reducing the possible polymer conformations, and consequently, give rise to a decrease in the polymer conformational entropy. This loss of entropy is partially compensated by the colloids getting closer together, to create space for a polymer chain to expand. Accordingly, there is a polymer-induced attraction between the colloids.

In chapter 4, we have studied the aggregation kinetics, and the non-equilibrium phase behaviour, in unstable mixtures of charge-stabilised, nanosized silica spheres and non-adsorbing polysaccharide chains using photon correlation spectroscopy and by visual inspection. First, the effect of salt-induced screening of the electrostatic repulsion on the initial aggregation kinetics was investigated in the pure colloidal suspension without added polymers. For this purpose, we followed the time-dependent cluster growth in low-ϕ suspensions by measuring the collective diffusion coefficient of the aggregates. The hydrodynamic radius, R, was then determined from the Stokes-Einstein relation. We have also investigated the effect of increasing colloid volume fraction on the cluster-aggregation growth rate. Following the time-evolution of the hydrodynamic radius, we obtained the salt- and ϕ-dependent aggregation time. From the observed exponential scaling behaviour of R, we conclude that the cluster growth (at least for short times) is induced by a slow and irreversible reaction-limited aggregation process (RLA) at initial times after sample preparation. At later times, we observe an accelerated exponential growth rate for high salt concentrations and large ϕ. This change in the aggregation rate can be explained by a transition from a slow RLA process at early times to a faster progressing RLCA mechanism at later times. To gain quantitative insight, we used the colloid dimer formation theory of initial flocculation. In this theory, the formation of dimers is explained by accounting for the electrostatic repulsion on the DLVO-level and the inclusion of van der Waals attractions. A theoretical description of the experimentally observed aggregation time has been achieved using the van der Waals force parameters of fused silica nanoparticles dispersed in water known from previous experiments, and by adjusting the effective colloid charge number in dependence of the salt concentration. In this way, we have circumvented the well-known difficulties in predicting aggregation rates in colloidal dispersion theoretically from first principles.

In the second part of chapter 4, we have added polymers to colloidal dispersions at low colloid volume fractions. We find that the collective diffusion coefficient of clusters decreases with increasing polymer concentration. The aggregation growth rate decreases with increasing q, i.e., with increasing polymer molar mass. We have shown that the polymer-induced aggregation rate is well described theoretically by the Asakura-Oosawa-Vrij depletion potential for polymer concentrations below the overlap concentration c^*. For $c \approx c^*$, the experimental aggregation rate is faster than theoretically predicted, since non-ideal polymer solution properties become important. This result is in agreement with previous experimental observations that water-dissolved dextran is close to the θ-solvent

condition at room temperature [162]. Finally, we have prepared and analysed samples of varying polymer concentration and colloid volume fraction, for different amounts of added salt. At high c and large ϕ, the samples become immediately turbid after preparation, and a turbid lower phase is formed at the bottom of the tube with progressing observation time. This bottom phase ceases to flow after several hours and forms then a gel. This is indicative of a phase separation process accompanied by a slower and irreversible cluster aggregation process [181, 183]. We speculate that the bottom phase is formed by micrometre-sized colloidal clusters. In addition, we have compared the experimentally observed non-equilibrium phase diagrams at various salt concentrations, with the theoretically predicted equilibrium phase diagram obtained from the GFVT described in chapter 3. In both phase diagrams, the homogeneous mixture is stabilised, as expected, when the electrostatic repulsion becomes stronger. Furthermore, we find that the region in our experimental non-equilibrium phase diagram, where phase separation is observed at short times after mixing, coincides with the region enclosed by the spinodal line obtained from the equilibrium GFVT. This suggests that the experimentally observed turbid phase at the tube bottom is due to the aggregation of large cluster in the colloid-rich phase during demixing, that sediment to the bottom of the container and form a dense phase.

In future work, it will be interesting to study experimentally the fast demixing process at high polymer concentrations and high colloid volume fractions using, e.g., x-ray correlation spectroscopy and small-angle x-ray scattering. Furthermore, little is known to date about the influence of long-ranged, polymer-induced attractions on the cluster fractal dimension. The fractal dimensions can be determined, in principle, by small-angle light scattering. On the theoretical side, it will be worth to explore the interplay between demixing and accompanying cluster aggregation.

Abbreviations

AO	Asakura-Oosawa (approximation)
AOV	Asakura-Oosawa-Vrij (potential)
BH	Barker-Henderson (approximation)
CMCT	cluster mode-coupling theory
DH	Debye-Hückel (theory)
DLA	diffusion limited aggregation
DLCA	diffusion limited cluster aggregation
DLVO	Derjaguin-Landau-Verwey-Overbeek (potential)
FVT	free-volume theory
GFVT	generalised free-volume theory
IA	irreversible aggregation (process)
MCT	mode-coupling theory
MSA	Mean-Spherical Approximation
PAO	penetrable Asakura-Oosawa (model)
PRISM	polymer reference interaction site model
PY	Percus-Yevick (approximation)
RA	reversible aggregation
RLA	reaction limited aggregation
RLCA	reaction limited cluster aggregation
SPT	scaled-particle theory
TPT	thermodynamic perturbation theory

Bibliography

[1] R. B. Laughlin. *A Different Universe: Reinventing Physics from the Bottom Down*. Basic Books, New York, 2005. chapt. 4, p. 33–45.

[2] H. Löwen. *Kolloide*. 28th IFF-Ferienkurs, Institut für Festkörperforschung, Forschungszentrum Jülich, Jülich, 1997.

[3] C. N. Likos. *Phys. Rep.*, 348:267, 2001.

[4] A. R. Denton. Effective Interactions in Soft Materials. In A. V. Zvelindovsky, editor, *Nanostructured Soft Matter: Experiment, Theory, Simulation and Perspectives*, page 395, Springer, Berlin, 2007.

[5] D. Frenkel. *Physica A*, 313:1, 2002.

[6] W. B. Russel, D. A. Saville, and W. R. Schowalter. *Colloidal Dispersions*. Cambridge University Press, Cambridge, 1992.

[7] A. Vrij, J. W. Jansen, J. K. G. Dhont, C. Pathmamanoharan, M. M. Kops-Werkhoven, and H. M. Fijnaut. *Far. Dis.*, 76:19, 1983.

[8] H. Löwen. *Phys. Rep.*, 237:249, 1994.

[9] J. K. G. Dhont. *An Introduction to Dynamics of Colloids*. Elsevier, Amsterdam, 1996.

[10] A. McPherson. *Crystallization of Biological Macromolecules*. Cold Spring Harbor Laboratory Press, New York, 1st edition, 1999.

[11] R. Cudney, S. Patel, K. Weisgraber, Y. Newhouse, and A. McPherson. *Acta Crystallogr. D, Sect. D: Biol. Crystallogr.*, 50(4):414, 1994.

[12] E. J. W. Verwey and J. Th. G. Overbeek. *Theory of the Stability of Lyophobic Colloids*. Dover Publications Inc., New York, 2000.

[13] G. Pellicane, D. Costa, and C. Caccamo. *J. Phys.: Condens. Matter*, 15(3):375, 2003.

[14] A. Tardieu, A. L. Verge, M. Malfois, F. Bonnete, S. Finet, M. Ries-Kautt, and L. Belloni. *J. Cryst. Growth*, 196(2-4):193, 1999.

[15] M. Muschol and F. Rosenberger. *J. Chem. Phys.*, 103(24):10424, 1995.

[16] P. Prinsen and T. Odijk. *J. Chem. Phys.*, 125(7):074903, 2006.

[17] R. Piazza. *J. Cryst. Growth*, 196(2–4):415, 1999.

[18] D.F. Rosenbaum and C. F. Zukoski. *J. Cryst. Growth*, 169(4):752, 1996.

[19] M. L. Broide, Tina M. Tominc, and Marc D. Saxowsky. *Phys. Rev. E*, 53(6):6325, 1996.

[20] RCSB Protein Data Bank. http://www.rcsb.org/pdb/home/home.do.

[21] H. J. Bernstein. RasMol. http://openrasmol.org/, 2000–2008.

[22] V. G. Taratuta, A. Holschbach, G. M . Thurston, D. Blankschtein, and G. B. Benedek. *J. Chem. Phys.*, 94:2140, 1990.

[23] A. George and W. W. Wilson. *Acta Crystallogr. D, Sect. D: Biol. Crystallogr.*, 50(4):361, 1994.

[24] P. R. ten Wolde and D. Frenkel. *Science*, 277:1975, 1997.

[25] R. Piazza. *Curr. Opin. Colloid Interface Sci.*, 5(1–2):38, 2000.

[26] A. Lomakin, N. Asherie, and G. B. Benedek. *Proc. Natl. Acad. Sci.*, 96:9465, 1999.

[27] A. Lomakin, N. Asherie, and G. B. Benedek. *J. Chem. Phys.*, 104(4):1646, 1996.

[28] N. Kern and D. Frenkel. *J. Chem. Phys.*, 118(21):9882, 2003.

[29] H. Liu, S. K. Kumar, and F. Sciortino. *J. Chem. Phys.*, 127(8):084902, 2007.

[30] R. P. Sear. *J. Chem. Phys.*, 111(10):4800, 1999.

[31] M. S. Wertheim. *J. Stat. Phys.*, 35(1–2):19, 1984.

[32] M. S. Wertheim. *J. Stat. Phys.*, 35(1–2):35, 1984.

[33] P. B. Warren. *J. Phys.: Condens. Matter*, 14(33):7617, 2002.

[34] N. M. Dixit and C. F. Zukoski. *J. Chem. Phys.*, 117(18):8540, 2002.

[35] N. M. Dixit, A. M. Kulkarni, and C. F. Zukoski. *Colloids and Surfaces A*, 190(1-2):47, 2001.

[36] R. Fantoni, D. Gazzillo, A. Giacometti, M. A. Miller, and G. Pastore. *J. Chem. Phys.*, 127:234507, 2007.

[37] V. Talanquer. *J. Chem. Phys.*, 122(8):084704, 2005.

[38] J. Chang, A. M. Lenhoff, and S. I. Sandler. *J. Chem. Phys.*, 120(6):3003, 2004.

[39] E. Bianchi, J. Largo, P. Tartaglia, E. Zaccarelli, and F. Sciortino. *Phys. Rev. Lett.*, 97(16):168301, 2006.

[40] A. J. Archer and N. B. Wilding. *Phys. Rev. E*, 76(3):031501, 2007.

[41] A. J. Archer, D. Pini, R. Evans, and L. Reatto. *J. Chem. Phys.*, 126:014104, 2007.

[42] R. P. Sear and W. M. Gelbart. *J. Chem. Phys.*, 110(9):4582, 1999.

[43] A. Stradner, H. Sedgwick, F. Cardinaux, W. C. K. Poon, S. U. Egelhaaf, and P. Schurtenberger. *Nature*, 432:492, 2004.

[44] E. Allahyarov, H. Löwen, J. P. Hansen, and A. A. Louis. *Phys. Rev. E*, 67(5):051404, 2003.

[45] J. Chang, A. M. Lenhoff, and S. I. Sandler. *J. Phys. Chem. B*, 109(41):19507, 2005.

[46] M. Carpineti and R. Piazza. *Phys. Chem. Chem. Phys.*, 6:1506, 2004.

[47] R. A. Curtis, C. Steinbrecher, M. Heinemann, H. W. Blanch, and J. M. Prausnitz. *Biophys. Chem.*, 98:249, 2002.

[48] M. G. Noro and D. Frenkel. *J. Chem. Phys.*, 113(8):2941, 2000.

[49] F. Cardinaux, T. Gibaud, A. Stradner, and P. Schurtenberger. *Phys. Rev. Lett.*, 99(11):118301, 2007.

[50] D. C. Phillips. *Proc. Natl. Acad. Sci.*, 57(3):483, 1967.

[51] L. Belloni. *J. Chem. Phys.*, 85(1):519, 1986.

[52] P. Prinsen and T. Odijk. *J. Chem. Phys.*, 127:115102, 2007.

[53] E. Allahyarov, H. Löwen, A. A. Louis, and J. P. Hansen. *Europhys. Lett.*, 57(5):731, 2002.

[54] D. E. Kuehner, C. Heyer, C. Ramsch, U. M. Fornefeld, H. W. Blanch, and J. M. Prausnitz. *Biophys. J.*, 73(6):3211, 1997.

[55] W. C. K. Poon, S. U. Egelhaaf, P. A. Beales, A. Salonen, and L. Sawyer. *J. Phys.: Condens. Matter*, 12(35):L569, 2000.

[56] A. Stradner, F. Cardinaux, and P. Schurtenberger. *J. Phys. Chem. B*, 110(42):21222, 2006.

[57] F. Cardinaux, A. Stradner, P. Schurtenberger, F. Sciortino, and E. Zaccarelli. *Europhys. Lett.*, 77(4):48004, 2007.

[58] C. Tanford and R. Roxby. *Biochemistry*, 11(1):2192, 1972.

[59] J. A. Barker and D. Henderson. *Rev. Mod. Phys.*, 48(4):587–671, 1976.

[60] J. A. Barker and D. Henderson. *J. Chem. Phys.*, 47(8):2856, 1967.

[61] N. F. Carnahan and K. E. Starling. *J. Chem. Phys.*, 51(2):635, 1969.

[62] L. K. Steinrauf. *Acta Cryst.*, 12:77, 1959.

[63] S. Zhou. *J. Chem. Phys.*, 127:084512, 2007.

[64] C. Rascón, L. Mederos, and G. Navascués. *Phys. Rev. E*, 54(2):1261, 1996.

[65] C. Rascón, L. Mederos, and G. Navascués. *Phys. Rev. E*, 53(6):5698, 1996.

[66] J. M. Kincaid and J. J. Weis. *Mol. Phys.*, 34(4):931, 1977.

[67] W. W. Wood. *J. Chem. Phys.*, 20(8):1334, 1952.

[68] D. Frenkel and A. J. C. Ladd. *J. Chem. Phys.*, 81(7):3188, 1984.

[69] G. Nägele. *The Physics of Colloidal Soft Matter*. Lecture Notes 14, Institute of Fundamental Technological Research Publishing, Polish Academy of Sciences, Warsaw, 2004.

[70] L. Verlet and J.-J. Weis. *Phys. Rev. A*, 5(2):939, 1972.

[71] M. S. Wertheim. *Phys. Rev. Lett.*, 10(8):321, 1963.

[72] G. J. Throop and R. J. Bearman. *J. Chem. Phys.*, 42(7):2408, 1965.

[73] M. H. J. Hagen and D. Frenkel. *J. Chem. Phys.*, 101(5):4093, 1994.

[74] T. W. Cochran and Y. C. Chiew. *J. Chem. Phys.*, 121(3):1480, 2004.

[75] B. Rotenberg, J. Dzubiella, J.-P. Hansen, and A. A. Louis. *Mol. Phys.*, 102(1):1, 2004.

[76] M. Dijkstra, J. M. Brader, and R. Evans. *J. Phys.: Condens. Matter*, 11(50):10079, 1999.

[77] A. P. Gast, C. K. Hall, and W. B. Russel. *J. Colloid Interface Sci.*, 96(1):251, 1983.

[78] W. H. Press, S. A. Teukolsky, W. T. Vetterling, and B. P. Flannery. *Numerical Recipes in C*. Cambridge University Press, New York, 2 edition, 1992.

[79] T. Gibaud. *Proteins as Model Colloids or the Physics of Dynamical Arrest*. PhD thesis, University of Fribourg, 2008.

[80] G. Foffi and F. Sciortino. *J. Phys. Chem. B*, 111(33):9702, 2007.

[81] P. M. Chaikin and T. C. Lubensky. *Principles of Condensed Matter Physics*. Cambridge University Press, New York, 1992.

[82] Dong Fu, Yigui Li, and Jianzhong Wu. *Phys. Rev. E*, 68(1):011403, Jul 2003.

[83] P. Bolhuis and D. Frenkel. *Phys. Rev. Lett.*, 72(14):2211, 1994.

[84] To our knowledge, the influence of short-range repulsion on the metastability of an attractive and repulsive hard-sphere Yukawa potential system has not been investigated. Therefore, we discuss the effect of the range of attraction on the (global) phase diagram by means of the existing literature on purely attractive hard-sphere plus Yukawa potentials [73].

[85] J. Israelachvili and R. Pashley. *Nature*, 300(25):341, 1982.

[86] P. R. ten Wolde. *J. Phys.: Condens. Matter*, 14:9445, 2002.

[87] D. Horinek, A. Serr, M. Geisler, T. Pirzer, U. Slotta, S. Q. Lud, J. A. Garrido, T. Scheibel, T. Hugel, and R. R. Netz. *Proc. Natl. Acad. Sci.*, 105(8):2842, 2008.

[88] D. M. Huang and D. Chandler. *Proc. Natl. Acad. Sci.*, 97(15):8324, 2000.

[89] S. W. Wukovitz and T. O. Yeates. *Nat. Struct. Biol.*, 2(12):1062, 1995.

[90] A. W. Wilber, J. P. K. Doye, A. A. Louis, E. G. Noya, M. A. Miller, and P. Wong. *J. Chem. Phys.*, 127(8):085106, 2007.

[91] J. P. K. Doye, A. A. Louis, I.-C. Lin, L. R. Allen, E. G. Noya, A. W. Wilber, H. C. Kok, and R. Lyus. *Phys. Chem. Chem. Phys.*, 9:2197, 2007.

[92] J. J. McManus, A. Lomakin, O. Ogun, A. Pande, M. Basan, J. Pande, and G. B. Benedek. *Proc. Natl. Acad. Sci.*, 104:16856, 2007.

[93] H. Ruiz-Estrada, M. Medina-Noyola, and G. Nägele. *Physica A*, 168(3):919, 1990.

[94] M. Ataka and M. Asai. *J. Cryst. Growth*, 90(1-3):86, 1988.

[95] F. Ewing, Forsythe E., and M. Pusey. *Acta Crystallogr. D, Sect. D: Biol. Crystallogr.*, 50(4):424, 1994.

[96] W. C. K. Poon. *J. Phys.: Condens. Matter*, 14(33):R859, 2002.

[97] R. Tuinier, J. Rieger, and C. G. de Kruif. *Adv. Colloid Interface Sci.*, 103:1, 2003.

[98] S. Asakura and F. Oosawa. *J. Chem. Phys.*, 22:1255, 1954.

[99] S. Asakura and F. Oosawa. *J. Polym. Sci.*, 33:183, 1958.

[100] A. Vrij. *Pure Appl. Chem.*, 48:471, 1976.

[101] H. de Hek and A. Vrij. *J. Colloid Interface Sci.*, 84:409, 1981.

[102] B. Vincent. *Colloids Surf.*, 24(4):269, 1987.

[103] B. Vincent, J. Edwards, S. Emmett, and R. Croot. *Colloids Surf.*, 31:267, 1988.

[104] H. N. W. Lekkerkerker, W. C. K. Poon, P. N. Pusey, A. Stroobants, and P. W. Warren. *Europhys. Lett.*, 20:559, 1992.

[105] H. L. Reiss, H. Frisch and J. L. Lebowitz. *J. Chem. Phys.*, 31:369, 1959.

[106] J. L. Lebowitz, E. Helfand, and E. Praestgaard. *J. Chem. Phys.*, 43:774, 1965.

[107] E. J. Meijer and D. Frenkel. *J. Chem. Phys.*, 100:6873, 1994.

[108] R. C. L. Vink and J. Horbach. *J. Chem. Phys.*, 121(7):3253, 2004.

[109] M. Dijkstra, R. van Roij, and R. Evans. *Phys. Rev. E*, 59:5744, 1999.

[110] M. Dijkstra, R. van Roij, and R. Evans. *Phys. Rev. Lett.*, 82:117, 1999.

[111] M. Dijkstra, R. van Roij, and R. Evans. *J. Chem. Phys.*, 113:4799, 2000.

[112] M. Dijkstra, R. van Roij, R. Roth, and A. Fortini. *Phys. Rev. E*, 73:041404, 2006.

[113] A. Moncho-Jordá, A. A. Louis, P. G. Bolhuis, and R. Roth. *J. Phys.: Condens. Matter*, 15:S3429, 2003.

[114] M. Fuchs and K. S. Schweizer. *J. Chem. Phys.*, 106(1):347, 1997.

[115] M. Fuchs and K. S. Schweizer. *Europhys. Lett.*, 51(6):621, 2000.

[116] M. Fuchs and K. S. Schweizer. *Phys. Rev. E*, 64:021514, 2001.

[117] Y. L. Chen and K. S. Schweizer. *J. Chem. Phys.*, 118:3880, 2003.

[118] M. Fuchs and K. S. Schweizer. *J. Phys.: Condens. Matter*, 14:R239, 2002.

[119] S. Ramakrishnan, M. Fuchs, K. S. Schweizer, and C. F. Zukoski. *Langmuir*, 18:1082, 2002.

[120] S. Ramakrishnan, M. Fuchs, K. S. Schweizer, and C. F. Zukoski. *J. Chem. Phys.*, 116:2201, 2002.

[121] S. A. Shah, S. Ramakrishnan, Y. L. Chen, K. S. Schweizer, and C. F. Zukoski. *Langmuir*, 19:5128, 2003.

[122] C. P. Royall, D. G. A. L. Aarts, and H. Tanaka. *Nature Phys.*, 3:636, 2007.

[123] D. Pini, F. Lo Verso, M. Tau, A. Parola, and L. Reatto. *Phys. Rev. Lett.*, 100(5):055703, 2008.

[124] V. B. Tolstoguzov. *Food Hydrocolloids*, 4:429, 1991.

[125] V. Ya Grinberg and V. B. Tolstoguzov. *Food Hydrocolloids*, 11:145, 1997.

[126] D. Marenduzzo, K. Finan, and P. R. Cook. *J. Cell Biol.*, 175(5):681, 2006.

[127] T. Odijk. *Biophys. J.*, 73:23, 1988.

[128] R. de Vries. *Biophys. J.*, 80(3):1186, 2001.

[129] P. G. Bolhuis and A. A. Louis. *Macromolecules*, 35:1860, 2002.

[130] P. G. Bolhuis, A. A. Louis, J. P. Hansen, and E. J. Meijer. *J. Chem. Phys.*, 114:4296, 2001.

[131] A. A. Louis, P. G. Bolhuis, J. P. Hansen, and E. J. Meijer. *Phys. Rev. Lett.*, 85:2522, 2000.

[132] P. G. Bolhuis, A. A. Louis, and J. P. Hansen. *Phys. Rev. Lett.*, 89(12):128302, 2002.

[133] M. Schmidt and M. Fuchs. *J. Chem. Phys.*, 117(13):6308, 2002.

[134] D. G. A. L. Aarts, R. Tuinier, and H. N. W. Lekkerkerker. *J. Phys.: Condens. Matter*, 14:7551, 2002.

[135] E. Eisenriegler, A. Hanke, and S. Dietrich. *Phys. Rev. E*, 54:1134, 1996.

[136] A. Hanke, E. Eisenriegler, and S. Dietrich. *Phys. Rev. E*, 59:6853, 1999.

[137] F. W. Tavares and S. I. Sandler. *AIChE J.*, 43(1):218, 1997.

[138] P. G. Ferreira, M. Dymitrowska, and L. Belloni. *J. Chem. Phys.*, 113:9849, 2000.

[139] A. R. Denton and M. Schmidt. *J. Chem. Phys.*, 122:244911, 2005.

[140] A. Fortini, M. Dijkstra, and R. Tuinier. *J. Phys.: Condens. Matter*, 17:7783, 2005.

[141] G. J. Fleer and R. Tuinier. *Phys. Rev. E*, 76:041802, 2007.

[142] G. J. Fleer, A. M. Skvortsov, and R. Tuinier. *Macromol. Theory Simul.*, 16:531, 2007.

[143] R. Tuinier, P. A. Smith, W. C. K. Poon, S. U. Egelhaaf, D. G. A. L. Aarts, H. N. W. Lekkerkerker, and G. J. Fleer. *Europhys. Lett.*, 82(6):68002, 2008.

[144] H. N. W. Lekkerkerker. *Colloids Surf.*, 51:419, 1990.

[145] S. M. Oversteegen and R. Roth. *J. Chem. Phys.*, 122:214502, 2005.

[146] J. M. Brader, M. Dijkstra, and R. Evans. *Phys. Rev. E*, 63:041405, 2001.

[147] A. A. Louis, P. G. Bolhuis, E. J. Meijer, and J. P. Hansen. *J. Chem. Phys.*, 117(4):1893, 2002.

[148] G. J. Fleer and R. Tuinier. *Physica A*, 379(52):52, 2007.

[149] E. Eisenriegler. *J. Chem. Phys.*, 79(2):1052, 1983.

[150] P. G. de Gennes. *Scaling Concepts in Polymer Physics*. Cornell University Press, Ithaca, 1979.

[151] G. J. Fleer, A. M. Skvortsov, and R. Tuinier. *Macromolecules*, 36:7857, 2003.

[152] A. A. Louis, P. G. Bolhuis, E. J. Meijer, and J. P. Hansen. *J. Chem. Phys.*, 116(23):10547, 2002.

[153] T. Taniguchi, T. Kawakatsu, and K. Kawasaki. *Slow Dynamics in Condensed Matter (AIP Series Vol. 256)*. American Institute of Physics, New York, 1992. p. 503.

[154] G. J. Fleer and R. Tuinier. *Adv. Colloid Interface Sci.*, 143:1, 2008.

[155] P. G. Bolhuis, E. J. Meijer, and A. A. Louis. *Phys. Rev. Lett.*, 90(6):068304, 2003.

[156] A. P. Hynninen and M. Dijkstra. *Phys. Rev. E*, 68:021407, 2003.

[157] W. G. Hoover and F. H. Ree. *J. Chem. Phys.*, 49:3609, 1968.

[158] A. A. Louis. *J. Phys.: Condens. Matter*, 14:9187, 2002.

[159] A. R. Hoskins, I. D. Robb, and P. A. Williams. *Biopolymers*, 45:97, 1998.

[160] C. L. A. Berli, J. A. Deiber, and M. C. Anon. *Food Hydrocolloids*, 13:507, 1999.

[161] H. Chick and C. J. Martin. *Biochem. J.*, 7(1):92, 1913.

[162] E. Nordmeier. *J. Phys. Chem.*, 97:5770, 1993.

[163] T. C. Halsey. *Physics Today*, 53:36, 2000.

[164] T. Vicsek. *Fractal Growth Phenomena*. World Scientific, Singapore, 2 edition, 1992.

[165] T. A. Witten and M. E. Cates. *Science*, 232(4758):1607, 1986.

[166] D. A. Weitz and M. Oliveria. *Phys. Rev. Lett.*, 52(16):1433, 1984.

[167] E. H. A. de Hoog, W. K. Kegel, A. van Blaaderen, and H. N. W. Lekkerkerker. *Phys. Rev. E*, 64:021407, 2001.

[168] A. D. Dinsmore and D. A. Weitz. *J. Phys.: Condens. Matter*, 14:7581, 2002.

[169] H. Sedgwick, S. U. Egelhaaf, and W. C. K. Poon. *J. Phys.: Condens. Matter*, 16:S4913, 2004.

[170] D. W. Schaefer, J. E. Martin, P. Wiltzius, and D. S. Cannell. *Phys. Rev. Lett.*, 52(26):2371, 1984.

[171] J. Feder, T. Jossang, and E. Rosenqvist. *Phys. Rev. Lett.*, 53(15):1403, 1984.

[172] D. A. Weitz, J. S. Huang, M. Y. Lin, and J. Sung. *Phys. Rev. Lett.*, 53(17):1657, 1984.

[173] T. A. Witten and L. M. Sander. *Phys. Rev. Lett.*, 47(19):1400, 1981.

[174] P. Meakin. *Phys. Rev. A*, 27(3):1495, 1983.

[175] G. L. Tan, M. F. Lemon, D. J. Jones, and R. H. French. *Phys. Rev. B*, 72:205117, 2005.

[176] M. von Smoluchowski. *Z. Phys. Chem., Stöchiom. Verwandtschaftsl.*, 92:215, 1917.

[177] S. Chandrasekhar. *Rev. Mod. Phys.*, 15:1, 1943.

[178] W. B. Russel. *The Phase Behaviour and Dynamics of Colloidal Dispersions.* Lecture Notes, Debye Professor 2000-2001, University of Utrecht, Utrecht, 2005.

[179] D. Stauffer and A. Aharony. *Introduction to Percolation Theory.* Taylor and Francis, London, 1994.

[180] E. Zaccarelli. *J. Phys.: Condens. Matter*, 19:323101, 2007.

[181] P. J. Lu, E. Zaccarelli, F. Ciulla, A. B. Schofield, F. Sciortino, and D. A. Weitz. *Nature*, 453:499, 2008.

[182] C. Allain, M. Cloitre, and M. Wafra. *Phys. Rev. Lett.*, 74(8):1478, 1995.

[183] H. Verduin and J. K. G. Dhont. *J. Colloid Interface Sci.*, 172:425, 1995.

[184] W. C. K. Poon and M. D. Haw. *Adv. Colloid Interface Sci.*, 73:71, 1997.

[185] S. Manley, H. M. Wyss, K. Miyazaki, J. C. Conrad, V. Trappe, L. J. Kaufma, D. R. Reichman, and D. A. Weitz. *Phys. Rev. Lett.*, 95:238302, 2005.

[186] K. G. Soga, J. R. Melrose, and R. C. Ball. *J. Chem. Phys.*, 108(14):6026, 1998.

[187] V. Prasad, V. Trappe, A. D. Dinsmore, P. N. Segre, L. Cipelletti, and D. A. Weitz. *Faraday Discuss.*, 123:1, 2003.

[188] I. Saika-Voivod, E. Zaccarelli, F. Sciortino, S. V. Buldyrev, and P. Tartaglia. *Phys. Rev. E*, 70:041401, 2004.

[189] P. Charbonneau and D. R. Reichman. *Phys. Rev. E*, 75:011507, 2007.

[190] J. Bergenholtz and M. Fuchs. *Phys. Rev. E*, 59:5706, 1999.

[191] P. N. Segrè, V. Prasad, A. B. Schofield, and D. A. Weitz. *Phys. Rev. Lett.*, 86:6042, 2001.

[192] K.N. Pham, A. M. Puertas, J. Bergenholtz, S. U. Egelhaaf, A. Moussaid, P. N. Pusey, A. B. Schofield, M. E. Cates, M. Fuchs, and W. C. K. Poon. *Science*, 296:104, 2002.

[193] H. Sedgwick. *Colloidal Metastability*. PhD thesis, University of Edinburgh, 2003.

[194] H. Sedgwick, K. Kroy, A. Salonen, M. B. Robertson, S. U. Egelhaaf, and W. C. K. Poon. *Eur. Phys. J. E*, 16:77, 2005.

[195] K. Kroy, M. E. Cates, and W. C. K. Poon. *Phys. Rev. Lett.*, 92(14):148302, 2004.

[196] D. W. Schaefer. *Science*, 243(4758):1023, 1989.

[197] K. A. Granath. *J. Colloid Sci.*, 13(4):308, 1958.

[198] B. J. Berne and R. Pecora. *Dynamic Light Scattering*. Robert E. Krieger Publishing Company, Inc., Krieger Drive, Malabar, Florida 32950, 1990.

[199] C. P. Lindsey and G. D. Patterson. *J. Chem. Phys.*, 73(7):3348, 1980.

[200] D. R. Lide, editor. *CRC Handbook of Chemistry and Physics*. CRC Press, New York, 1997.

[201] A. J. Banchio and G. Nägele. *J. Chem. Phys.*, 128:104903, 2008.

[202] P. N. Pusey and R. J. A. Tough. Particle Interactions. In Robert Pecora, editor, *Dynamic Light Scattering*, pages 85–179, New York, 1985. Plenum Press.

[203] G. Nägele. *Phys. Rep.*, 272:215, 1996.

[204] A. K. van Helden, J. W. Jansen, and A. Vrij. *J. Colloid Interface Sci.*, 81(2):354, 1981.

[205] S. Coenen and C. G. de Kruif. *J. Colloid Interface Sci.*, 124(1):104, 1988.

[206] A. van Blaaderen and A. P. M. Kentgens. *J. Non-Cryst. Solids*, 149:161, 1992.

[207] G. H. Koenderink. *Rotational and Translational Diffusion in Colloidal Mixtures*. PhD thesis, Table 4.1, page 74, chapter 4, University of Utrecht, Utrecht, 2003.

[208] S. H. Behrens and D. G. Grier. *J. Chem. Phys.*, 115(14):6716, 2001.

[209] M. Doi and S. F. Edwards, editors. *The Theory of Polymer Dynamics*. Oxford University Press, Oxford, 1988.

[210] G.J. Fleer, M.A. Cohen Stuart, J.M.H.M. Scheutjens, T. Cosgrove, and B. Vincent. *Polymers at Interfaces*. Springer, Berlin, 1993.

[211] X. Zeng and K. Osseo-Asare. *Colloids Surf. A*, 226:45, 2003.

[212] B. A. Jucker, H. Harms, S. J. Hug, and A. J. B. Zehnder. *Colloids Surf. B*, 9:331, 1997.

[213] X. Zeng and K. Osseo-Asare. *J. Colloid Interface Sci.*, 272(2):298, 2004.

[214] G. Dietler, C. Aubert, D. S. Cannell, and P. Wiltzius. *Phys. Rev. Lett.*, 57(24):3117, 1986.

[215] M. Y. Lin, R. Klein, H. M. Lindsay, D. A. Weitz, R. C. Ball, and P. Meakin. *J. Colloid Interface Sci.*, 137:263, 1990.

[216] B. D. Butler, C. D. Muzny, and H. J. M. Hanley. *Int. J. Thermophys.*, 20(1):35, 1999.

[217] P. A. Heiney, R. J. Butera, J. D. Londono, R. V. Davidson, and S. Mazur. *J. Phys. Chem. B*, 104:8807, 2000.

[218] H. M. Wyss, J. Innerlohinger, L. P. Meier, L. J. Gauckler, and O. Glatter. *J. Colloid Interface Sci.*, 271:388, 2004.

[219] A. Alexander, P. M. Chaikin, P. Grant, G. J. Morales, and P. Pincus. *J. Chem. Phys.*, 80:5776, 1984.

[220] S. Pianegonda, E. Trizac, and Y. Levin. *J. Chem. Phys.*, 126:014702, 2007.

[221] L. F. Rojas-Ochoa, R. Castaneda-Priego, V. Lobaskin, A. Stradner, F. Scheffold, and P. Schurtenberger. *Phys. Rev. Lett.*, 100:178304, 2008.

[222] S. H. Behrens, D. I. Christl, R. Emmerzael, P. Schurtenberger, and M. Borkovec. *Langmuir*, 16:2566, 2000.

[223] S. Yu Shulepov and G. J. Frens. *J. Colloid Interface Sci.*, 170:44, 1995.

[224] S. Yu Shulepov and G. J. Frens. *J. Colloid Interface Sci.*, 182:388, 1996.

[225] H. Kihira, N. Ryde, and E. Matijevic. *Chem. Soc. Faraday Trans.*, 88:2379, 1992.

[226] G. M. Litton and T. M. Olson. *J. Colloid Interface Sci.*, 165:522, 1994.

[227] J. N. Israelachvili and R. M. Pashley. *Nature*, 306:249, 1983.

[228] J. N. Israelachvili and H. Wennerström. *Nature*, 379:219, 1996.

[229] G. K. Batchelor. *J. Fluid Mech.*, 74:1, 2008.

[230] S. Kim and S. J. Karrila. *Microhydrodynamics*. Dover Publications, Inc., Mineola, New York, 1990.

[231] D. J. Acheson. *Elementary Fluid Dynamics*. Oxford University Press, Oxford, 1990.

[232] J. E. Martin, J. P. Wilcoxon, D. Schaefer, and J. Odinek. *Phys. Rev. A*, 41(8):4379, 1990.

[233] S. Sauer and H. Löwen. *J. Phys.: Condens. Matter*, 8:L803, 1996.

[234] A. R. Denton. *Phys. Rev. E*, 62(3):3855, 2000.

[235] F. Scheffold and P. Schurtenberger. *Soft Materials*, 1(2):139, 2003.

[236] M. C. Grant and W. B. Russel. *Phys. Rev. E*, 47(4):2606, 1993.

[237] N. A. M. Verhaegh, D. Asnaghi, H. N. W. Lekkerkerker, M. Giglio, and L. Cipelletti. *Physica A*, 242:104, 1997.

[238] P. J. Lu, J. C. Conrad, H. M. Wyss, A. B. Schofield, and D. A. Weitz. *Phys. Rev. Lett.*, 96:028306, 2006.

[239] D. Pini, G. Jialin, A. Parola, and L. Reatto. *Chem. Phys. Lett.*, 327(3-4):209, 2000.

[240] A. Imperio and L. Reatto. *J. Phys.: Condens. Matter*, 16:S3769, 2004.

[241] Y. Liu, W.-R. Chen, and S.-H. Chen. *J. Chem. Phys.*, 122(4):044507, 2005.

[242] A. D. Dinsmore, V. Prasad, I.Y. Wong, and D. A. Weitz. *Phys. Rev. Lett.*, 96:185502, 2006.

[243] Y. Liu, E. Fratini, P. Baglioni, W.-R. Chen, and S.-H. Chen. *Phys. Rev. Lett.*, 95(11):118102, 2005.

[244] M. Malfois, F. Bonnete, L. Belloni, and A. Tardieu. *J. Chem. Phys.*, 105(8):3290, 1996.

[245] E. Bianchi, J. Largo, P. Tartaglia, E. Zaccarelli, and F. Sciortino. *Phys. Rev. Lett.*, 97(16):168301, 2006.

[246] Ghonasgi and Chapman, Ref. 252, and later Kern and Frenkel, Ref. 28, used the same angular distribution function to model attractive patchy interactions. However, in both cases a simple square-well pair potential was used.

[247] A. R. Hoskins, I. D. Robb, P. A. Williams, and P. Warren. *J. Chem. Soc., Faraday Trans.*, 92(22):4515, 1996.

[248] W. C. K. Poon. (private communication).

[249] S. Talreja, P. J. A. Kenis, and C. F. Zukoski. *Langmuir*, 23:4516, 2007.

[250] G. Nägele. *Theories of Fluid Microstructures.* 39th IFF Spring School, Institute of Solid State Research (IFF), Forschungszentrum Jülich, Jülich, 2008.

[251] T. Odijk. *arXiv:0807.4997v1*, 2008.

[252] D. Ghonasgi and W. G. Chapman. *Mol. Phys.*, 79(2):291, 1993.

Acknowledgements

First, and foremost, I would like to thank Gerhard Nägele for all his courage, support and patience, during my stay in Jülich and for accepting to referee this thesis.

I would like to express my gratitude to Jan Dhont for sharing his passion for science, and for the superb working conditions in his labs. Thank you to you and Kyong for our common Jülich sport's activities.

I would like to acknowledge the extended independence granted to me by my supervisors Remco Tuinier and Johan Buitenhuis. Thank you to both for proof-reading my thesis, in particular Johan whose comments have helped to improve the manuscript.

I would like to thank Prof. Egelhaaf for having accepted to review my thesis.

Especially I would like to thank Anna Stradner, Thomas Gibaud and Prof. Schurtenberger for the fruitful collaboration, and for the discussions during my visit to Fribourg.

I am indebted to several visitors in our soft matter group: Benoit Loppinet and George Petekidis for their interest in my work, and their company during their stopover in lovely Jülich. I also enjoyed the enthusiastic discussions with Prof. Poon from Edinburgh.

Thank you Abiramy, Angeliki, Emilie, Karolina, Manolis, Marco and Sylvia for your nice companion that I enjoyed a lot.

Last but not least I thank my mum and dad for all their support.

Die hier vorgelegte Dissertation habe ich eigenständig und ohne unerlaubte Hilfe angefertigt. Die Dissertation wurde in der vorgelegten oder in ähnlicher Form noch bei keiner anderen Institution eingereicht. Ich habe bisher keine erfolglosen Promotionsversuche unternommen.

Düsseldorf, den 30.09.2008

Christoph Gögelein